

**RENAL ARTERIAL BLOOD FLOW QUANTIFICATION BY BREATH-HELD
PHASE-VELOCITY ENCODED MRI**

A Thesis
Presented to
The Academic Faculty

By

Ashley Kay Wallin

In Partial Fulfillment
Of the Requirements for the Degree
Master of Science in Bioengineering

Georgia Institute of Technology
May 2004

**RENAL ARTERIAL BLOOD FLOW QUANTIFICATION BY BREATH-HELD
PHASE-VELOCITY ENCODED MRI**

Approved:

Ajit P. Yoganathan, PhD -- Chairman

Marijn Brummer, PhD

John Oshinski, PhD

Raymond Vito, PhD

Date Approved:
May 11, 2004

*For my family and for Clint,
Thank you for your constant love and support...*

ACKNOWLEDGEMENT

There are a number of individuals I would like to thank and acknowledge for their assistance and support in reaching my goals (specifically this thesis) and helping me to get to the point in my life that I am at today.

I would first like to thank my family. Mom, thank you for listening to me all the many days I was so upset and stressed. I would not have made “it out” without you. Dad, I do not know where I would be without all the days you pushed me. Just as you always said, it has paid off. I would also like to thank my brother, Patrick, for all the days he told me to cheer up and for how he can always make me laugh.

I would also like to thank Clint, for always being my pillar of support. Without him, the past four years would have been so much different and more difficult. He has such an incredible ability to calm me down when I feel that things cannot get any worse. I am so blessed to have such a wonderful and caring companion.

I owe my deepest appreciation to Dr. Dave Frakes, for ALL his assistance in so many ways relating to this work. From our many LATE nights dancing to the beat of the MRI, and all his support and advice; I am forever indebted. THANK YOU!!!

I would like to sincerely thank Dr. Arlene Chapman for not only her academic and financial support in this project, but for her medical knowledge and abilities. She has helped my family to such an incredible to degree, and I am so thankful for all her support and assistance.

I would like to thank Dr. Ajit Yoganathan for his support in helping me to complete this thesis and for showing me so many wonderful new ideas in the field of

Bioengineering. I would like to thank him for allowing me to be part of such a world-class research group made up of so many wonderful people. He has been influential in many of my decisions, and has taught me to look at everything from a broader point of view.

Many thanks to my committee members, Dr. Marijn Brummer, Dr. John Oshinski, and Dr. Ray Vito, for all their support of my research and their academic assistance. I would like to sincerely thank Dr. Brummer for his endless support and knowledge of MRI and for joining me during a number of scanning sessions. I am so thankful for my many conversations with Dr. Oshinski, and I could not have made it through all of this without the advice and support of Dr. Vito.

I am so grateful to all the members of the Cardiovascular Fluid Mechanics Laboratory, especially Dennis Soerensen, Kartik Sundareswaran, Helene Simon, Diane de Zelicourt, Jorge Jimenez and Jenni Nash for their help in finishing my thesis. My most sincere thanks goes to Chris Ruffin, for the time and energy he puts into this group. This would not have been completed without all of these individuals' help and support.

My deepest appreciation goes to Dr. David Sanborn, for his endless time and support. His advice throughout the years has been instrumental in the paths I have chosen. His exceptional teaching methods and the time he spends helping his students has made my time at Georgia Tech a much better experience. A special thanks goes to him for all his encouragement.

I would finally like to thank my friends, especially the girls at ZTA, for their encouraging words when I was up so late studying so many nights. Thank you for dealing with my frustrations and always helping me through the worst of days.

TABLE OF CONTENTS

ACKNOWLEDGEMENT	iv
TABLE OF CONTENTS	vi
LIST OF TABLES	viii
LIST OF FIGURES	x
LIST OF ABBREVIATIONS	xix
SUMMARY	xx
CHAPTER I	
INTRODUCTION	1
CHAPTER II	
BACKGROUND	5
The Normal Kidney	5
Polycystic Kidney Disease Pathology	8
Historical Perspective on Polycystic Kidney Disease	12
Magnetic Resonance Imaging and Flow Quantification	15
Phase-Contrast Velocity-Encoded Magnetic Resonance Imaging	15
<i>The Application of PC MRI to the Renal Arteries</i>	17
CHAPTER III	
HYPOTHESIS AND SPECIFIC AIMS	23
Hypothesis I	24
Hypothesis II	25
CHAPTER IV	
INSTRUMENTATION AND EXPERIMENTAL METHODS	27
<i>In Vitro</i> Model	27
Evaluation of Materials	31
PVA Preparation	31
Steady Flow Loop	33
Fluid Analysis	36
Principles of Magnetic Resonance Imaging	38
Magnetic Resonance Imaging Techniques and Protocol	43
Magnetic Resonance Image Analysis	45
Statistical Analysis: Bland and Altman Plots and Coefficient of Variance	48
CHAPTER V	
RESULTS	52
Material Evaluation Using PVA, Plastic, and Glass	53
Comparison of High-Resolution Scans: 160, 200 and 350 mm FOV	56
Low-Resolution Scan Comparison: 160, 200 and 350 mm FOV	70
Multiple-Site Study	77

Velocity Encoding in Three Directions	82
Summary of Findings	84
CHAPTER VI	
DISCUSSION	85
Motivation for the Study	85
Material Evaluation Using PVA, Plastic, and Glass	86
Comparison of High-Resolution Scans: 160, 200, and 350 mm FOV	89
<i>Field of View</i>	89
<i>Wraparound Artifact</i>	92
<i>Background Subtraction</i>	96
<i>Region of Interest</i>	98
Low-Resolution Scan Comparison: 160, 200, and 350 mm FOV	100
Multiple-Site Study	101
Velocity Encoding in Three Directions	103
CHAPTER VII	
CONCLUSIONS	105
CHAPTER VIII	
RECOMMENDATIONS	109
REFERENCES	112
APPENDIX I	
BLAND-ALTMAN PLOTS	121

LIST OF TABLES

- Table 4-1: Experimental flow rates measured using the weight determination method. The listed flow rates are an averaged value of the fluid collected prior to the first scan and after the last scan, with the exception of the two highest flow rates for the largest diameter of 11.11 mm.
- Table 4-2: Imaging parameters for the gradient-echo breath-held velocity-encoded acquisitions.
- Table 4-3: Experimental flow rates used to assess inter- and intraobserver variability. Data was compiled at these flow rates, which represent a mid-range rate of flow for each simulated vessel, at 160 and 200 mm FOV ($n = 12$).
- Table 5-1: Correlation coefficients calculated for each ROI based upon the data presented in Figures 5-3 through 5-5.
- Table 5-2: Various quantitative results extracted from the Bland and Altman plots shown in Appendix A (Figures A-1 through A-18). The bias is calculated by finding the mean difference between methods, and may be used to adjust results obtained using a new clinical method based on a more established one. Based on the assumption of a normal distribution, the majority of data points (95%) will lie within two standard deviations (SD) of the mean. The upper and lower percent differences display the difference between methods as a percent of the averages. The terms in the table correspond to the following: magnitude image contour (ROI 1); phase image contour (ROI 2); and automatic contour (ROI 3). “BG” denotes that background subtraction has been applied to the data series.
- Table 5-3: Various quantitative results extracted from the Bland and Altman plots shown in Figures 5-26 through 5-35 using low-resolution protocol (96 phase encodings). A brief description of each of these statistical parameters is provided with Table 5-2. When comparing the values in this table with those in Table 5-2, it is apparent that high-resolution protocol (192 phase encodings) provides significantly more accurate results, as further shown in the following figures.
- Table 5-4: Reynolds numbers resulting from experimental flow rates measured using the weight determination method, which are shown in parentheses below each corresponding Reynolds number. The Reynolds numbers listed below were calculated using Equation (4-2) and are all within the laminar range, as defined by Munson et al. [99].

- Table 5-5: Quantitative summary resulting from experiment with velocity encoded in three directions. A field of view of 240 mm was used in this protocol. The magnitude (ROI 1), phase (ROI 2), and automatic (ROI 3) borders were analyzed using this technique. The automatic detection algorithm most accurately analyzed the velocity data encoded in the phase-velocity images for this protocol, but not by a significant amount.
- Table 6-1: Parameters used to correct wraparound artifact for 3.175 mm simulated vessel. V_{min} and v_{max} are provided for each scan corrected. It is important to note the direct relationship between FOV and the degree of aliasing: as the FOV increases, the degree of phase wrap increases, as well.
- Table 6-2: Resulting COV values between true flow and flow measured using velocity-encoded MRI (graphically shown in Figures 5-14 and 5-15). Background subtraction actually increased the COV between the true flow MRI flow in all experiments, with the exception of ROI 2 using the 160 mm FOV.

LIST OF FIGURES

- Figure 2-1: Anterior view of kidneys *in situ*. It is interesting to note that the left kidney is usually larger than the right [30-31]. [33]
- Figure 2-2: Kidney anatomy and enhanced view of nephron. [34]
- Figure 2-3: Illustrative comparison of polycystic and normal kidneys. [42]
- Figure 2-4: Comparison of polycystic kidney (left) with a healthy kidney (right). [29]
- Figure 4-1: PVA phantom used in validation experiments. The model was constructed with six hollow channels running through the PVA ranging in diameter from 3.18 to 11.11 (± 0.01) mm. PVA proved to be the superior choice among other possible phantom materials during initial experimentation.
- Figure 4-2: The chemical structure of the polyvinyl alcohol molecule. PVA has been reported to have a number of significant medical applications including its use in MR quality control phantoms.
- Figure 4-3: Flow loop used in steady flow validation experiment. This schematic shows the setup for the 9.53 mm experiment. It is also important to note that PVC tubing was returned over the phantom model in order to capture flow through the vinyl (PVC) tubing for comparison of material experiments. The same set of PVC tubing would have also been used for the 11.11 mm experiments.
- Figure 4-4: This diagram displays the two main properties of NMR. **(a)** In the absence of an external magnetic field, a hydrogen proton has an intrinsic magnetic field due to the property of nuclear spin. **(b)** When an external magnetic field (B_0) is applied, the spinning proton not only spins about its own axis, but also around the axis created by the applied magnetism.
- Figure 4-5: **(a)** A representation of the chaotic array of hydrogen protons when an external magnetic field (B_0) is absent and **(b)** the alignment that occurs when the magnetic field is applied. In **(b)**, the bars above and below the protons represent the poles of the magnet. In MRI, protons may either align with the direction of the magnetic field or against it, resulting in two different energy states. In this example, when B_0 is applied, the first two columns represent the lower energy state, as these protons align in the direction of the external magnetic field, while the last column represents the higher energy state.

- Figure 4-6: Sample screen layout using the FLOW software package. The first region of interest (red) was drawn manually in the modulus image (right), while the second region of interest (green) was drawn in the phase image (left). The third region of interest (white) was created using the automatic contour detection algorithm included in the program. The fourth region of interest (C-shape) was used to correct for static velocity components.
- Figure 4-7: Example of a Bland and Altman Plot using the difference between methods. Other variations of this plot may be used, including the presentation of the difference between methods as a percent, which will be further discussed in Chapter V.
- Figure 5-1: Flow rate data obtained from PVA and plastic at the 200 mm FOV with no background correction applied. These results were obtained from the following channels: 3.18, 4.76, and 7.94 mm. As shown, the plastic data deviates more from the true flow rate values than the PVA data.
- Figure 5-2: Average COV results calculated from the image data acquired using PVA, plastic, and glass at the 200 mm FOV. The average COV of PVA is consistently less than that of the two supplementary materials studied.
- Figure 5-3: Flow rate data obtained from high-resolution experiments at the 160 mm FOV as compared to the true flow rates calculated using the weight determination method. All flow rates presented here span the entire range of simulated vessels ($n = 32$). The terms in the legend correspond to the following: magnitude image contour (ROI 1); phase image contour (ROI 2); and automatic contour (ROI 3). “BG” denotes that background subtraction has been applied to the data series.
- Figure 5-4: Flow rate data obtained from high-resolution experiments at the 200 mm FOV as compared to the true flow rates calculated using the weight determination method. All flow rates presented here span the entire range of simulated vessels ($n = 32$). The terms in the legend correspond to the following: magnitude image contour (ROI 1); phase image contour (ROI 2); and automatic contour (ROI 3). “BG” denotes that background subtraction has been applied to the data series.
- Figure 5-5: Flow rate data obtained from high-resolution experiments at the 350 mm FOV as compared to the true flow rates calculated using the weight determination method. All flow rates presented here span the entire range of simulated vessels ($n = 32$), except for ROI 3 and BG ROI 3, where $n = 31$. The terms in the legend correspond to the following: magnitude image contour (ROI 1); phase image contour (ROI 2); and automatic contour (ROI 3). “BG” denotes that background subtraction has been applied to the data series.

- Figure 5-6: Graphical comparison of data analysis using the Bland-Altman method. The data presented here was acquired using the magnitude border (ROI 1) at 160, 200, and 350 mm FOV and corresponds to the data presented in Table 5-2. The 160 mm FOV proved to be the most accurate parameter in this case, while the 350 mm FOV was the least accurate.
- Figure 5-7: Graphical comparison of data analysis using the Bland-Altman method. The data presented here was acquired using the phase border (ROI 2) at 160, 200, and 350 mm FOV and corresponds to the data presented in Table 5-2. The 200 mm FOV proved to be the most accurate parameter in this case, while the 350 mm FOV was the least accurate.
- Figure 5-8: Graphical comparison of data analysis using the Bland-Altman method. The data presented here was acquired using the automatic border (ROI 3) at 160, 200, and 350 mm FOV and corresponds to the data presented in Table 5-2. The 200 mm FOV proved to be the most accurate parameter in this case, while the 350 mm FOV was once again the least accurate.
- Figure 5-9: Graphical comparison of data analysis using the Bland-Altman method. The data presented here was acquired using the magnitude border with background correction (BG ROI 1) at 160, 200, and 350 mm FOV and corresponds to the data presented in Table 5-2. The 160 mm FOV proved to be the most accurate parameter in this case, while the 200 mm FOV was the least accurate.
- Figure 5-10: Graphical comparison of data analysis using the Bland-Altman method. The data presented here was acquired using the phase border with background correction (BG ROI 2) at 160, 200, and 350 mm FOV and corresponds to the data presented in Table 5-2. In this case, the 160 and 200 mm FOV were the most accurate parameters.
- Figure 5-11: Graphical comparison of data analysis using the Bland-Altman method. The data presented here was acquired using the automatic border with background correction (BG ROI 1) at 160, 200, and 350 mm FOV and corresponds to the data presented in Table 5-2. The 200 mm FOV proved to be the most accurate parameter in this case, while the 350 mm FOV was the least accurate.
- Figure 5-12: Bland and Altman plot displaying the difference between the true flow values and the experimental MRI data ($n = 64$). This plot corresponds to combined data sets of ROI 1 and ROI 2 at the 160 mm FOV.
- Figure 5-13: Bland and Altman plot displaying the difference between the true flow values and the experimental MRI data ($n = 64$). This plot corresponds to combined data sets of ROI 1 and ROI 2 at the 200 mm FOV.

- Figure 5-14: Average COV results calculated from the image data acquired using the 160 mm FOV. Background correction (BG) does not improve the results and even has a significant negative effect on ROI 1 and ROI 3.
- Figure 5-15: Average COV results calculated from the image data acquired using the 200 mm FOV. Background correction (BG) has no positive effect on this data, as all ROIs are negatively affected and vary more from true flow.
- Figure 5-16: Graphical comparison of high-resolution (192 phase encodings) and low-resolution (96 phase encodings) protocol obtained using the Bland-Altman method. The data presented here was acquired using the magnitude border (ROI 1) at the 160, 200, and 350 mm FOV and corresponds to the data presented in Table 5-3. The amount of variability between low- and high-resolution increased with increasing field of view.
- Figure 5-17: Graphical comparison of high-resolution (192 phase encodings) and low-resolution (96 phase encodings) protocol obtained using the Bland-Altman method. The data presented here was acquired using the phase border (ROI 2) at the 160, 200, and 350 mm FOV and corresponds to the data presented in Table 5-3. The amount of variability between low- and high-resolution again increased with increasing field of view.
- Figure 5-18: Graphical comparison of high-resolution (192 phase encodings) and low-resolution (96 phase encodings) protocol obtained using the Bland-Altman method. The data presented here was acquired using the automatic border (ROI 3) at 160, 200, and 350 mm FOV and corresponds to the data presented in Table 5-3. In this case, the low-resolution data is comparable at 160 and 200 mm FOV, while increased variability is observed at 350 mm FOV.
- Figure 5-19: Bland and Altman plot displaying the difference between true flow values and MRI data as a percentage using low-resolution protocol (96 phase encodings). This figure specifically shows the extreme deviation from true flow, especially at lower flow rates (< 500 ml/min). Data presented here is from the phase image contour obtained using 160 mm FOV.
- Figure 5-20: Bland and Altman plot displaying the difference between true flow values and MRI data as a percentage using low-resolution protocol (96 phase encodings). This figure also shows the extreme deviation from true flow, specifically at lower flow rates (< 500 ml/min). Data presented here is from the magnitude image contour obtained using 200 mm FOV.

Figure 5-21: Schematic showing visually-defined perpendicular planes used to capture velocity-encoded phase images in this phantom validation study. The first scan plane is centered along the phantom, and this data is presented as the 200 mm FOV high-resolution data. The second and third scan planes were used to evaluate flow along the length of each simulated vessel at the 200 mm FOV.

Figure 5-22: Bland and Altman plot displaying the difference between sites 2 and 3 as compared to site 1 (Figure 5-21). This plot corresponds to the manual contour drawn in the magnitude image (ROI 1) at the 200 mm FOV.

Figure 5-23: Bland and Altman plot displaying the difference between sites 2 and 3 as compared to site 1 (Figure 5-21). This plot corresponds to the manual contour drawn in the phase image (ROI 2) at the 200 mm FOV.

Figure 5-24: Graphical comparison of high-resolution protocol at the 200 mm FOV with protocol velocity-encoded in all three orthogonal planes (240 mm FOV). It is shown that this technique is not useful as compared to high-resolution protocol, as increased variability is observed with all image contours at the 240 mm FOV.

Figure 6-1: *In vitro* and *in vivo* breath-held phase-velocity encoded MRI scans. The plastic material in (A) was found to perform less like the *in vivo* tissue in (B) than the PVA in (C).

Figure 6-2: Comparison of Bland-Altman plots using the phase border using (A) the 160 mm FOV and (B) the 350 mm FOV. The 95% limits of agreement for the 350 mm FOV data were larger than the 160 mm FOV, indicating that minimization of FOV is important for accurate flow results.

Figure 6-3: Phase image for the 160 mm FOV scan obtained for the 3.18 mm channel experiment. The arrow points to the flow region, which contains the wraparound artifact. This phenomenon is due to the excitation of tissue outside the defined FOV boundary, which causes the anatomy to be displaced from its actual position. This image was corrected by properly encoding the “unwanted” tissue using the phase-unwrap feature in the FLOW software program. These values are presented in Table 6-1.

Figure A-1: Bland and Altman plot displaying the difference between the true flow values and the experimental MRI data ($n = 32$). This plot corresponds to the contour drawn in the magnitude image (ROI 1) without background correction at 160 mm FOV.

- Figure A-2: Bland and Altman plot displaying the difference between the true flow values and the experimental MRI data ($n = 32$). This plot corresponds to the contour drawn in the magnitude image (ROI 1) with background correction at 160 mm FOV.
- Figure A-3: Bland and Altman plot displaying the difference between the true flow values and the experimental MRI data ($n = 32$). This plot corresponds to the contour drawn in the phase image (ROI 2) without background correction at 160 mm FOV.
- Figure A-4: Bland and Altman plot displaying the difference between the true flow values and the experimental MRI data ($n = 32$). This plot corresponds to the contour drawn in the phase image (ROI 2) with background correction at 160 mm FOV.
- Figure A-5: Bland and Altman plot displaying the difference between the true flow values and the experimental MRI data ($n = 32$). This plot corresponds to the automatic contour drawn in the phase image (ROI 3) using the algorithm in the FLOW software without background correction at 160 mm FOV.
- Figure A-6: Bland and Altman plot displaying the difference between the true flow values and the experimental MRI data ($n = 32$). This plot corresponds to the automatic contour drawn in the phase image (ROI 3) using the algorithm in the FLOW software with background correction at 160 mm FOV.
- Figure A-7: Bland and Altman plot displaying the difference between the true flow values and the experimental MRI data ($n = 32$). This plot corresponds to the contour drawn in the magnitude image (ROI 1) without background correction at 200 mm FOV.
- Figure A-8: Bland and Altman plot displaying the difference between the true flow values and the experimental MRI data ($n = 32$). This plot corresponds to the contour drawn in the magnitude image (ROI 1) with background correction at 200 mm FOV.
- Figure A-9: Bland and Altman plot displaying the difference between the true flow values and the experimental MRI data ($n = 32$). This plot corresponds to the contour drawn in the phase image (ROI 2) without background correction at 200 mm FOV.
- Figure A-10: Bland and Altman plot displaying the difference between the true flow values and the experimental MRI data ($n = 32$). This plot corresponds to the contour drawn in the phase image (ROI 2) with background correction at 200 mm FOV.

Figure A-11: Bland and Altman plot displaying the difference between the true flow values and the experimental MRI data ($n = 32$). This plot corresponds to the automatic contour drawn in the phase image (ROI 3) using the algorithm in the FLOW software without background correction at 200 mm FOV.

Figure A-12: Bland and Altman plot displaying the difference between the true flow values and the experimental MRI data ($n = 32$). This plot corresponds to the automatic contour drawn in the phase image (ROI 3) using the algorithm in the FLOW software with background correction at 200 mm FOV.

Figure A-13: Bland and Altman plot displaying the difference between the true flow values and the experimental MRI data ($n = 32$). This plot corresponds to the contour drawn in the magnitude image (ROI 1) without background correction at 350 mm FOV.

Figure A-14: Bland and Altman plot displaying the difference between the true flow values and the experimental MRI data ($n = 32$). This plot corresponds to the contour drawn in the magnitude image (ROI 1) with background correction at 350 mm FOV.

Figure A-15: Bland and Altman plot displaying the difference between the true flow values and the experimental MRI data ($n = 32$). This plot corresponds to the contour drawn in the phase image (ROI 2) without background correction at 350 mm FOV.

Figure A-16: Bland and Altman plot displaying the difference between the true flow values and the experimental MRI data ($n = 32$). This plot corresponds to the contour drawn in the phase image (ROI 2) with background correction at 350 mm FOV.

Figure A-17: Bland and Altman plot displaying the difference between the true flow values and the experimental MRI data ($n = 31$). This plot corresponds to the automatic contour drawn in the phase image (ROI 3) using the algorithm in the FLOW software without background correction at 350 mm FOV.

Figure A-18: Bland and Altman plot displaying the difference between the true flow values and the experimental MRI data ($n = 31$). This plot corresponds to the automatic contour drawn in the phase image (ROI 3) using the algorithm in the FLOW software with background correction at 350 mm FOV.

Figure A-19: Bland and Altman plot displaying the difference between methods using two independent and blinded observers at the 160 mm FOV (interobserver study).

Figure A-20: Bland and Altman plot displaying the difference between methods using two independent and blinded observers at the 200 mm FOV (interobserver study).

Figure A-21: Bland and Altman plot displaying the difference between methods using a single observer at two different dates at the 160 mm FOV (intraobserver study).

Figure A-22: Bland and Altman plot displaying the difference between methods using a single observer at two different dates at the 200 mm FOV (intraobserver study).

Figure A-23: Bland and Altman plot displaying the difference between the true flow values and the experimental MRI data using a low-resolution protocol ($n = 32$). This plot corresponds to the contour drawn in the magnitude image (ROI 1) at 160 mm FOV.

Figure A-24: Bland and Altman plot displaying the difference between the true flow values and the experimental MRI data using a low-resolution protocol ($n = 32$). This plot corresponds to the contour drawn in the phase image (ROI 2) at 160 mm FOV.

Figure A-25: Bland and Altman plot displaying the difference between the true flow values and the experimental MRI data using a low-resolution protocol ($n = 32$). This plot corresponds to the automatic contour drawn in the phase image (ROI 3) using the algorithm in the FLOW software at 160 mm FOV.

Figure A-26: Bland and Altman plot displaying the difference between the true flow values and the experimental MRI data using a low-resolution protocol ($n = 32$). This plot corresponds to the contour drawn in the magnitude image (ROI 1) at 200 mm FOV.

Figure A-27: Bland and Altman plot displaying the difference between the true flow values and the experimental MRI data using a low-resolution protocol ($n = 32$). This plot corresponds to the contour drawn in the phase image (ROI 2) at 200 mm FOV.

Figure A-28: Bland and Altman plot displaying the difference between the true flow values and the experimental MRI data using a low-resolution protocol ($n = 32$). This plot corresponds to the automatic contour drawn in the phase image (ROI 3) using the algorithm in the FLOW software at 200 mm FOV.

Figure A-29: Bland and Altman plot displaying the difference between the true flow values and the experimental MRI data using a low-resolution protocol ($n = 32$). This plot corresponds to the contour drawn in the magnitude image (ROI 1) at 350 mm FOV.

Figure A-30: Bland and Altman plot displaying the difference between the true flow values and the experimental MRI data using a low-resolution protocol ($n = 32$). This plot corresponds to the contour drawn in the phase image (ROI 2) at 350 mm FOV.

Figure A-31: Bland and Altman plot displaying the difference between the true flow values and the experimental MRI data using a low-resolution protocol ($n = 31$). This plot corresponds to the automatic contour drawn in the phase image (ROI 3) using the algorithm in the FLOW software at 350 mm FOV.

LIST OF ABBREVIATIONS

ADPKD (autosomal polycystic kidney disease)
RBF (renal blood flow)
MRI (magnetic resonance imaging)
CT (computed tomography)
NIH (National Institutes of Health)
CRISP (Consortium for Radiologic Imaging Studies of Polycystic Kidney Disease)
2D PC MR (two-dimensional phase-contrast magnetic resonance)
PVA (polyvinyl alcohol)
GFR (glomerular filtration rate)
PKD (polycystic kidney disease)
PAH (para-amino-hippurate, a clearance technique)
MRA (magnetic resonance angiography)
NMR (nuclear magnetic resonance)
RF (radiofrequency)
PVC MRI (phase-velocity cine MRI)
FE-EPI (multi-shot echoplanar imaging)
FOV (field of view)
ROI (region of interest)

SUMMARY

Autosomal dominant polycystic disease (ADPKD) is the most common hereditary renal disease and is characterized by renal cyst growth and enlargement. Hypertension occurs early when renal function is normal and is characterized by decreased renal blood flow. Accordingly, the measurement of blood flow in the renal arteries can be a valuable tool in evaluating disease progression. In studies performed in conjunction with this work, blood flow was measured through the renal arteries using magnetic resonance imaging (MRI). In order to validate these in vivo measurements, a vascular phantom was created using polyvinyl alcohol (PVA) and also scanned using MRI under controlled steady flow conditions. Ranges of vessel diameters and flow velocities were used to simulate actual flow in a normal and diseased population of adults and children.

With the vessel diameters studied in this experiment, minimization of field of view and an increase in spatial resolution is important in obtaining accurate data. However, a significant difference does not exist between the results when using the 160 or 200 mm FOV. An increase in the number of phase encodings provides improved results, although an increase in image acquisition time is observed. Velocity-encoding in all three orthogonal directions does not improve image data. This method of using MRI to measure flow through a vessel is shown to be both accurate and reproducible, and the protocol providing the most correct results is prescribed.

Breath-hold phase-velocity encoded MRI proves to be an accurate and reproducible technique in capturing flow and has the potential to be used for the purpose of observing hemodynamic changes in the renal arteries with the progression of ADPKD.

The results of these experiments are currently being implemented and used in patient studies to determine the extent to which MRI may be used as a non-invasive diagnostic technique in assessing disease progression.

CHAPTER I

INTRODUCTION

Autosomal dominant polycystic kidney disease (ADPKD) is the most common hereditary renal disease, affecting approximately 500,000 people in the United States, alone [1]. Of these, approximately 1,800 require the initiation of renal replacement therapy each year [2], costing half-a-billion dollars annually [3]. About 1 in 1,000 individuals carry a mutant gene causing this condition [4], which is a disease distinguished by renal cyst growth and enlargement. ADPKD is also one of many pathologies characterized by decreased renal blood flow (RBF). Hypertension occurs early when renal function is essentially normal, and it is preceded by, or seen in conjunction with, compromised flow in the renal arteries [5]. Accordingly, the measurement of blood flow in renal arteries may become a valuable tool in evaluating disease progression. Renal sufficiency deteriorates as the disease progresses, ultimately resulting in end-stage renal failure. ADPKD is the single greatest cause of end-stage renal failure in the United States, following diabetes mellitus, hypertension, and glomerulonephritis [3].

Little attention has been given to the idea that the evaluation of RBF may be used as a marker of disease severity, despite evidence that it may contribute to renal failure. Even as early as 1929, it was noticed that the vascular system is impaired in ADPKD

individuals. It has been shown that the number of small arteries and arterioles is greatly reduced in polycystic kidneys [6] and that an increased wall-to-lumen ratio exists in these vascular areas [7-8]. These observations have been confirmed in more recent studies [9].

Because approximately ninety-five percent of ADPKD patients inherit the disease from a parent [2], an effective early detection and prevention program is essential in an effort to care for individuals in this population. Over the past ten years, major advances in the understanding of genetics, as well as the mechanisms and rate of disease progression, have continued to provide hope that this type of program will soon become available. A number of modalities have been used to assess this disease, both invasive and non-invasive. Recent technological improvements have improved non-invasive data acquisition techniques. The information that has been obtained using a number of these improved modalities has provided additional insight into the pathogenesis of ADPKD.

Magnetic resonance imaging (MRI) is not the only available non-invasive modality used in diagnosing and treating ADPKD; however, other modalities, such as ultrasound and computed tomography (CT), do not provide the same range of information as MRI. In one scan session, renal hemodynamic parameters, as well as an entire map of kidney and cyst volumes may be obtained. Ultrasound also causes some degree of discomfort, as the probe must be firmly pressed over the ribs to obtain accurate images of the left and right kidneys. Only MRI provides the wide range of diagnostic images needed to accurately diagnose and assess the disease.

With the vast progress that has been made using non-invasive technologies, specifically in MRI, the use of RBF measurements for treatment purposes is receiving more attention from medical professionals and researchers. It is becoming an established

technique, particularly in the area of cardiology. Multiple studies have validated its accuracy for this purpose in both flow phantoms and *in vivo* [10-18]. In a multi-center National Institutes of Health (NIH)-sponsored study, referred to as the Consortium for Radiologic Imaging Studies of Polycystic Kidney Disease (CRISP), an effort was made to develop accurate MRI protocol assessing RBF changes in ADPKD patients using longitudinal MRI studies. This clinical study is currently exploring the use of two-dimensional breath-held gradient echo techniques using existing clinical imaging equipment to establish an effective method for accomplishing the aforementioned goal. Using one hundred twenty-seven ADPKD subjects, King et al. have studied the changes that occur as the disease progresses, including those observed in RBF, as well as total and cyst renal volumes, using MRI [19].

To ensure that this RBF data is valid, a comprehensive vascular phantom validation study was performed using a full range of vessel diameters and flow rates testing the physiological ranges of flow and arterial sizes encountered *in vivo*. In this study, a series of two-dimensional phase-contrast magnetic resonance (2D PC MR) scans was performed on a range of simulated vessels representing both normal and diseased flow. The resulting data was analyzed in order to extract the flow measurements recorded using the velocity-encoded images.

Various materials were also tested in the development of this vascular phantom. A number of materials have been used in the past as MR quality control phantoms including rigid materials, such as glass [20], acrylic [21], and polyester [22], and those that are flexible, including silicone [23] and latex rubber [24]. These materials all exhibit MRI compliancy, but do not provide the most accurate results: glass, acrylic, and

polyester do not provide an MRI signal, while silicone and latex rubber do not have anthropomorphic properties [25]. Polyvinyl alcohol (PVA), which is a polymer that retains more than 20% water within its structure (hydrogel), has been shown to have excellent MR properties [25-28] and is consequently examined in this experimental validation study.

The possibility of using MRI to accurately detect flow characteristics in the renal arteries may assist in reducing the number of invasive procedures required in diagnosis and disease progression evaluation. Patients and their families are also far more likely to participate in research monitoring disease progression if this involves non-invasive studies, as opposed to those that are invasive, thereby providing a more detailed and accurate understanding of the pathology of the disease. The study described in this report seeks to validate *in vivo* MR results, which will assist in treating a significant number of individuals afflicted with ADPKD. As an established and accepted technology, velocity-encoded MRI may ultimately be used to guide therapy in not only ADPKD, but also in a variety of other renal diseases.

CHAPTER II

BACKGROUND

The Normal Kidney

The kidneys (Figure 2-1 and 2-2) are part of a regulating system that perform a variety of functions. They ensure that electrolytes, such as sodium, potassium, calcium, phosphorous, and other chemicals are in balance. Kidneys produce several essential hormones and change vitamin D into its active form. The kidneys also help regulate the pH of body fluids and filter and excrete waste products. Kidneys filter blood plasma and produce urine, by which waste products are eliminated from the body. When kidney function is impaired, these waste products cannot be eliminated from the body. This causes a toxic condition known as uremic poisoning [29].

Each person is normally born with two kidneys, which are located in the back of the body, on each side of the spine and positioned under the rib cage. It is important to note that the left kidney is usually slightly larger than the right [30-31], which results in increased volume and dynamic flow values. These organs are truly remarkable, as a single kidney can function at 20% of its capacity while still providing all required renal filtration and regulation [32]. Kidneys are normally about five- an-a-half inches long, three inches wide, two inches thick, and usually weigh ten to twelve ounces. The size of

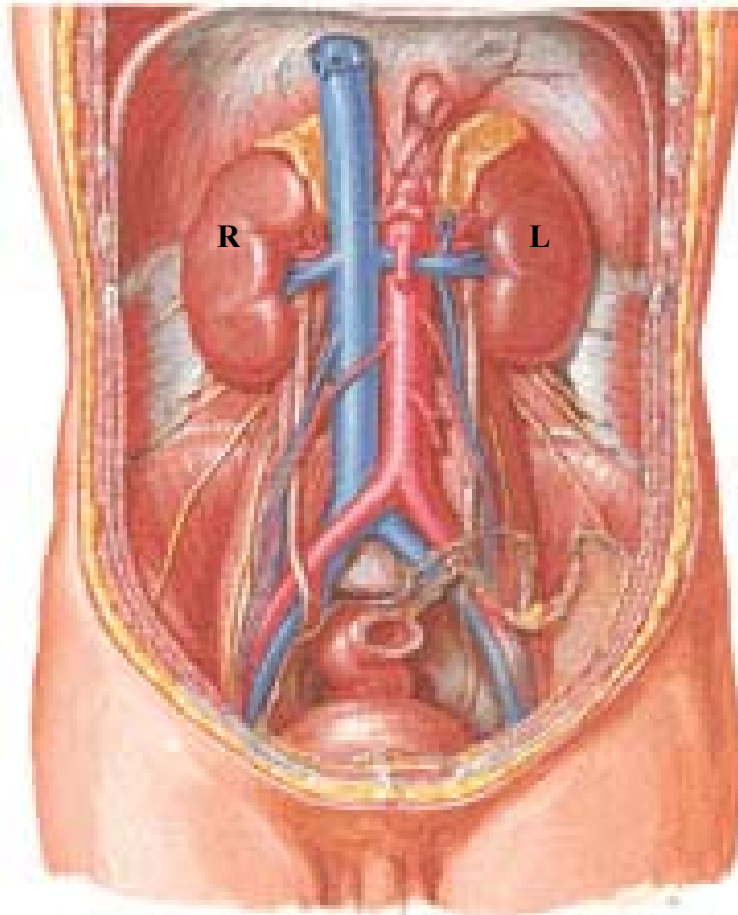


Figure 2-1: Anterior view of kidneys *in situ*. It is interesting to note that the left kidney is usually larger than the right [30-31]. [33]

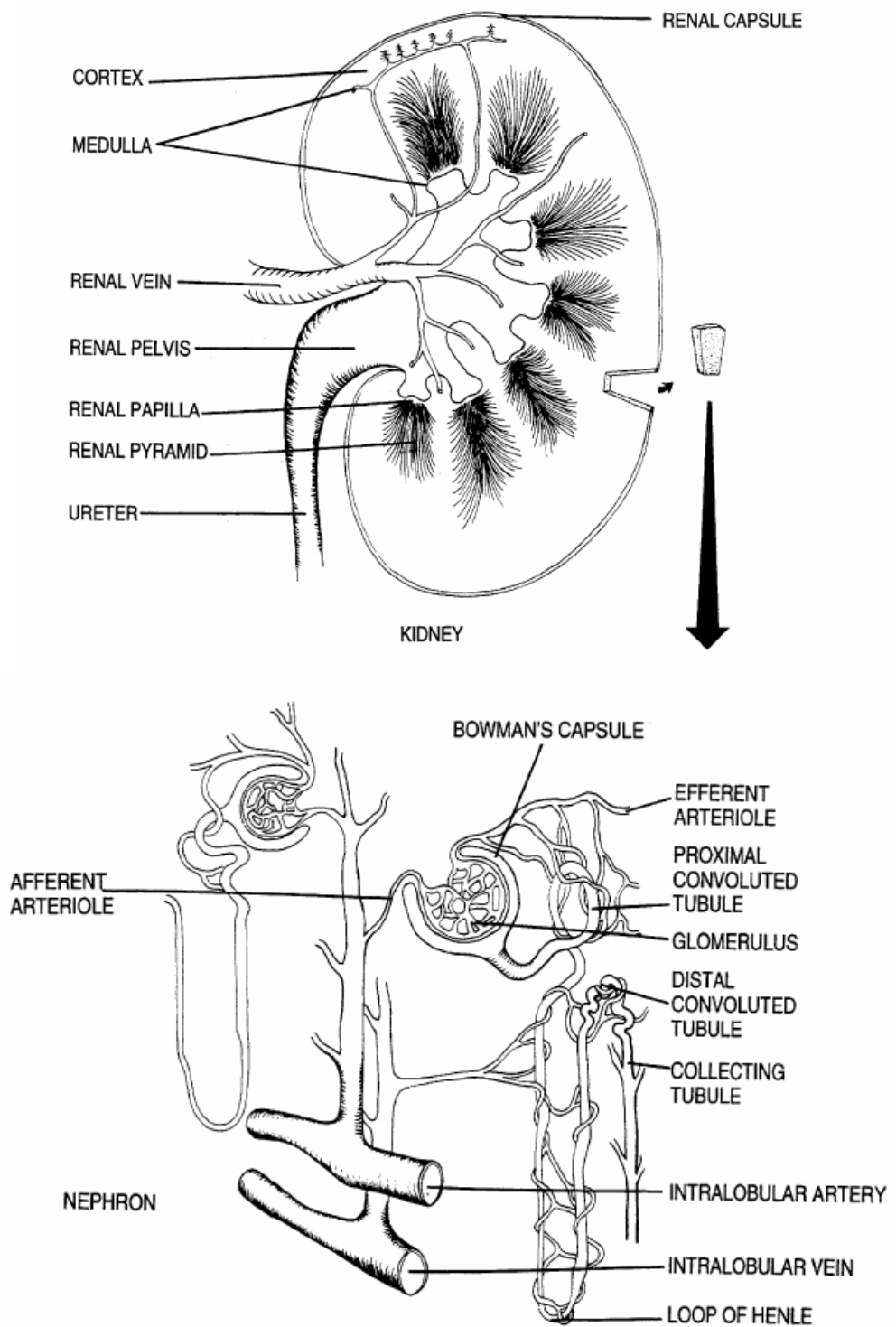


Figure 2-2: Kidney anatomy and enhanced view of nephron. [34]

a kidney may be approximated as the size of a human fist. A kidney is comprised of approximately one million tiny tubes referred to as nephrons (Figure 2-2). Up to twenty-five percent of the blood that the heart pumps every second travels into the kidneys from the renal arteries and flows through the glomeruli, which are filters located in each nephron. The glomeruli remove substances including urea, creatinine, and ureic acid. The kidney removes creatinine in such an efficient manner that the level of creatinine in the blood may be used as a diagnostic tool to determine kidney function. This test is performed using results from a blood test and a twenty-four hour urine collection, along with height and weight, and is referred to as creatinine clearance or glomerular filtration rate (GFR) [1, 29].

Polycystic Kidney Disease Pathology

Polycystic kidney disease (PKD) is diagnosed as two hereditary forms, and is characterized by renal cyst enlargement, interstitial fibrosis, and progressive deterioration of renal function in conjunction with the loss of normal renal tissue [1, 35]. Autosomal dominant polycystic kidney disease (ADPKD) is the most common of all life-threatening genetic diseases, and about 1 in 1000 people carry a mutant gene for the condition [36]. In the past, it has sometimes been referred to as adult polycystic kidney disease, or APKD [37-39]. Autosomal recessive (ARPKD) often causes mortality in the first month of life; however, it is also very rare. In the presence of PKD, cysts develop in the kidneys (Figure 2-3). The appearance of cysts is variable and detection ranges from birth

to healthy individuals over eighty years of age [39]. The cysts may also spread to other organs, most commonly the liver. Cysts may be as small as pinhead and may grow to be as large as a grapefruit. The kidneys may grow to be larger than a football (Figure 2-4) and have weighed as much as thirty-eight pounds each in the presence of many cysts.

ADPKD is usually caused by a mutant gene at the PKD1 locus on the short arm of chromosome 16; however, unknown mutations elsewhere in the genome cause the disease in approximately four percent of cases [4]. In these specific cases, if renal cysts develop, renal failure will most likely not occur until later in life. Renal dysfunction due to the disease most often occurs in middle-aged individuals; however, a considerable number of diseased individuals remain asymptomatic [36, 40-41]. It has been estimated that approximately 53 percent of individuals will develop end-stage renal disease by the age of fifty-eight; however, this approximation does present a considerable amount of uncertainty (95 percent confidence interval, 0.34 to 0.72), as few patients over 50 years have been studied [40].

Cysts begin as a blister-like occurrence of the nephron. Most cysts detach when they are small and enlarge over time, becoming filled with fluid. Three components to cyst formation have been determined. The first is cell proliferation, in which the cells of a cyst wall reproduce more rapidly than normal kidney cells. Therefore, the cysts become larger. Cellular secretion is also a factor in cyst formation. The cells produce fluid, which fills the cyst. An abnormal basement membrane has also been found to contribute to cyst formation. The basement layer is the thin layer of tissue that cyst cells sit on and is thicker than normal and has an unusual makeup in ADPKD patients. Cysts cause problems due to the size and space they occupy. Their size is directly related to the

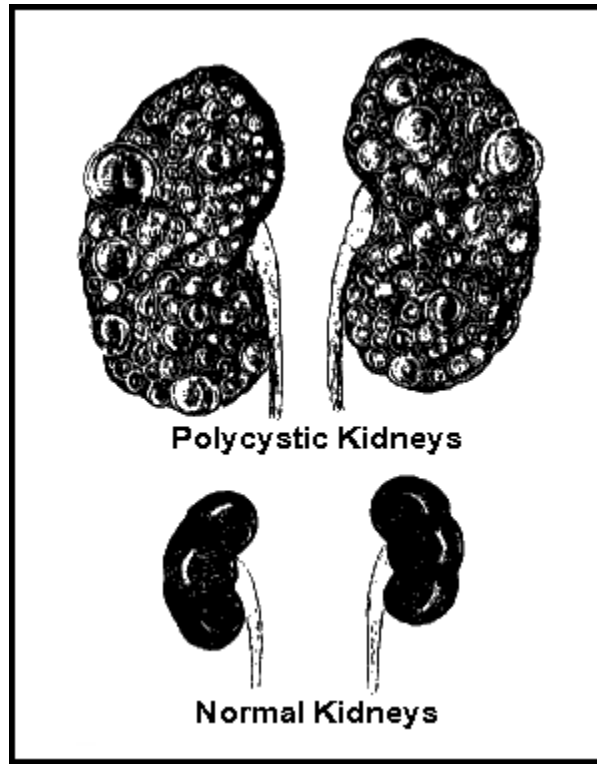


Figure 2-3: Illustrative comparison of polycystic and normal kidneys. [42]

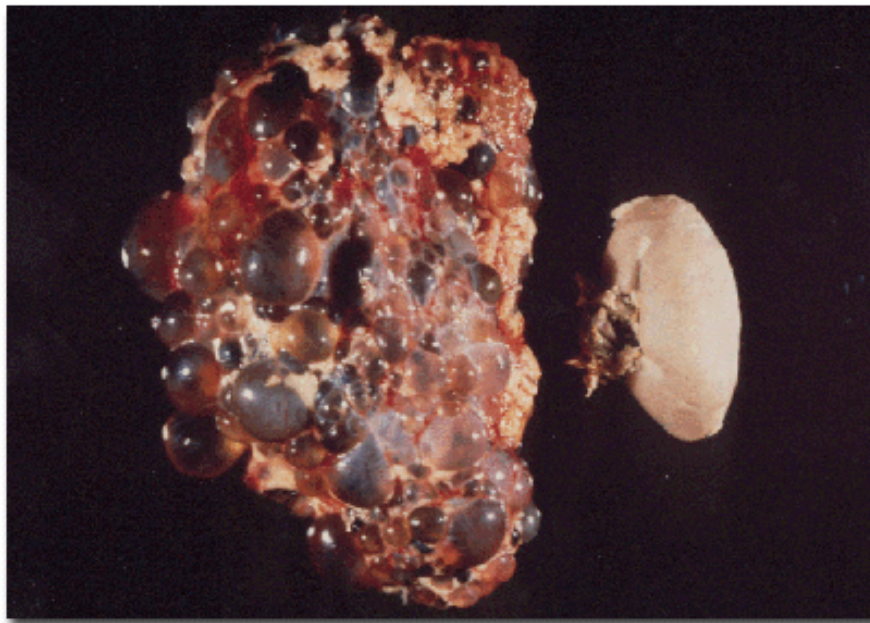


Figure 2-4: Comparison of polycystic kidney (left) with a healthy kidney (right). [29]

number and size of the cysts [29].

The most common clinical finding associated with the disease is flank pain [38]. Hypertension is also a common symptom of ADPKD and has been shown to have an adverse and significant effect on kidney survival [37]. Hypertension is defined as persistent systolic or diastolic blood pressures greater than 150 or 100 mm Hg, respectively. Numerous studies have confirmed the presence of hypertension in ADPKD, and some have suggested that *this* is the most common feature in symptomatic ADPKD [39]. Delaney et al. suggested that hypertension is easily treated; however, it does cause minor end-organ damage [38]. Hypertension is also significantly more prevalent in patients with renal cysts than those without [4].

Intracranial aneurysms have also been classically associated with the disease. [37]. Other symptoms that have also been identified in patients suffering from ADPKD include symptomatic urinary tract infections, gross hematuria, and palpable masses [38]. A number of disorders has been shown to be associated with the disease include gout [43-44] arteriosclerotic cardiovascular disease [45], and colonic diverticulosis [46], and are noteworthy as each condition is a significant cause of morbidity and mortality [37].

Clinical diagnosis has historically been based upon the presence of multiple bilateral cysts [37, 39]. These cysts have been discovered using a wide range of methods, including radiographic findings (excretory urography, angiography, and computed tomography), ultrasound, laparotomy, or surgical exploration. In some instances, polycystic kidney disease may not be diagnosed until an autopsy is performed [37-38]. By using ultrasonographic imaging, the disease may be diagnosed before symptoms develop. If negative ultrasonographic images showing no bilateral cysts continue to

result during early adulthood, there is considerable assurance that a person is not affected [4]. Levels of creatinine in the blood are used to assess disease progression through its evaluation of kidney function; for example, renal functional impairment may be defined arbitrarily as a serum creatinine in excess of 2.5 mg/dL, while end-stage renal disease is defined as a serum creatinine greater than 8.0 mg/dL [38]. However, these values may vary; for example, chronic renal failure has been defined as a serum creatinine in excess of 1.5 mg/dL, while end-stage renal disease may be more broadly diagnosed as any individual requiring dialysis or transplantation [39]. In many patients, serum creatinine levels may remain elevated for a number of years before end-stage renal disease develops [47].

Historical Perspective on Polycystic Kidney Disease

In the 1700s and 1800s, PKD was often diagnosed as Bright's disease. This "disease" actually encompassed any one of several kidney diseases that were marked by high concentrations of protein in the urine. The first documented case of PKD was Stefan Bathory, King of Poland, who lived from 1533 to 1588 [29]. Lejars provided the initial description of the disease in 1888 [48], and in 1957, Dalgaard established that ADPKD is transmitted as an autosomal dominant trait [36]. Although polycystic kidney disease has been the subject of numerous reports since it was first described, major advances were not made until fairly recently [2, 29]. It is also important to note that prior to 1970, cyst punctures were performed and retrograde pyelography was advocated,

which have been shown to distort the natural history of the disease [49-50]. Therefore, the results of series performed prior to the 1970s may not be valid [38].

As medical care and diagnostic techniques have continued to improve, ADPKD has been diagnosed earlier and more frequently since the late 1950s. This has resulted in improved kidney and patient survival for affected individuals. In a study following forty individuals identified between 1935 and 1980, Iglesias et al. presented that patients diagnosed between 1956 and 1980 had an improved survival rate compared to those diagnosed between 1935 and 1955 [37]. Although an antihypertensive therapy with reserpine in the 1950s may have also contributed to the improved survival rate [37], the study suggests that the early diagnosis of adult polycystic kidney disease with modern techniques, combined with adequate medical attention, could possibly improve kidney and patient survival. This study marked the first time the incidence rate of adult polycystic kidney disease was projected. In this study, it was also shown that the presence of hypertension at the time of diagnosis had a significant influence on kidney survival, although it was not statistically shown that this led to an influence on the actual survival of the patient. The presence of impaired renal function also was shown to influence kidney survival, but not patient survival.

In 1985, Delaney et al. presented their results of a group of fifty-three symptomatic adults with APKD studied retrospectively for a mean follow-up of twelve years [38]. In this study, it was suggested that the deterioration of renal function is linear and renal calculi are frequent. It was also demonstrated that urinary tract instrumentation induces serious infection that may cause death, and should be avoided. In contrast with earlier series [51-52], Delaney et al. showed that pregnancy in women with APKD is not

contraindicated when renal function is normal [38]. In conclusion, this study suggested an improved prognosis for survival in the disease than previously reported.

Today, ultrasound is used to diagnose ADPKD before the onset of symptoms in order to determine if renal cysts are present. The presence of renal cysts establishes the diagnosis of the disease at any age. Genetic studies are also conducted in many research facilities; in addition, ultrasounds are continuously conducted on children who may carry the PKD1 gene. These ultrasonographic images are used in conjunction with genotypes inferred from linkage studies in order to diagnose the disease in individuals less than thirty years of age whose kidneys do not exhibit bilateral cysts [4]. However, some individuals may have family data that is insufficient for diagnosis, and in this case, imaging is the only method that may be used. Although a number of imaging modalities exist, the majority of these techniques only provide anatomical information.

Currently, no cure exists for ADPKD. As the disease progresses, the kidneys fail, and dialysis or transplantation is required for patient survival. Through diagnosis at an early age, and by monitoring disease progression, the side effects of this disease may be decreased and the quality of the patient's life may be improved. Recent research efforts focusing on the mutant genes that cause ADPKD have provided an interesting prognosis for the future, as it has even been proposed that gene replacement therapy may be possible based on recent information suggesting that ADPKD is recessive at a cellular level [53].

Magnetic Resonance Imaging and Flow Quantification

Magnetic resonance imaging (MRI) is an established clinical imaging technique, and is constantly being used in new applications, many of which are quantitatively measuring flow velocities throughout the cardiovascular system. MRI is becoming more prevalent for the purpose of obtaining both velocity and anatomic data for larger arteries in the cardiac area, specifically in major arteries directly connected to the heart, as well as the femoral artery [18, 54-56]. Despite the positive results obtained from these studies, the application of this noninvasive imaging modality to the renal arteries has been applied less often in clinical evaluation. Early studies resulted in contrasting conclusions ranging from total lack of agreement to a good correlation between RBF measurements obtained using MRI and other, more established clearance methods used in the early 1990's [57-59]. However, current studies are consistently yielding more positive results [19, 60-62], suggesting that this technique may be used to accurately quantify flow in the renal arteries, in addition to the larger arteries comprising the cardiovascular system.

Phase-Contrast Velocity-Encoded Magnetic Resonance Imaging

Two specific sequences are used in clinical MRI, resulting in two types of images: spin echo and gradient echo. These sequences are used to obtain complementary information pertaining to the anatomy (spin echo) and the motion of blood (gradient echo) in the specific area under observation. Spin echo results in flowing blood

appearing black and is generated by applying an RF pulse that tips hydrogen protons by 90° followed by a second 180° pulse. These types of sequences are used to provide static anatomic information allowing for the differentiation of tissues. Despite only one image being acquired per location, spin echo images have a number of advantages, which will be further discussed in Chapter IV. Gradient echo sequences are produced by applying RF pulses less than 90° and result in images where flowing blood appears white. These sequences are often substantially shorter than those defined as spin echo, allowing breath-hold scans to be performed. Gradient echo sequences provide less anatomical information as compared to spin echo sequences, and are accordingly used to obtain velocity information. As technology has improved, magnetic resonance imaging using a gradient-echo technique with velocity encoding has become a prevalent source used to obtain flow measurements through the aorta and other large vessels in the cardiac system. For the purposes of the present validation study, a gradient echo sequence was used to obtain the flow data using the PVA phantom.

Phase-contrast magnetic resonance imaging (PC MRI), an example of a gradient echo sequence, is an emerging technique for measuring regional blood flow [18-19, 54-62]. A brief summary of the technique is presented here, with a more detailed explanation provided in Chapter IV: Instrumentation and Experimental Methods. This technique is based on the principle that the signal from flowing hydrogen nuclei, relative to those that are stationary, accumulates a phase shift that is proportional to the velocity of flow when passed through specifically-designed magnetic field gradients. When using this type of imaging sequence, two images are acquired: the magnitude image, which provides anatomical information, and the phase image, which is velocity-encoded and

provides velocity information. Numerous phase images are constructed across the cardiac cycle in which the brightness of the voxel is proportional to the blood velocity within that voxel. Regions of interest around a vessel are then defined using specialized software, and the flow rate is automatically calculated based on the specific contour defined.

Numerous studies have been performed showing that phase-contrast velocity-encoded MRI is a technique that provides accurate regional hemodynamic information, both *in vivo* and *in vitro*, which address larger arteries found in both children and adults [10, 18, 54-55, 63-69]. Clinically, this technique has been used to quantify cardiac output, the pulmonary-to-systemic flow ratio, valvular regurgitation, differential lung perfusion, and coronary flow [56]. It has also been shown that shear stresses may be calculated using this sequence when flow encoding is performed in three orthogonal directions [70].

The Application of PC MRI to the Renal Arteries

The use of PC MRI has been proven to be of clinical value in the evaluation of flow in the larger arteries of the cardiovascular system. Blood flow may be measured in vessel cross-sections at various points in the cardiac cycle at high temporal and spatial resolution [54]. However, less experimentation has been performed using this noninvasive technique in renal applications, where smaller arteries are present. In order to quantify flow through the renal arteries previously, Doppler signals were recorded and $^{81}\text{Rb}/^{81}\text{mKr}$ ratios were compared to evaluate renal function [71-72]. Since the early

1990's, both *in vivo* and *in vitro* studies have been performed in order to observe how velocity-encoded MRI may be applied to image the renovascular system.

Sommer et al. showed in 1992 that PC MRI could be used to obtain reproducible noninvasive measurements of RBF [57]. Although a high degree of reproducibility was observed in this study, the MRI measurements of arterial flow did not agree significantly with the standard measurements using the para-amino-hippurate (PAH) clearance technique in nine normal volunteers. However, Sommer et al. did observe a correlation of 0.86 between the RBF estimated using MRI and the RBF calculated using the PAH-clearance method from the left renal vein.

More promising results were presented in 1993 by Lundin et al. [59]. Using two different RBF measurements found using MR angiography (sum of flows in right and left renal arteries and difference between supra- and infrarenal abdominal aorta flow), they found the correlation coefficient between the two flow rate calculations to equal 0.72. A comparison of the MR results and expected RBF measurements found using the PAH clearance was made, and agreement was observed among the values. Based upon their results, Lundin et al. also suggested that noninvasive RBF measurements were possible using PC MRI methods.

In the same year, Wolf et al. further suggested that cine PC MRI was a promising technique for measuring blood flow when applied to the renal arteries [58]. Using a total of ten healthy adult volunteers, flow data using velocity-encoded MR images was again calculated by measuring the difference between suprarenal and infrarenal aortic flow. Individual arteries were also imaged in order to obtain through-plane flow. These results were then compared to RBF measurements found using the PAH-clearance method.

Wolf et al. pointed out in their discussion that the PAH-clearance method has a number of limitations. When using this method, only healthy subjects with normal renal function may be monitored, temporal resolution is poor, and most importantly for the purposes of a number of renal diseases, the kidneys cannot be studied separately. The PAH-clearance method would not allow observation of patients with impaired renal function.

Measurements of the individual renal arteries resulted in more correct results than the flow data calculated using the aortic subtraction method, as compared to the PAH-clearance values. Wolf et al. also emphasized the importance of minimizing the velocity encoding value and reported that more accurate results were obtained as the velocity encoding value was decreased.

In 1994, Debatin et al. [73] used a cine PC MRI sequence, in addition to two breath-hold PC techniques, to determine the most correct method of obtaining reliable RBF measurements. After performing *in vivo* and *in vitro* experiments, they were able to show that it was possible to acquire consistent RBF measurements using breath-hold PC MRI. For the *in vivo* study, the PAH clearance technique was again used as the established method for comparison to the MRI data in eight patients. Based upon their results, Debatin et al. commented that breath-hold sequences were significantly more accurate than conventional cine PC sequences both *in vivo* and *in vitro*. Overestimation of flow resulted from the use of the cine PC technique.

In the three studies presented above, flow rates obtained using MR were compared indirectly with measurements obtained using MR imaging of the aorta [59] and/or through clearance techniques [57, 59, 73]. In 1997, Schoenberg et al. surgically implanted transit-time ultrasound flow probes in seven foxhounds to compare MR

measurements more directly to a specially-designed cine PC MR protocol [60]. When the cine PC MR results were statistically compared to the flow probe data, a correlation coefficient of 0.99 resulted. Through the results of this study, Schoenberg et al. were able to show that cine PC MR could be used to provide a reliable quantification of RBF. They also commented that this technique proved to be sensitive to hemodynamic changes and provided an accurate assessment of the pulsatile flow signal. With such a strong correlation between the two techniques, Schoenberg et al. suggested that their cine PC MR protocol had the potential to be a reliable method for obtaining a quantitative and qualitative assessment of RBF, thereby one day replacing the invasive measurement techniques widely used at that time.

In 2000, de Haan et al. presented their results focusing on the differences observed when using breath-hold and respiratory-triggered PC MRI [61]. Using twelve healthy subjects, they found that both techniques were valid and reproducible, although results obtained using the breath-hold method were slightly more accurate. De Haan et al. also used the difference in aortic flow measurements above and below the renal arteries as their validity control. It was emphasized in this report that further and larger studies, which included the observation of diseased patients, were required prior to the extensive application of this technique to quantitative imaging of the renal arteries.

De Haan et al. published their results from a follow-up study using the $^{133}\text{Xenon}$ -washout procedure as an independent comparison method in 2003 [62]. This report described the results of a much larger study, which included fifty-three patients suspected of having renovascular disease. Up until this time, no large-scale studies on diseased patients had been performed. De Haan et al. again showed that a significant correlation

existed between PC MR and an independent control method ($^{133}\text{Xenon}$ -washout procedure). In contrast, they pointed out that the MR data did not compare well with the severity, or presence, of renovascular disease using angiography. Based upon their results, de Haan et al. stressed that the PC MR technique required further experimentation and improvement before its clinical application on a larger-scale.

Finally, in 2003, King et al. presented a comprehensive study using one hundred twenty-seven patients diagnosed with ADPKD [19]. A large amount of information was acquired during this study, including both anatomic and hemodynamic data. The *in vivo* flow data acquired using a 2D cine phase-contrast breath hold sequence was found to be both valid and reproducible. King et al. also demonstrated that compromised flow in the renal arteries correlated with other anatomical and functional characteristics of ADPKD severity. As a result, they suggested that MR has great potential for investigating hemodynamic changes that occur with disease progression, and may be more widely applied in the future with additional experimentation.

The studies discussed in this chapter have all presented important information that have contributed to the advancement of noninvasive imaging techniques, specifically as applied to the renal arteries. It is important to note that many of these studies were limited by small sample sizes. Although nearly all reports presented promising results, the accepted standard used to image the renal arteries is still contrast angiography [74], which may be performed using a variety of modalities including sonography, computer tomography, and MR. Currently, the preferred MR angiography (MRA) technique is high-resolution 3D gadolinium-enhanced MRA [61, 75]. In addition to the requirement of contrast agents, these modalities have certain limitations, as they rely on morphologic

assessments of the arteries [73]. PC MRI allows a noninvasive quantitative evaluation of flow dynamics to be performed, which cannot be achieved using angiographic techniques.

Because there is a growing population of individuals being diagnosed with ADPKD, as well as other renovascular diseases, the ability of diagnostic imaging modalities to provide both anatomical and functional information pertaining to the renal arteries is of particular importance. MRI is ideally suited to become the primary imaging modality for the patient population affected by this disease, as it can provide a large amount of information (velocity data, flow quantification, cyst volume, and kidney volume) obtained during a single scan session. MRI is also noninvasive and biologically harmless, which may further increase patient cooperation in clinical studies. Because of its numerous applications in comparison to its few limitations, MRI has the potential to be the imaging modality of choice in the future for the purposes of quantifying flow, as well as for other anatomical and functional purposes, throughout the many areas of the cardiovascular system. Although numerous studies have been performed using PC MRI to image the cardiovascular system, the focus has been on larger arteries. In addition, the majority of the studies on renal arteries concentrate on using PC MRI to obtain data from healthy adults. A substantial amount of RBF data does not exist for diseased individuals or children. Thus, the present validation study aims to formulate a protocol that may be applied to the renal arteries, in healthy and diseased populations of both children and adults.

CHAPTER III

HYPOTHESIS AND SPECIFIC AIMS

The long-term goals of the CRISP study include the ability to more completely understand how MRI may be used to assess renal circulation and the role that hemodynamic changes have in renal disease progression, specifically in ADPKD. King et al. have shown that a significant correlation exists between the anatomical and functional indicators of ADPKD disease severity and the hemodynamic parameters measured in the renal arteries [19]; however, the mechanism behind this correlation must be further understood in order to develop an effective preventative treatment program. In order to ensure that these *in vivo* measurements are as accurate as possible, a number of experiments must be performed *in vitro*. These experiments will result in the determination of an effective protocol for assessing the wide range of individuals this disease affects. By combining the knowledge gained from both *in vitro* and *in vivo* studies, methods to monitor disease progression and the development of a treatment plan to reduce the effects of rapidly changing hemodynamic parameters may be developed. The present study uses current MR techniques to test the following hypotheses and achieve the detailed specific aims described in the following pages.

Hypothesis I

The first hypothesis of this study is that polyvinyl alcohol (PVA) is a superior phantom material for modeling vascular tissue in MR flow simulations.

The specific aims resulting from this hypothesis are:

Specific Aim 1:

To investigate MR velocity results from:

- (a) PVA cryogel,
- (b) Plastic tubing (vinyl, containing polyvinyl chloride compounds), and
- (c) Glass models

in order to establish the most accurate material for modeling human vessels.

This aim will be achieved through *in vitro* experiments. A phantom will be designed using a block of PVA constructed with six hollow channels. MR measurements will be taken through the center of this cryogel block, as well as through plastic tubing exiting the phantom to capture flow characteristics through both materials. These results will be compared to results previously obtained in this and other studies to determine the most precise material for the validation study.

Hypothesis II

The second hypothesis of this study is that breath-hold velocity-encoded MRI is capable of producing highly accurate flow measurements for the physiological range and dimensions of renal arterial blood flow.

The specific aims resulting from this hypothesis are:

Specific Aim 2:

To investigate the ability of MR to accurately determine velocity and flow in renal arteries.

This aim will be achieved through *in vitro* MR studies using a PVA cryogel phantom. The resulting measurements will be compared to actual flow calculated using collected volume by weight determination.

Specific Aim 3:

To formulate an effective protocol resulting in precise flow measurements, which may be applied to *in vivo* studies and further used to quantify hemodynamic changes in patients with renal insufficiency.

This aim will be achieved using a breath-held phase-velocity encoded protocol with the PVA cryogel phantom. A number of parameters will be tested in order to

determine exactly which protocol provides the best results and should subsequently be used in patient studies and treatment.

CHAPTER IV

INSTRUMENTATION AND EXPERIMENTAL METHODS

In this chapter, the experimental model, the *in vitro* flow loop, and the experimental techniques and protocol are discussed. The process for analyzing the data collected during the various magnetic resonance (MR) experiments using a breath-held gradient-echo technique is also explained in detail.

In Vitro Model

The experimental model (Figure 4-1) used in this validation study was a square box made of cast acrylic sheets (constructed by J.M. Machining, Lawrenceville, Georgia). The box measured 24.13 x 24.13 x 6.99 cm, and was made of 9.52 mm cast acrylic with a 6.35 mm cast acrylic lid held in place with plastic flat head screws. Adhesive was used to glue the cast acrylic sheets together forming the square casing. Six holes of decreasing diameter were machined onto opposite sides of the box into which six Teflon tubes with six different diameters were inserted. The diameters of the holes were as follows: 3.18, 4.76, 6.35, 7.94, 9.52, and 11.11 (± 0.01) mm. These diameters were

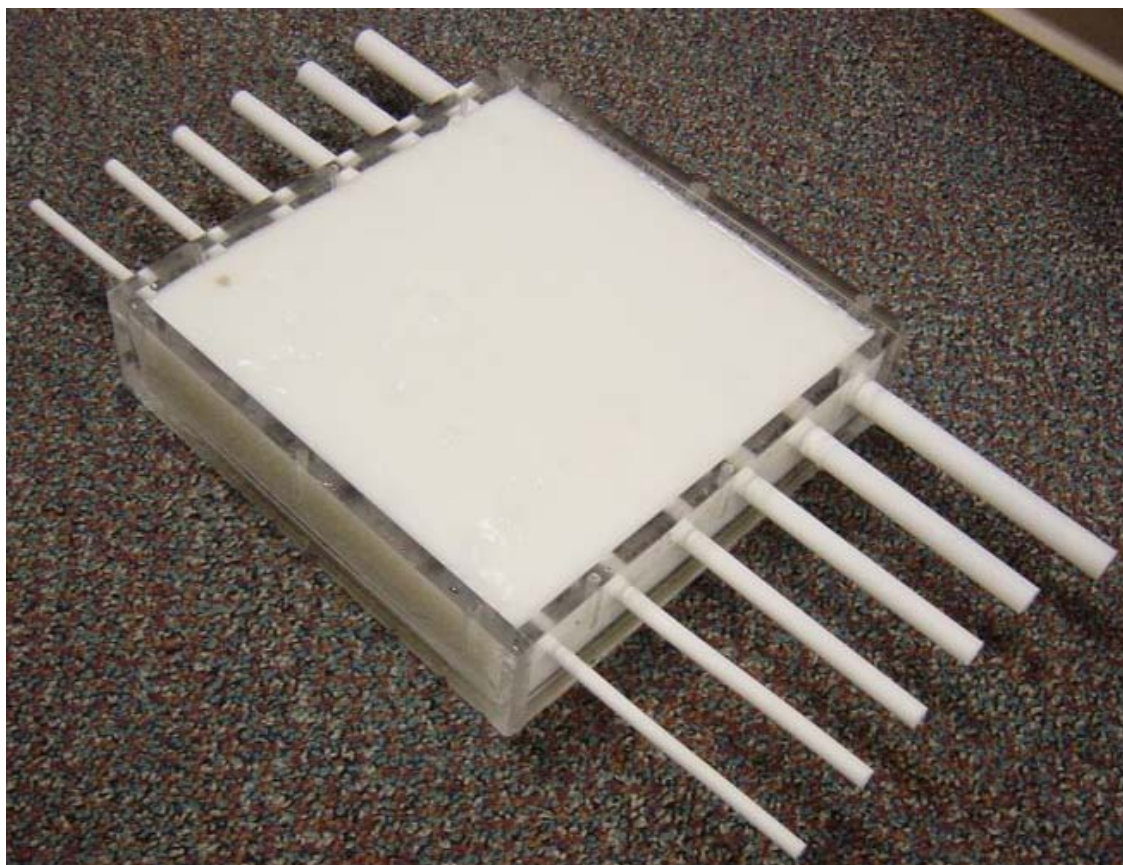


Figure 4-1: PVA phantom used in validation experiments. The model was constructed with six hollow channels running through the PVA ranging in diameter from 3.18 to 11.11 (± 0.01) mm. PVA proved to be the superior choice among other possible phantom materials during initial experimentation.

chosen to simulate the full range of vessel diameters encountered in renal arteries in both a healthy and diseased population of children and adults [73].

In the process of validating renal blood flow measurements from magnetic resonance imaging (MRI), various model materials were evaluated. Initial experimentation was performed using polyvinyl alcohol (PVA), vinyl tubing, made of polyvinyl chloride (PVC) compounds, and glass. These results are presented in Chapter V, and as shown, results from the vinyl tubing and plastic did not prove to be as accurate as PVA in terms of resulting MRI data. After these initial results were evaluated, PVA was selected as the material of choice because of its mechanical and magnetic properties for simulating vessel lumen in *in vivo* blood flow measurements [25]. The chemical structure of PVA is shown in Figure 4-2 for reference purposes.

PVA was first recognized to have medical applications by Nambu in 1982 [76]. Since that time, it has been reported to be ideal for a number of different medical purposes. PVA has been used as a skin marker in MR [77-78] and x-ray imaging [77, 79], a transmission pad in radiofrequency thermal therapy [80], a conductive electroretinographic membrane [81-83], a bandage for burn victims [84-85], a substitute for an ice bag [86-87], and other medical applications [88-89]. Most importantly, for the purposes of this study, PVA has been shown to be ideal as an MR quality control phantom material [25-28], as PVA yields enough free protons to yield above-noise signals with most MRI pulse sequences, unlike glass, plastic and rubber. The strength and elastic characteristics of this material are also mechanically comparable to the vessel wall [25]. In 1997, Chu and Rutt described how PVA is inherently flexible and tough, and it has similar elastic properties and MR relaxation times to those of porcine aortas.

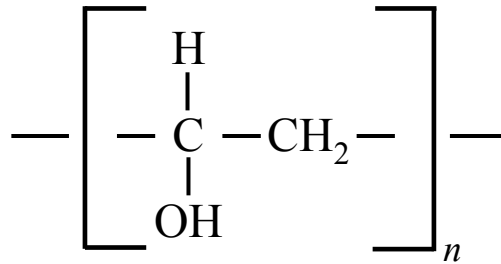


Figure 4-2: The chemical structure of the polyvinyl alcohol molecule. PVA has been reported to have a number of significant medical applications including its use in MR quality control phantoms.

These relaxation properties are stable over a six-month period of time [26], and although some researchers feel that more than six months is required for an MR quality control phantom to be of clinical use and significance [90-91], it is important to note that this material may be easily reproduced in a fairly short amount of time.

The specific PVA cryogel used in this study was created by freezing and thawing an aqueous PVA solution. During these freeze-thaw cycles, cross-linking occurs through hydrogen bonding with hydroxyl groups between the PVA molecules. This cross-linking determines the strength characteristics of the rubber-like gel material. Strength characteristics may be altered using chemical cross-linking, initiated through the addition of compounds such as aldehydes or borates [92]; however, for the purposes of this study, an aqueous PVA solution proved to be the best choice. In chemically altered PVA cryogels, the result is that of a gel having the appearance and strength similar to common gelatin [25], which would not be suitable for a phantom material as needed in the present experimental study.

Evaluation of Materials

In order to determine which material would provide the most accurate results for this validation study, three materials were evaluated: clear vinyl tubing composed of polyvinyl chloride (PVC) compounds, glass, and polyvinyl alcohol (PVA). In order to assess the accuracy of these materials, experimental flow rates resulting from the phase-velocity image analysis described above was compared to the experimental flow rates at a 200 mm field of view (FOV). Results for the clear vinyl tubing and the PVA were compared to the flow rates presented in Table 4-1 for channel diameters of 3.18, 4.76, and 11.11 mm, as the vinyl tubing was most perpendicular to the scan plane in these instances. Data for these materials was taken simultaneously using the procedure described later in this chapter. Using the same analysis methods described with the FLOW software package, a glass model from a previous study [93] was used as a third material for comparison. The vinyl tubing continued to be imaged throughout the validation study after initial experimentation in order to further demonstrate the superiority of PVA.

PVA Preparation

Once it was shown that PVA is a superior phantom material for the purpose of MRI research, the most effective procedure and ratio of PVA to water in the cryogel solution had to be determined. In order to address this issue, two phantoms were made using different amounts of PVA in each (20% and 30%). Three different sizes of beakers

were also used to determine the best method of autoclaving the solution. The flow loop described in the next subsection was set up in an experimental laboratory, and each phantom was placed inside the cast acrylic box and incorporated into the flow loop. The performance of each phantom was observed during this “dry” experimental run, and the amount of leakage by the phantom was especially noted.

In order to create a mold that would be of sufficient strength and elasticity to retain its shape under fluid pressures encountered *in vivo*, a solution of 30% hot-water soluble PVA and 70% water was used. The polyvinyl alcohol slab was formed using 2500 ml of the aqueous PVA solution. After the solution was mixed, it was autoclaved on the liquid cycle for thirty-five minutes to allow it to go into solution, as the PVA used in the phantom construction is only soluble at higher temperatures. After testing with various sizes of autoclavable containers, it was found that using 1000 ml beakers with 500 ml of solution in each was the most appropriate method, preventing spillover during the autoclaving process. The resulting solution was then poured into the cast acrylic casing, where six Teflon tubes of corresponding diameter had been inserted into their appropriate straight holes. Care was taken in pouring the solution into the casing as to not allow any air bubbles to form in the area to be scanned. Air bubbles were also removed before beginning the freeze-thaw cycles. Once the solution had been poured into the casing, the lid of the case was attached with metal screws. The entire phantom was then placed into a freezer to begin freeze-and-thaw cycles. These cycles occurred at twelve-hour intervals, and were placed in water at room temperature during the thaw cycle to ensure that the PVA would not lose its mechanical properties. According to Chu and Rutt, the length of time frozen does not have a large influence on the properties of the

PVA [25]. The time intervals were chosen to ensure that access to the freezer would be available. Four freeze-and-thaw cycles were used, as research suggests that additional cycles would make no substantial difference in the PVA properties. It was also noted that a minimum of four cycles was required to allow cross-linking to occur throughout the entire model. Once the freeze and thaw cycles were completed, the PVA phantom was stored in water at room temperature to maintain its properties. The metal screws used during freeze and thaw cycles were also replaced with those made of plastic before the phantom was placed in the scanner, ensuring MRI compatibility and reducing the incidence of artifact.

Steady Flow Loop

A steady flow loop was created in order to allow flow quantification to be made using MRI. A schematic showing the setup for the 9.53 mm experiment is shown in Figure 4-3. The fluid used in the experiments matched the kinematic viscosity of blood ($3.5 \pm 0.1 \text{ cSt}$) and was a solution of 40% glycerin and 60% water by volume. Teflon tubing was inserted into the casing described in the previous subsection to serve as entry length tubing, ensuring fully-developed flow within the model. These tubes were inserted through the holes in the casing, approximately one inch into the PVA mold. The proper entry lengths were calculated according to Equation (4-1),

$$L = 0.03 \times \text{Re} \times D \quad (4-1)$$

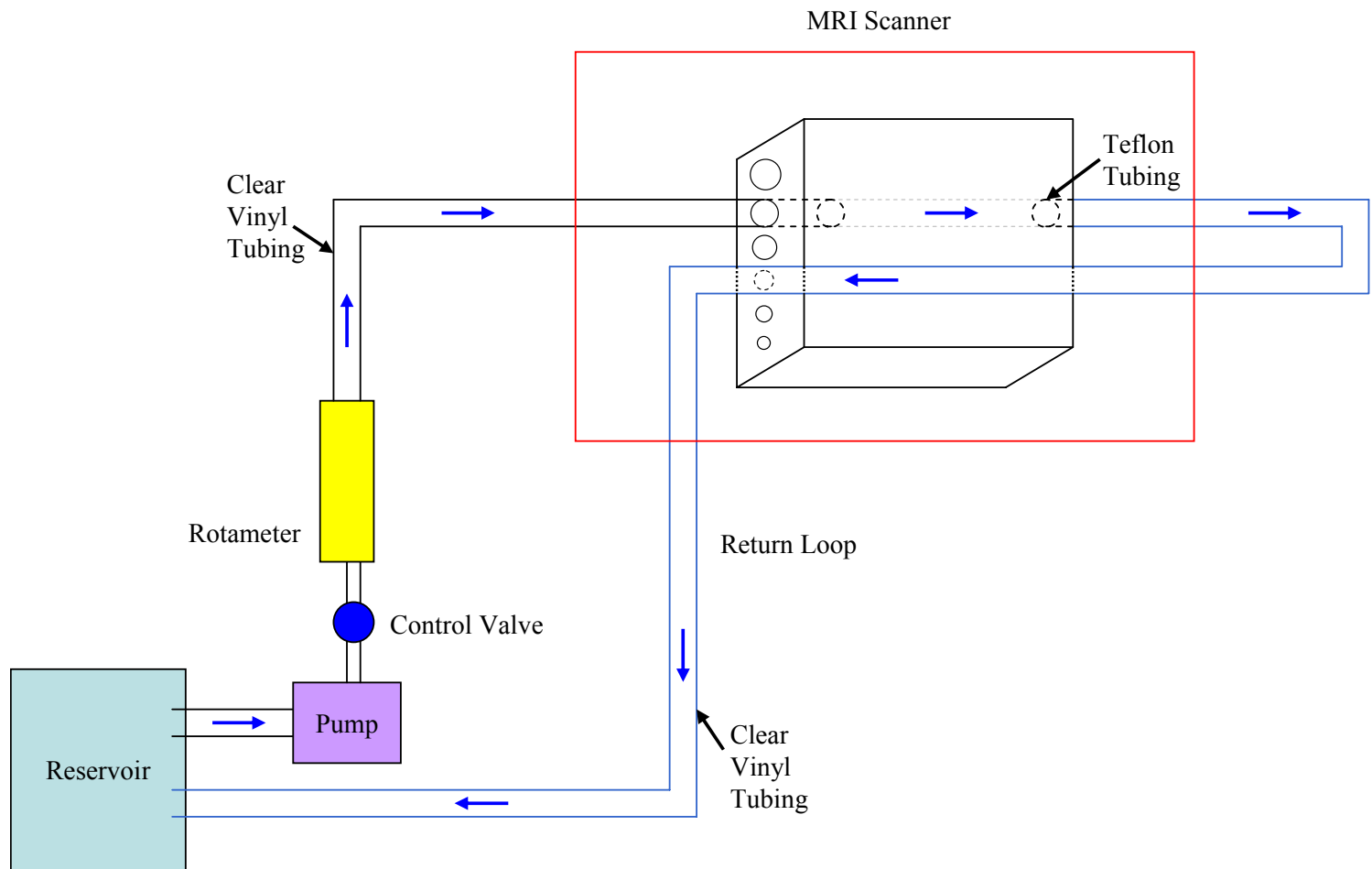


Figure 4-3: Flow loop used in steady flow validation experiment. This schematic shows the setup for the 9.53 mm experiment. It is also important to note that PVC tubing was returned over the phantom model in order to capture flow through the vinyl (PVC) tubing for comparison of material experiments. The same set of PVC tubing would have also been used for the 11.11 mm experiments.

where Re is the Reynolds number and D is the inner diameter of the tube. The Reynolds number was calculated using Equation (4-2),

$$Re = \frac{VD}{\nu} \quad (4-2)$$

where V is the velocity, D is the diameter, and ν is the kinematic viscosity of the fluid in centiStokes. In these calculations, a kinematic viscosity of 3.4 centiStokes was used. Based upon the entry length calculations, the range of entry lengths varied from 3.74 to 22.47 cm using the kinematic viscosity stated above. Therefore, all entry lengths were cut to be 25 cm to ensure fully-developed flow at all possible rates of flow and to account for slight variations in fluid viscosity. Temperature was also monitored to maintain accurate viscosities throughout the duration of each experimental trial using a standard thermometer (Enviro-Safe -20 to 110°C, H-B Instrument Company, Collegeville, PA). The temperature of the fluid was maintained at 21°C by keeping the pump iced accordingly.

In order to make the appropriate connections to the six different inlets, three different sets of flexible vinyl tubing subsections were made, which could be integrated into the main flow loop. Each subsection was created so that it would fit onto the inlet and outlet Teflon tubing of two consecutive diameters. Fluid was run through one channel at a time with only that channel integrated into the main flow loop.

For every diameter existing in the model, six flow rates were tested, resulting in thirty-six sets of scans ranging experimentally from 120 to 1190 ml/min. Beginning with the smallest diameter of 3.18 mm, flow rates were tested from 120 to 760 ml/min at

increments of approximately 100 ml/min. Flow rates were measured with a rotameter (model 6B0202, Dakota Instruments, Monsey, NY and model H404020030, Bel-Art Products, Pequannock, NJ) that was placed directly after the adjustable control valve in the experimental flow loop. The return outlet of the phantom model drained into the same initial reservoir, from which the fluid was pumped via a submersible pump (model number 550, Little Giant, New Haven, CT). True flow rates were calculated by weighing the fluid from the return loop over a one-minute interval. With the exception of the highest two flow rates in the 11.11 mm experimental trial, fluid was collected both before and after each scan set to ensure accurate true flow determination.

Fluid Analysis

During each scan session, one simulated vessel was used for experimentation. The collected fluid obtained from the return loop was transported away from the scanner and taken to a separate experimental laboratory within Emory University Hospital in order to prevent any spills in the scanner room. As previously discussed, fluid was collected twice at each flow rate for each simulated vessel. One sample measuring 500 ml of fluid from the reservoir was then measured and weighed using a standard balance (model TM3000, Mettler Toledo, Columbus, OH). Once the resulting weight of the sample had been recorded, each individual fluid sample for each rate of flow was weighed and the volume was calculated, resulting in two experimental flow rate values (ml/min) for each flow rate. These values were then averaged and the resulting volume was used as the true

flow rate, which served as the baseline in the MRI validation. The two measurements taken for each flow rate were all within 3% of one another, the majority of flow rates being within 1%. The resultant flow rates are shown in Table 4-1. Please note that two fluid samples were not collected during experimentation with the two highest flow rates for the largest diameter (11.11 mm). This was due to higher flow rates used and size limitations of the fluid collection apparatus. For these two flow rates, sampling occurred before the scans began.

Table 4-1: Experimental flow rates measured using the weight determination method. The listed flow rates are an averaged value of the fluid collected prior to the first scan and after the last scan, with the exception of the two highest flow rates for the largest diameter of 11.11 mm.

		Channel Diameter (mm)					
		3.18	4.76	6.35	7.94	9.52	11.11
Flow Rate (ml/min)		123.35	278.09	336.95	477.22	532.07	694.37
		242.13	411.72	457.93	573.09	706.87	796.64
		377.96	510.04	654.48	691.37	795.88	851.56
		397.69	660.25	686.06	787.15	808.22	919.18
		531.19	771.37	743.88	896.50	964.40	1010.44
		764.94	864.22	869.91	979.08	1142.15	1189.41

Principles of Magnetic Resonance Imaging

Nuclear magnetic resonance (NMR) tomography, now recognized as MRI, is based upon the principle of NMR. Although the word "nuclear" was dropped from the term "MRI" in the late 1970s, as to not associate MRI with ionizing radiation, the occurrence of this technique actually originates in the nuclei of atoms. In clinical MRI today, magnetic fields and radiofrequency energy are most frequently used to stimulate hydrogen nuclei in selected regions of the body. Hydrogen is one of many NMR active elements. Other biologically important elements that share this characteristic include carbon, nitrogen, oxygen, fluorine, sodium, phosphorous, chlorine, and potassium [94]. As these hydrogen nuclei are stimulated, they emit radio waves that are then used to construct images [69]. These MRI signals have frequency, amplitude, and phase components, just as other types of waves.

The principle of NMR is established by two main properties: nuclear spin and also that moving charged particles give rise to a magnetic field (Figure 4-4). Nuclear spin causes elementary particles, which are contained in nuclei, to have an intrinsic magnetic field associated with them. In the absence of an external magnetic field, these particles (protons) are in complete disarray; however, if they are placed in a strong magnet, they will have a tendency to align in the presence of an external magnetic field. For protons, only two alignments are possible using an applied magnetic field: either with the field (lower energy state) or against it (higher energy state) (Figure 4-5). The difference

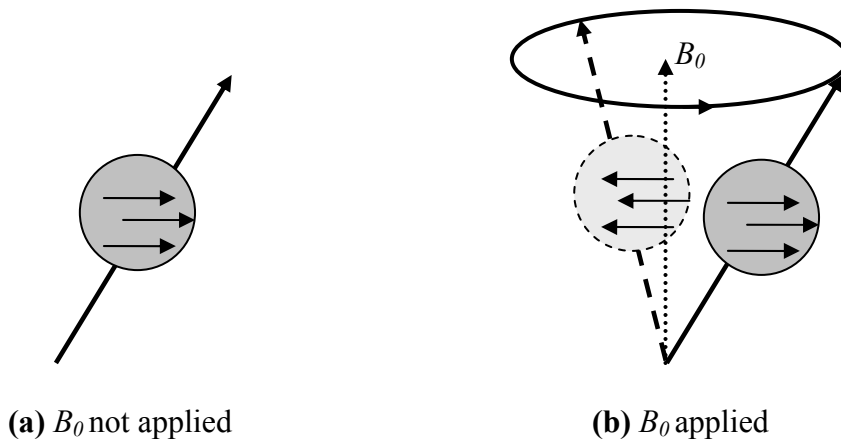


Figure 4-4: This diagram displays the two main properties of NMR. **(a)** In the absence of an external magnetic field, a hydrogen proton has an intrinsic magnetic field due to the property of nuclear spin. **(b)** When an external magnetic field (B_0) is applied, the spinning proton not only spins about its own axis, but also around the axis created by the applied magnetism.

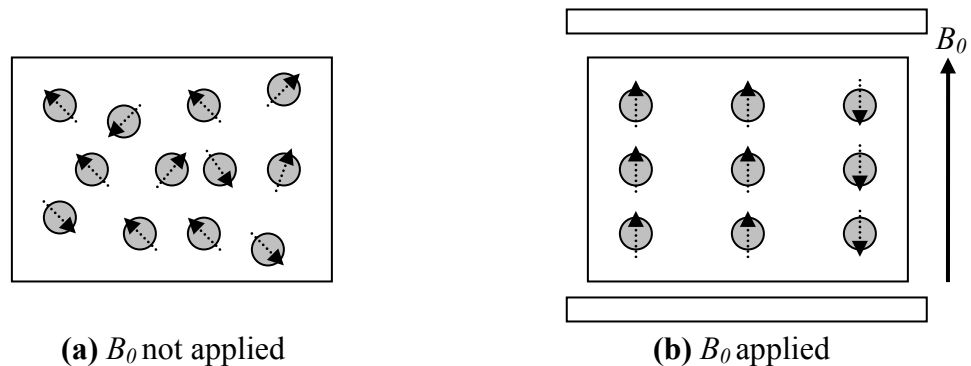


Figure 4-5: **(a)** A representation of the chaotic array of hydrogen protons when an external magnetic field (B_0) is absent and **(b)** the alignment that occurs when the magnetic field is applied. In **(b)**, the bars above and below the protons represent the poles of the magnet. In MRI, protons may either align with the direction of the magnetic field or against it, resulting in two different energy states. In this example, when B_0 is applied, the first two columns represent the lower energy state, as these protons align in the direction of the external magnetic field, while the last column represents the higher energy state.

between these two energy states is directly proportional to the strength of the external magnetic field and is governed by Equation (4-3),

$$\Delta E = \gamma B_0 \quad (4-3)$$

where γ is the gyromagnetic ratio of the nucleus and B_0 is the strength of the external magnetic field. For a proton, γ equals 1.7×10^{-7} eV/T (42.58 MHz/T). When using an applied magnetic field of 1.5 T, the energy difference as described in Equation (4-3) is equivalent to 2.6×10^{-7} eV. This is approximately one ten-billionth of the energy used in X-ray and nuclear medicine.

In order to perform an MRI experiment, radiation must be sent into the protons in a specific sample at the frequency at which they will absorb the radiation. This frequency is identical to the energy difference between the two possible alignment states, and in the case of the 1.5 T applied magnetic field, this frequency would be 63.87 MHz (2.6×10^{-7} eV). The radiation is only applied for a short time and is referred to as a radiofrequency radiation (RF) pulse. After the sample is excited, it emits an RF signal that must be received and quantified in order to produce the MRI image. The transmission of the excitation pulse and the receiving of the resulting RF signal are performed by the RF coil, which acts as both a transmitter and receiver. For each and every MRI study, a number of steps are taken. A pulse sequence is selected, an image location is chosen, and image data is acquired in order to address specific questions relating to each individual case. Each pulse sequence is defined in order to determine how the magnetic field gradients are applied during image acquisition.

During the past fifteen years, clinical MRI has evolved from a modality that was restricted to anatomic imaging to one that also provides functional information. Two specific sequences are used in clinical MRI, resulting in both types of images: spin echo and gradient echo. Spin echo results in flowing blood appearing black and is generated by applying an RF pulse that tips hydrogen protons by 90° followed by a second 180° pulse. These types of sequences are used to provide static anatomic information. Although only one image is acquired per location, spin echo images have a number of advantages. These include high spatial resolution, blood-tissue contrast, and decreased artifact caused by metallic biomedical implants [56]. Gradient echo sequences are produced by applying RF pulses less than 90° and result in images where flowing blood appears white ($+v_{max}$). At $v = 0$, the image appears medium gray, and at a maximum “negative” velocity ($-v_{max}$), the image is black. These sequences are often substantially shorter than those defined as spin echo, allowing breath-hold scans to be performed. Multiple images may also be acquired over the cardiac cycle in each predetermined location, allowing flow characteristics to be defined and arterial and ventricular function to be assessed.

Phase-contrast magnetic resonance imaging (PC MRI), an example of a gradient echo sequence, is an emerging technique for measuring regional blood flow [17-18, 54, 56, 60-61], and is used throughout this renal phantom validation study. PC MRI is also referred to as phase-velocity cine MRI (PVC MRI) and velocity-encoded cine MRI [69]. The ability to acquire quantitative measurements of blood flow non-invasively is a valuable tool that has resulted from improved technology. In order to obtain the flow characteristics through a vessel, an image plane is oriented perpendicular to the direction

of flow through the vessel. A cross-sectional image with velocity encoded in the through-plane direction results, and both the modulus, or magnitude, and phase images are acquired at various points during the cardiac cycle. The modulus image provides information about the anatomy of the patient, while the phase image contains the velocity information.

PC MRI is based upon the principle that the signal from hydrogen nuclei, such as those found in the blood, accumulates a predictable phase shift, which is proportional to flow velocity. The fact that spin echoes resulting from magnetization moving along a magnetic field gradient experience phase shifts was recognized early with the use of MR [95]. In PC MRI, specially designed magnetic field gradients, whose strength varies linearly in the direction of blood flow, are briefly applied to the specific location being examined. Protons at different locations along the gradient develop phase differences, as a result of the rate of proton precession (complex rotation of the spinning proton) being proportional to the strength of the magnetic field. The gradient is then reversed, giving it opposite polarity. No net phase shift is acquired by nuclei in stationary tissue because the gradient cancels out any phase change, and therefore, this tissue appears gray. However, moving protons experience a different gradient strength when the second gradient is applied. The application of this bipolar gradient results in a net phase shift (φ) being accumulated proportional to the velocity of the protons in the velocity-encoded direction. This is governed by Equation (4-4),

$$\varphi = \gamma \cdot v \cdot \int G(t) dt \quad (4-4)$$

where v is the velocity and $\int G(t)tdt$ is the first moment of the gradient $G(t)$ in the direction of flow [60, 69]. Moving fluid is displayed through the intensity of each voxel in the phase image and may appear bright or dark, depending on the direction of flow. Background phase shift phenomena may be attributed to a lack of homogeneity in the magnetic field and other factors, resulting in inaccurate images. These effects may be accounted for by acquiring a second set of phase data without velocity encoding. By subtracting the two sets of phase data from one another, the background error may be removed, resulting in more accurate results [69].

Velocity encoding may also be performed in all three orthogonal planes (RL, AP, FH); however, these studies are performed with less temporal resolution. This type of encoding results in three phase images at each point measured during the cardiac cycle and was used in this renal validation study in order to determine flow characteristics and establish any deviation from steady, laminar flow.

Magnetic Resonance Imaging Techniques and Protocol

Four main studies were performed using the PVA validation phantom and the steady flow loop described in this chapter, in addition to the MR studies performed using different materials. All experiments were performed using a gradient-echo sequence, specifically using multi-shot echoplanar imaging (FE-EPI). These studies include a comparison among high-resolution protocol at various fields of view, an assessment of the variations in low- and high-resolution scans, a multi-site study, and a study observing

the effects of velocity encoding in three directions. All studies were performed on the Philips Gyroscan Intera 1.5 T scanner located at Emory University. The 4-element, phased array body coil was used to transmit and receive RF signals. Cardiac triggering of the MRI acquisition was performed using the Philips' built-in physiology simulation software. The high-resolution and low-resolution breath-held 2D PC MRI protocol, listed in Table 4-2, was used at each flow rate with a 160 x 160, 200 x 200, and 350 x 350 mm field of view (FOV). These will be referred to as the 160, 200, and 350 mm FOV from this point forward. Visually defined perpendicular planes were also imaged in three locations along each channel using the high-resolution protocol at 200 mm FOV in order to study repeatability and to also ensure a uniform velocity profile along the length of each simulated vessel. A study was also performed using a gradient echo protocol with velocity encoding in three directions at 240 x 240 mm FOV to assist in determining the best possible protocol to use in clinical investigation.

Table 4-2: Imaging parameters for the gradient-echo breath-held velocity-encoded acquisitions.

	Low-Resolution	High-Resolution	Velocity Encoding-3 Directions
TR (ms)	21	24	24
TE	11	11	11
Flip Angle (°)	35	35	35
Phase Encoding Views	96	192	192
Phases (across cardiac cycle)	16	16	12
Image Size	256 x 256	256 x 256	256 x 256
Field of View (mm x mm)	160 x 160, 200 x 200, 350 x 350	160 x 160, 200 x 200, 350 x 350	240 x 240

Magnetic Resonance Image Analysis

Phase-velocity encoded protocol results in two images: the modulus and the phase difference images. After each scan session was completed, all resulting image data was transferred to a Sun analysis workstation (Sun Blade 100, Sun Microsystems, Mountainview, CA). The flow analysis was performed using the FLOW software package (University of Leiden, The Netherlands). The definition of the lumen borders was performed manually first in the magnitude map and then the phase difference (velocity) map using the drawing tools provided with the FLOW software program. The contours were drawn into the magnitude map based on visual perception of where the lumen boundary existed, while a velocity of 0 cm/sec was used to define the contours in the velocity map. A third flux region was then defined using the software's built-in contour detection program on the phase-velocity map. This required the manual identification of a center point (using the "point" edit tool) inside the cross-section of each phase image acquired across the cardiac cycle. A fourth region of interest (ROI) was drawn in a C-shape around the simulated vessel in order to correct for any static velocity components resulting from DC phase errors in the image background. Data processing for the four regions of interest took approximately ten minutes for each scan. A typical image of the screen layout observed using the FLOW software package after manual and automatic contour definition is shown in Figure 4-6. Flow rates were calculated with and without the inclusion of the fourth region in order to observe any constant velocity errors that were present across the image. Instantaneous flow was first calculated from the information contained in the phase-velocity maps by integrating the

flow velocity values for each pixel within the first three regions of interest, with and without background subtraction. Total flow per minute was then calculated by integrating these instantaneous flow values for each acquired phase across the complete cardiac cycle and multiplying by the heart rate in beats per minute as defined by the physiological simulation built into the Philips' scanner. Flow rates were calculated for each region of interest in each image to evaluate both the manual and automatic methods.

Manual and automated image analyses were performed by two blinded independent observers for high-resolution scans at 160 and 200 mm FOV for all simulated vessels at a mid-range rate of flow (Table 4-3) to assess interobserver variability. To assess intraobserver variability, the first observer repeated analysis on 160 and 200 FOV to detect any significant changes in definition. For both the interobserver and intraobserver studies, all simulated vessels were analyzed at the same flow rates to avoid the inclusion of errors that may have been present in some images, but not others.

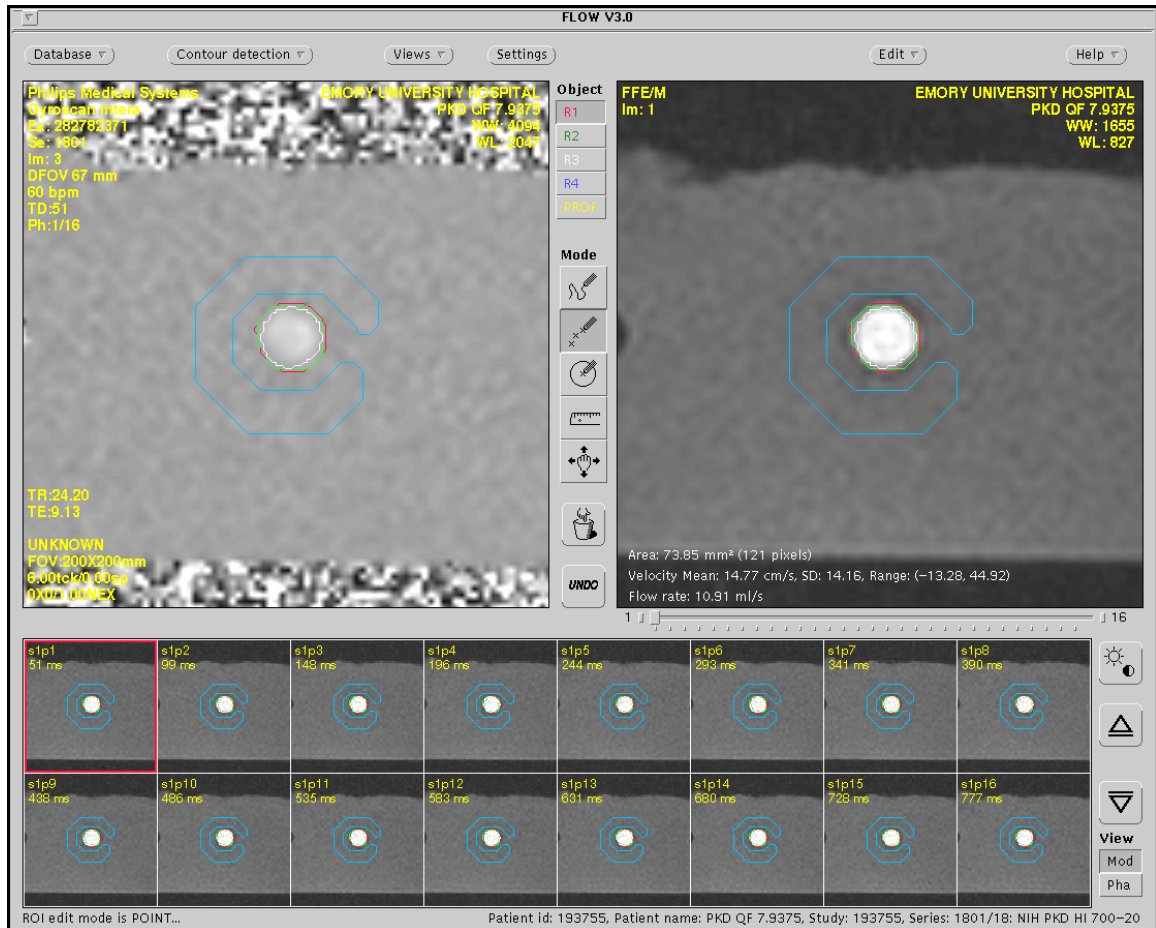


Figure 4-6: Sample screen layout using the FLOW software package. The first region of interest (red) was drawn manually in the modulus image (right), while the second region of interest (green) was drawn in the phase image (left). The third region of interest (white) was created using the automatic contour detection algorithm included in the program. The fourth region of interest (C-shape) was used to correct for static velocity components.

Table 4-3: Experimental flow rates used to assess inter- and intraobserver variability. Data was compiled at these flow rates, which represent a mid-range rate of flow for each simulated vessel, at 160 and 200 mm FOV ($n = 12$).

		Channel Diameter (mm)					
		3.18	4.76	6.35	7.94	9.52	11.11
Flow Rate (ml/min)		377.96	510.04	654.48	691.37	795.88	919.18

Statistical Analysis: Bland and Altman Plots and Coefficient of Variance

In order to assess the resulting data statistically, two statistical methods were used: the Bland and Altman method and the coefficient of variance.

Bland and Altman plots are used to assess the agreement between two measurement techniques and are specifically used when comparing a new method against one that is established [17, 96]. As stated by Bland and Altman, it is often misleading and inappropriate to evaluate clinical results using correlation coefficients or regression analysis [97]. In this experiment, the experimental flow rates provided in Table 4-1 are defined as the established method, while the experimental flow rates calculated from each region of interest (magnitude, phase, automatic) are defined as the new technique. This method plots the difference between the results of the two methods against the average of the two methods, as shown in the example plot in Figure 4-7. The differences may be plotted as a numerical difference, as a percent of the averages, or as a ratio. For the purposes of this experimental study, the plots will be further presented as both a

numerical difference between the two methods and also as a percent of the averages to more accurately portray observed differences.

As shown in Figure 4-7, the graph displays a scatter diagram of the differences plotted against the averages of the two measurements. Dashed lines are drawn at the mean difference and the mean difference (bias) plus or minus two standard deviations of all data being compared. This type of statistical comparison is useful in revealing a number of key issues, including a relationship between the differences and the averages, systemic bias, and also possible outliers. Bland and Altman plots are also useful in assessing the repeatability of a method. This may be accomplished by comparing repeated measurements using one method on a series of subjects. The Bland and Altman method also provides a quantitative bias. If this bias is consistent, it may be adjusted for by subtracting the mean difference from the resultant measurements using the new method being tested.

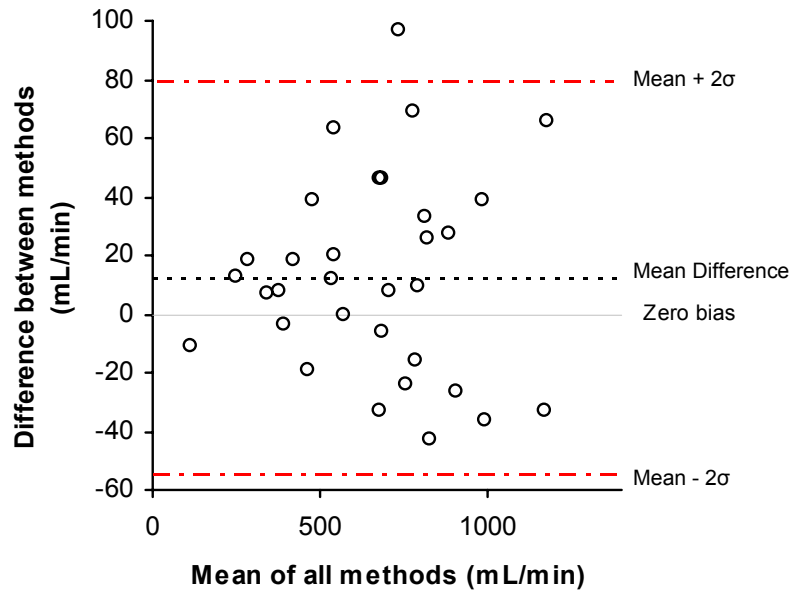


Figure 4-7: Example of a Bland and Altman Plot using the difference between methods. Other variations of this plot may be used, including the presentation of the difference between methods as a percent, which will be further discussed in Chapter V.

A second statistical method was used to evaluate the results from the evaluation of materials and also to reinforce the results presented in the Bland-Altman plots. In the described experiments, the coefficient of variance (COV) was used [98]. The coefficient of variance is calculated as shown in Equation (4-5)

$$COV = \frac{\sigma}{\mu} \times 100\% \quad (4-5)$$

where σ is the standard deviation and μ is the mean of flow data obtained using MRI as compared to true flow. The various coefficients of variance were then compared in order to help determine the best material to use in this validation study. The assurance of steady, laminar flow throughout the model and accurate, reproducible flow measurements in various points along each channel were reinforced using this statistical method. All COV values are also presented in Chapter V for the high-resolution data, in order to further convey the most accurate protocol that may be used for this type of study *in vivo*.

CHAPTER V

RESULTS

The results of the renal phantom validation study are organized into five sections corresponding to the five primary studies performed: (1) a material study exploring the results of MRI experiments using glass, plastic, and PVA; (2) a comparison of high-resolution scans at 160, 200 and 350 mm FOV; (3) the variation in MRI experimental results using low-resolution (96 phase encodings) versus high-resolution (192 phase encodings) protocol; (4) a multiple-site study comparing image data at three points along the simulated vessel; and (5) an experiment studying the effects of velocity encoding in three directions.

Based upon statistical data, including the Bland-Altman method and the coefficient of variance (COV), it is shown that PVA provides more accurate flow values, as opposed to other materials, specifically plastic and glass. Using a high-resolution gradient-echo technique with 192 phase encodings, experiments at 160 and 200 mm FOV are shown to be superior to those at 350 mm FOV. The use of high-resolution scans also improved results from previous tests using 96 phase encodings (low-resolution). The multiple-site study resulted in similar data along the length of each channel, while velocity profiles illustrated that the flow was steady. The multiple-site study also confirmed the overall reproducibility of results. Velocity encoding in three directions did

not significantly improve data. The results from each of these experimental studies will be further discussed in this chapter.

Material Evaluation Using PVA, Plastic, and Glass

The aim of this study was to investigate the MR velocity data resulting from the use of PVA, plastic, and glass when used as vessel wall materials in MRI validation. Figure 5-1 displays the experimental flow rate results of the PVA and plastic experiments taken simultaneously at 200 mm FOV with no background correction applied as compared to true flow obtained using the weight determination method. Glass data was acquired using the same parameters, but in a different set of experiments [93], and is therefore not compared in this specific figure. The statistical test used for this specific experimental evaluation was the average COV (Equation 4-5); Figure 5-2 displays these results for each material.

By comparing the flow data acquired through the plastic tubing and comparing it to the true flow identity line in Figure 5-1, it is shown that the plastic data generally deviates more from the true flow rate values as compared to the PVA data, although some points representing plastic flow are more accurate than others. Figure 5-2 indicates the same results, as the average COV of PVA is consistently less than that of both plastic and glass. Plastic data deviates the most at a channel diameter of 4.76 mm, followed by 3.18 mm, suggesting increased difficulty in accurately defining the vessel wall at smaller diameters.

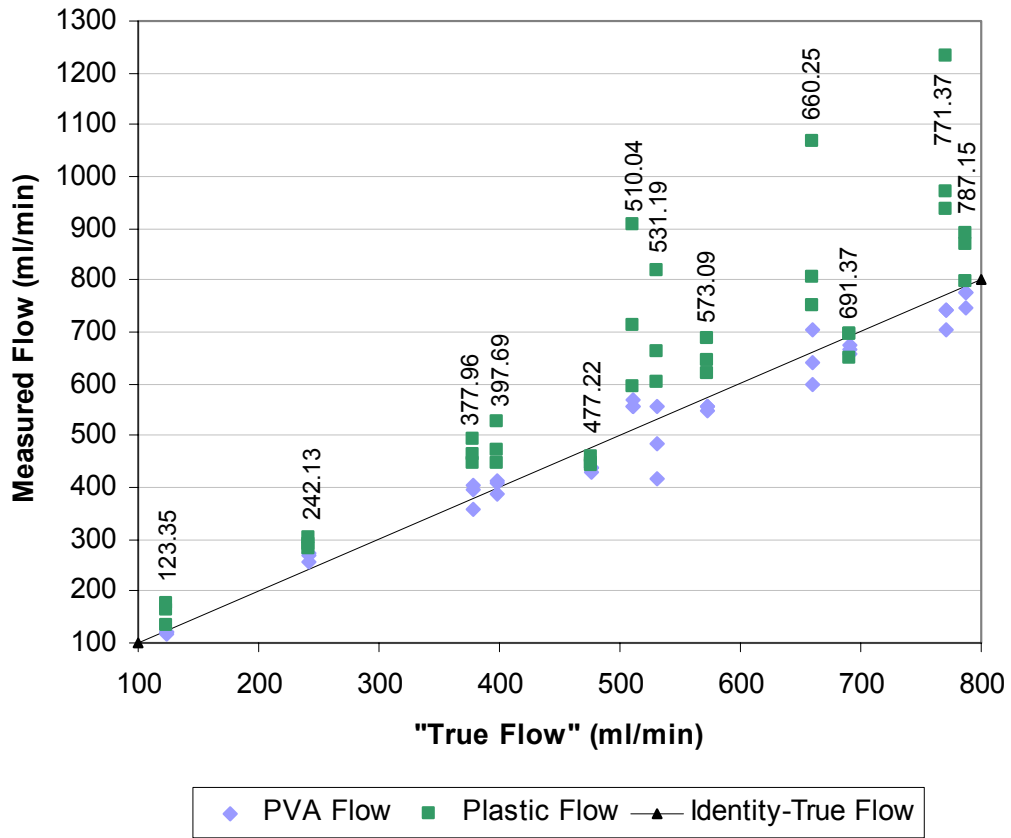


Figure 5-1: Flow rate data obtained from PVA and plastic at the 200 mm FOV with no background correction applied. These results were obtained from the following channels: 3.18, 4.76, and 7.94 mm. As shown, the plastic data deviates more from the true flow rate values than the PVA data.

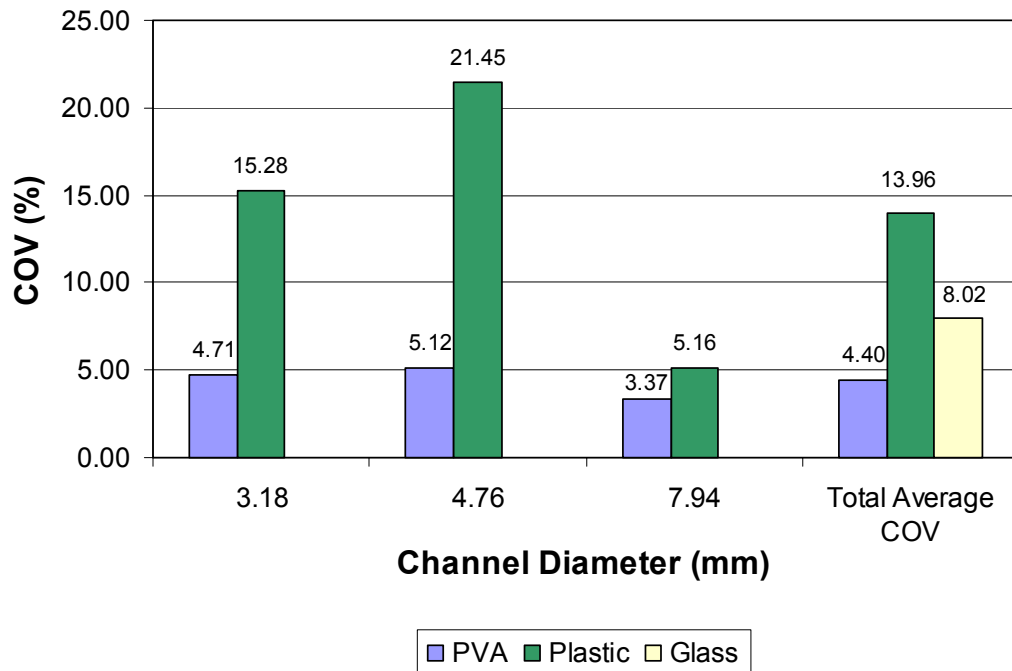


Figure 5-2: Average COV results calculated from the image data acquired using PVA, plastic, and glass at the 200 mm FOV. The average COV of PVA is consistently less than that of the two supplementary materials studied.

As shown in Figures 5-1 and 5-2, PVA consistently provides more accurate (Figure 5-1) and more precise (Figure 5-2) velocity images as compared to plastic and glass. The average difference between each individual measurement was also calculated for each material, being equivalent to 4.17%, 10.09%, and 1.02% for PVA, plastic, and glass, respectively.

Comparison of High-Resolution Scans: 160, 200 and 350 mm FOV

This section will present the results obtained from the high-resolution scans (192 phase encodings) at 160, 200, and 350 mm FOV. For each flow rate tested, six sets of data are presented, based upon each region of interest as defined in Chapter IV, with and without background correction. In the case of the high-resolution scans, four scans sets were unreadable at all fields of view. The highest flow rates for the simulated channels measuring 3.18 and 4.76 mm (764.94 and 864.22 ml/min, respectively) provided extremely poor results due to velocity aliasing, which were subsequently not used in the analysis. Wraparound artifact, including velocity aliasing, will be further discussed in the next chapter. For the two highest flow rates at 7.94 mm (896.50 and 979.08 ml/min), the FLOW program could not read the velocity information in the images. This resulted in thirty-two data sets available for statistical analysis ($n = 32$) for each region of interest defined for the 160 and 200 mm FOV. It is also important to note that the automatic contour detection algorithm (ROI 3) was unable to determine the vessel boundary for the second-highest flow rate for the 3.18 mm channel (531.19 ml/min) at the 350 mm FOV

($n = 31$ for the ROI 3 data sets). These issues will also be further discussed in Chapter VI: Discussion. For each flow rate, all six points (ROI 1, ROI 2, ROI 3, BG ROI 1, BG ROI 2, AND BG ROI 3) are shown, with the exception of the second-highest rate obtained using the 3.18 mm channel. In these figures, many of the resulting MRI flow rates are exceedingly similar in value, making it somewhat difficult to distinguish all six points in certain cases. Figures 5-3 through 5-5 display the experimental flow rates calculated using MRI techniques as compared to true flow rates found using the weight determination method. In each of these figures, the magnitude image contour is defined as ROI 1, the phase image contour as ROI 2, and the automatic contour as ROI 3. “BG” denotes that background subtraction has been applied to the data series.

When comparing Figures 5-3 and 5-4, it is difficult to notice a significant difference in data between the 160 and 200 mm FOV; both sets of data appear relatively accurate as compared to true flow rate values. However, it is noticeable how the flow rate data generally becomes more scattered and less comparable to true flow when the 350 mm FOV is used (Figure 5-5). In order to accurately analyze this data, Bland-Altman plots were used to assess the differences statistically. The correlation coefficients for each ROI when used at each FOV are provided in Table 5-1. All correlation coefficients were above 0.975 at the 160 and 200 mm FOV.

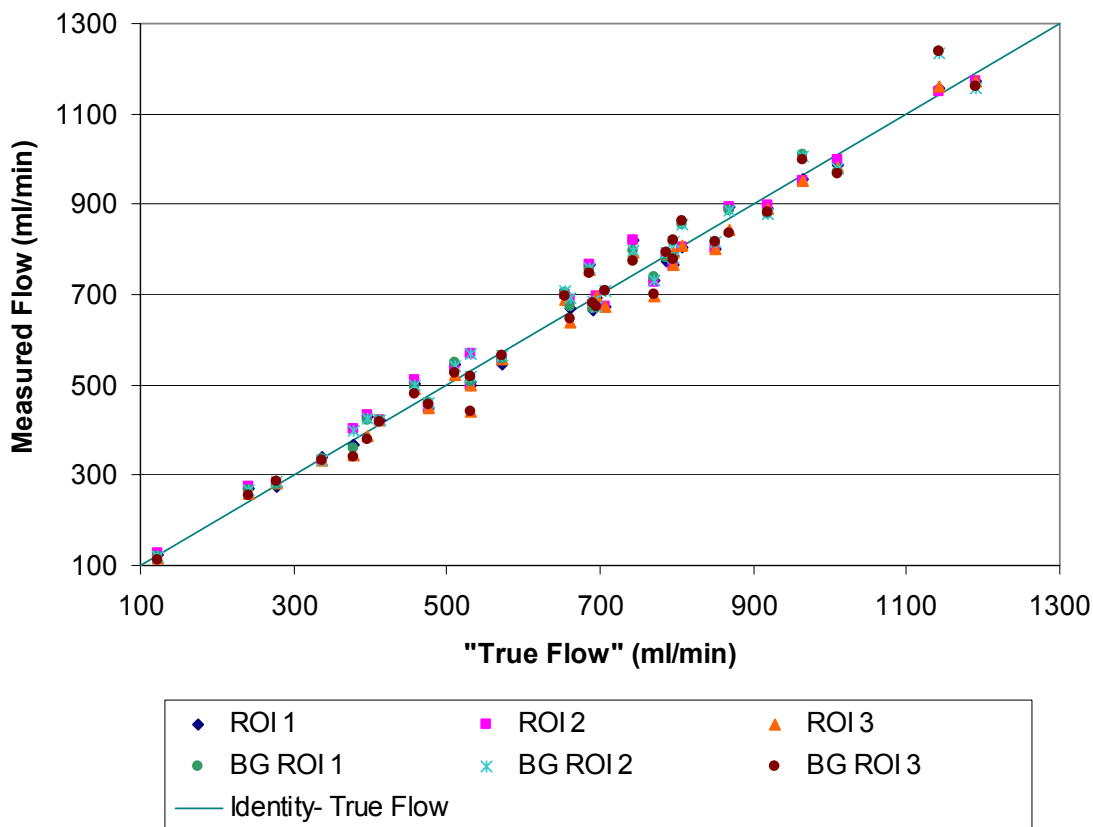


Figure 5-3: Flow rate data obtained from high-resolution experiments at the 160 mm FOV as compared to the true flow rates calculated using the weight determination method. All flow rates presented here span the entire range of simulated vessels ($n = 32$). The terms in the legend correspond to the following: magnitude image contour (ROI 1); phase image contour (ROI 2); and automatic contour (ROI 3). “BG” denotes that background subtraction has been applied to the data series.

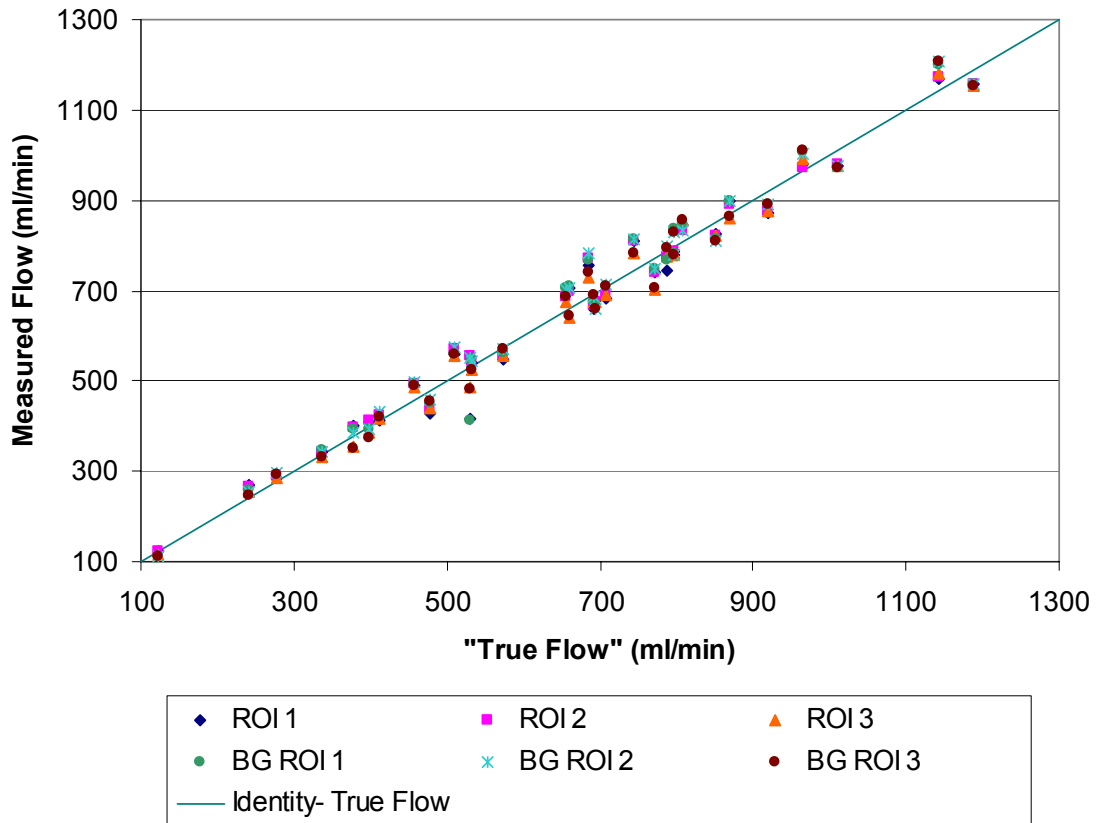


Figure 5-4: Flow rate data obtained from high-resolution experiments at the 200 mm FOV as compared to the true flow rates calculated using the weight determination method. All flow rates presented here span the entire range of simulated vessels ($n = 32$). The terms in the legend correspond to the following: magnitude image contour (ROI 1); phase image contour (ROI 2); and automatic contour (ROI 3). “BG” denotes that background subtraction has been applied to the data series.

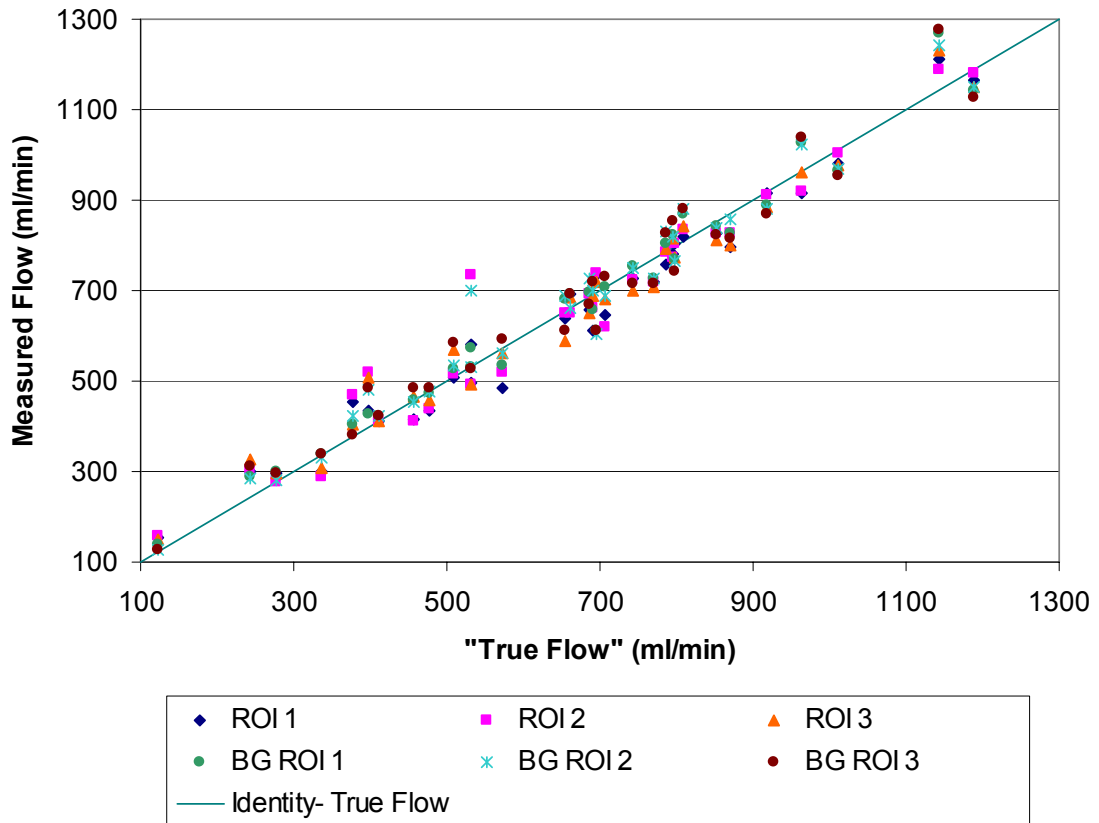


Figure 5-5: Flow rate data obtained from high-resolution experiments at the 350 mm FOV as compared to the true flow rates calculated using the weight determination method. All flow rates presented here span the entire range of simulated vessels ($n = 32$), except for ROI 3 and BG ROI 3, where $n = 31$. The terms in the legend correspond to the following: magnitude image contour (ROI 1); phase image contour (ROI 2); and automatic contour (ROI 3). “BG” denotes that background subtraction has been applied to the data series.

Table 5-1: Correlation coefficients calculated for each ROI based upon the data presented in Figures 5-3 through 5-5.

	FOV		
	160 mm	200 mm	350 mm
ROI 1	0.9842	0.9770	0.9716
ROI 2	0.9840	0.9849	0.9500
ROI 3	0.9844	0.9869	0.8540
BG ROI 1	0.9828	0.9754	0.9747
BG ROI 2	0.9830	0.9825	0.9634
BG ROI 3	0.9797	0.9836	0.8477

Using the Bland-Altman statistical technique, plots were prepared for each region of interest analyzed using each particular field of view. Each plot is presented in Appendix A (Figures A-1 through A-18). A summary of the information extracted using the Bland-Altman method is provided in Table 5-2. Using this information, the biases and standard deviations (SD) were compiled for each ROI, and are shown in Figures 5-6 through 5-11.

When using the magnitude border, or ROI 1, the best results were obtained when using the 160 mm FOV, while significant deviation from true flow existed when using the 350 mm FOV (Figure 5-6). For the phase border (ROI 2), the 200 mm FOV provided the most accurate results, while the 350 mm FOV continued to result in significant deviation (Figure 5-7). The same observations were made for the automatic border (ROI 3), shown in Figure 5-8. When applying background correction, the 160 mm FOV continued to provide the most accurate results for ROI 1; however, the background subtraction improved the data at the 350 mm FOV (Figure 5-9). In terms of applying

background correction to ROI 2 and ROI 3, no significant changes were observed, as the 160 and 200 mm FOV provided similar results and the 350 mm FOV provided the poorest results (Figures 5-10 and 5-11). Overall, throughout all cases, it was extremely difficult to make an exact determination of which field of view was most accurate: the 160 or 200 mm FOV. Thus, a Bland-Altman test was performed comparing the combined data sets of ROI 1 (magnitude border) and ROI 2 (phase border) at the 160 and 200 mm FOV to true flow values. These plots are presented in Figures 5-12 and 5-13.

Table 5-2: Various quantitative results extracted from the Bland and Altman plots shown in Appendix A (Figures A-1 through A-18). The bias is calculated by finding the mean difference between methods, and may be used to adjust results obtained using a new clinical method based on a more established one. Based on the assumption of a normal distribution, the majority of data points (95%) will lie within two standard deviations (SD) of the mean. The upper and lower percent differences display the difference between methods as a percent of the averages. The terms in the table correspond to the following: magnitude image contour (ROI 1); phase image contour (ROI 2); and automatic contour (ROI 3). “BG” denotes that background subtraction has been applied to the data series.

	Bias (mL/min)	- 2 SD (mL/min)	+ 2 SD (mL/min)	Lower % Difference	Upper % Difference
160 FOV					
ROI 1	-0.894	-64.134	62.346	-6.39	11.69
ROI 2	4.459	-59.845	68.763	-6.28	11.88
ROI 3	-10.413	-73.185	52.359	-9.67	7.19
BG ROI 1	6.554	-60.181	73.290	-4.78	10.25
BG ROI 2	11.554	-54.146	77.254	-5.11	9.98
BG ROI 3	-3.508	-77.214	70.199	-10.61	8.37
200 FOV					
ROI 1	-0.166	-76.383	76.051	-10.55	11.36
ROI 2	6.262	-55.923	68.447	-8.41	11.05
ROI 3	-5.254	-62.811	52.304	-9.03	8.60
BG ROI 1	7.011	-72.891	86.912	-9.31	11.44
BG ROI 2	12.817	-53.905	79.538	-9.41	13.14
BG ROI 3	0.005	-65.320	65.329	-11.23	9.00
350 FOV					
ROI 1	-10.098	-94.993	74.798	-16.45	22.74
ROI 2	1.356	-110.958	113.669	-15.63	23.50
ROI 3	-1.617	-90.610	87.376	-10.79	29.25
BG ROI 1	5.434	-74.543	85.411	-6.89	17.48
BG ROI 2	13.453	-82.833	109.739	-5.88	27.24
BG ROI 3	7.875	-95.184	110.935	-12.68	24.50

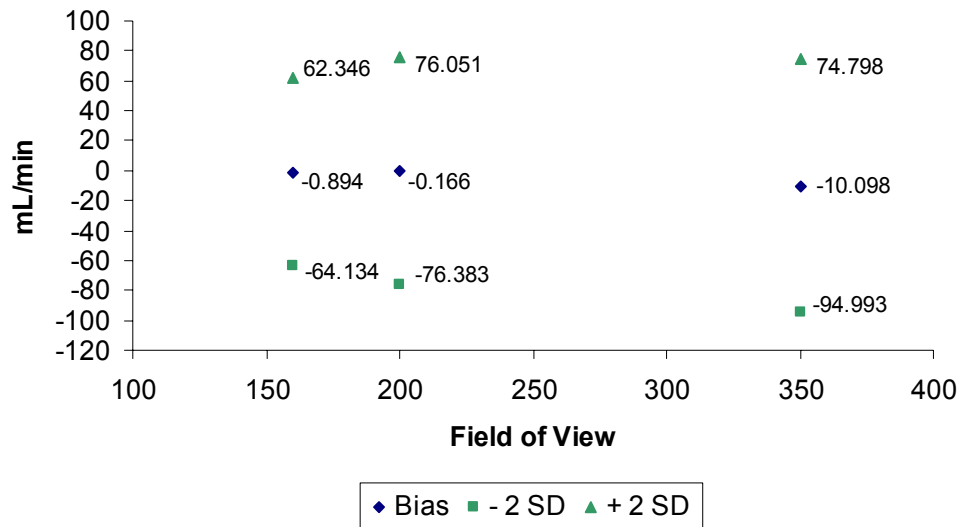


Figure 5-6: Graphical comparison of data analysis using the Bland-Altman method. The data presented here was acquired using the magnitude border (ROI 1) at 160, 200, and 350 mm FOV and corresponds to the data presented in Table 5-2. The 160 mm FOV proved to be the most accurate parameter in this case, while the 350 mm FOV was the least accurate.

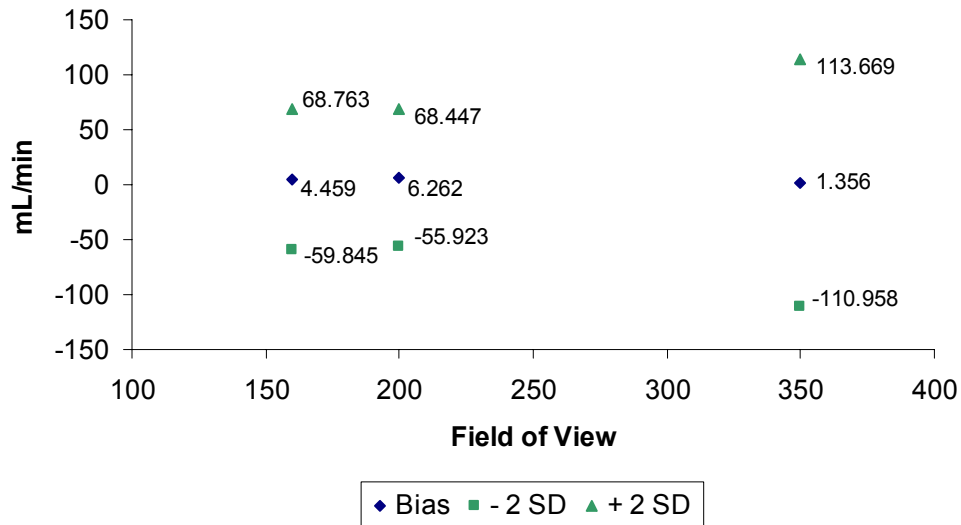


Figure 5-7: Graphical comparison of data analysis using the Bland-Altman method. The data presented here was acquired using the phase border (ROI 2) at 160, 200, and 350 mm FOV and corresponds to the data presented in Table 5-2. The 200 mm FOV proved to be the most accurate parameter in this case, while the 350 mm FOV was the least accurate.

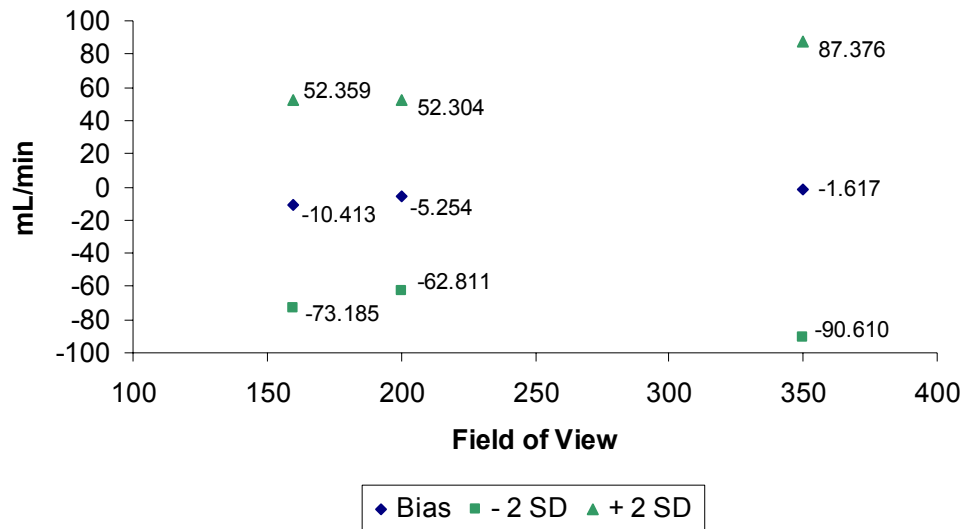


Figure 5-8: Graphical comparison of data analysis using the Bland-Altman method. The data presented here was acquired using the automatic border (ROI 3) at 160, 200, and 350 mm FOV and corresponds to the data presented in Table 5-2. The 200 mm FOV proved to be the most accurate parameter in this case, while the 350 mm FOV was once again the least accurate.

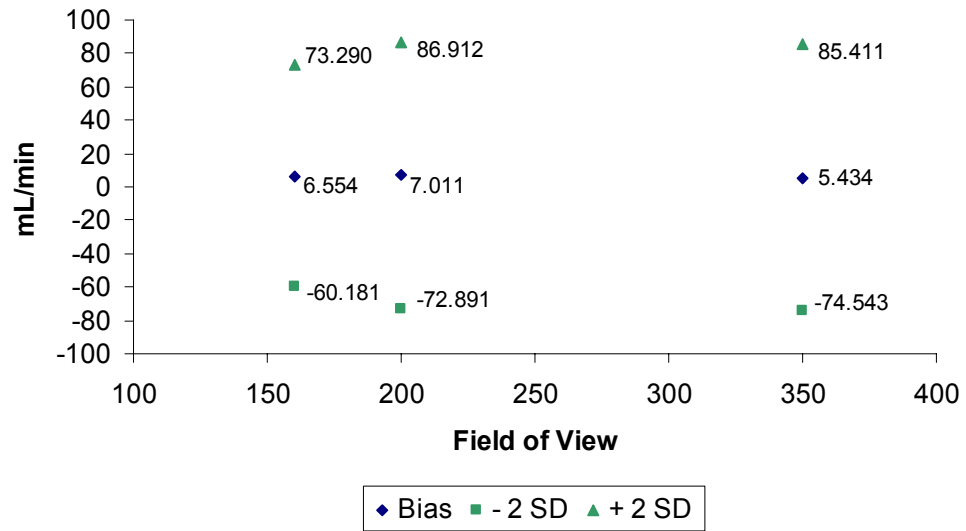


Figure 5-9: Graphical comparison of data analysis using the Bland-Altman method. The data presented here was acquired using the magnitude border with background correction (BG ROI 1) at 160, 200, and 350 mm FOV and corresponds to the data presented in Table 5-2. The 160 mm FOV proved to be the most accurate parameter in this case, while the 200 mm FOV was the least accurate.

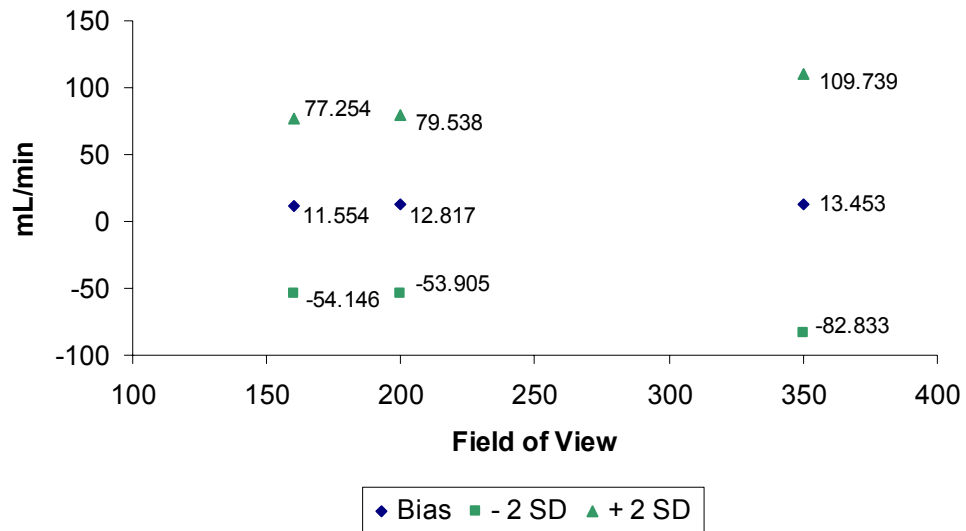


Figure 5-10: Graphical comparison of data analysis using the Bland-Altman method. The data presented here was acquired using the phase border with background correction (BG ROI 2) at 160, 200, and 350 mm FOV and corresponds to the data presented in Table 5-2. In this case, the 160 and 200 mm FOV were the most accurate parameters.

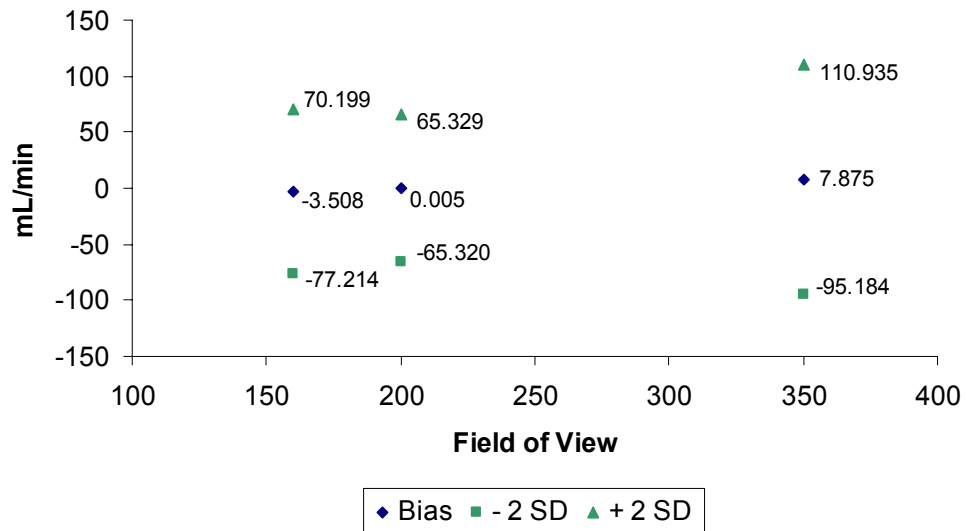


Figure 5-11: Graphical comparison of data analysis using the Bland-Altman method. The data presented here was acquired using the automatic border with background correction (BG ROI 1) at 160, 200, and 350 mm FOV and corresponds to the data presented in Table 5-2. The 200 mm FOV proved to be the most accurate parameter in this case, while the 350 mm FOV was the least accurate.

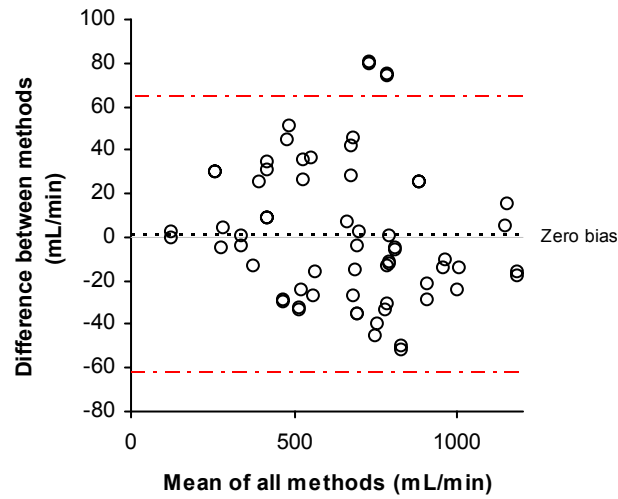


Figure 5-12: Bland and Altman plot displaying the difference between the true flow values and the experimental MRI data ($n = 64$). This plot corresponds to combined data sets of ROI 1 and ROI 2 at the 160 mm FOV.

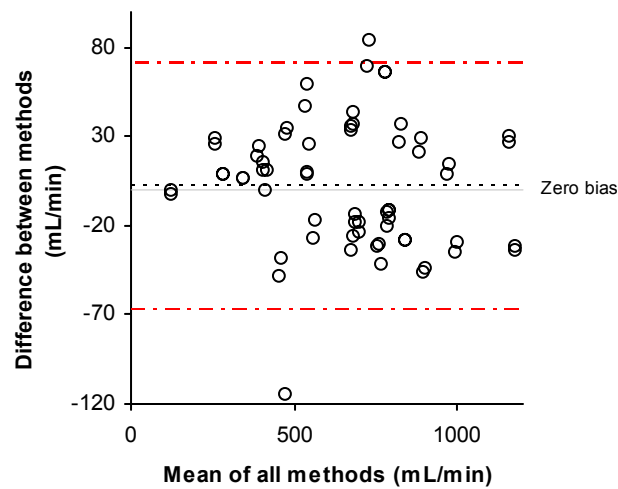


Figure 5-13: Bland and Altman plot displaying the difference between the true flow values and the experimental MRI data ($n = 64$). This plot corresponds to combined data sets of ROI 1 and ROI 2 at the 200 mm FOV.

Based upon the statistical results presented in Table 5-2 and Figures 5-6 through 5-11, it is apparent that using the 350 mm FOV results in data characterized by significantly more deviation than those resulting from the use of the 160 or 200 mm FOV. It is also shown in these results that the 160 and 200 mm FOV are comparable in terms of the data they provide. Significant differences in MRI flow rates do not result from the use of these two different protocols. Quantitatively, as shown in Figures 5-12 and 5-13, the biases for the 160 and 200 mm FOV are 1.782 and 3.048 ml/min, respectively. The 95% limits of agreement were calculated to range from -61.704 to 65.269 ml/min for the 160 mm FOV, while the 200 mm FOV values ranged from -66.245 to 72.341 ml/min. These statistics shown that a significant difference is not observed when using the 200 mm FOV, as opposed to the 160 mm FOV. In order to further analyze data sets, the average COV was calculated for each field of view and each contour at the 160 and 200 mm FOV. These results are presented in Figures 5-14 and 5-15.

In Figures 5-14 and 5-15, it is shown that background subtraction, correcting for DC phase errors, has no significant positive net effect on the velocity-encoded data. For all average COV values at the 160 and 200 mm FOV, only background correcting the phase contour at the 160 mm FOV results in the MRI data being closer in value to the true flow rates. In terms of reducing the amount of bias, using background subtraction only improved results for ROI 3 (the automatic border) for 160 and 200 mm FOV (Table 5-2).

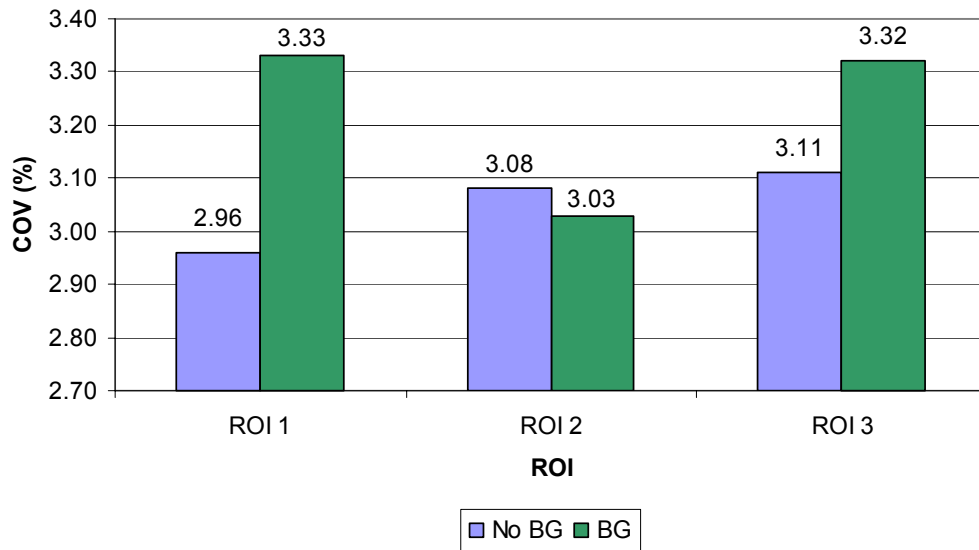


Figure 5-14: Average COV results calculated from the image data acquired using the 160 mm FOV. Background correction (BG) does not improve the results and even has a significant negative effect on ROI 1 and ROI 3.

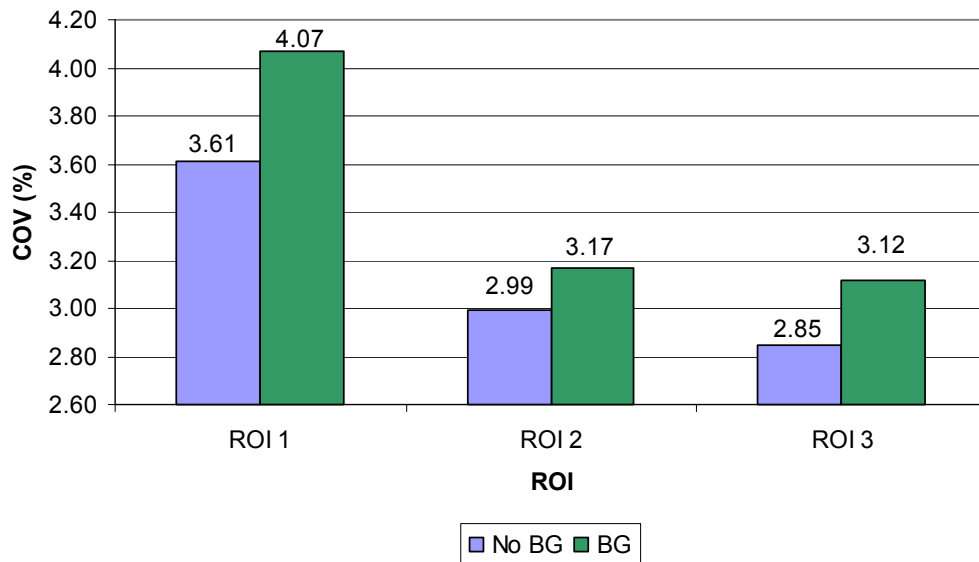


Figure 5-15: Average COV results calculated from the image data acquired using the 200 mm FOV. Background correction (BG) has no positive effect on this data, as all ROIs are negatively affected and vary more from true flow.

Because manual definition was required for border determination in the magnitude (ROI 1) and phase (ROI 2) maps, a potential source of data variability existed. For the six flow rates examined in the inter- and intraobserver studies (Table 4-3), data was processed independently by two investigators and compared. The Bland-Altman statistical method was used to analyze these data, and excellent agreement was found between the two observers, and also in the intraobserver study. Using two observers, which were blinded, the bias was found to be -0.692 ml/min and -1.567 with the 95% limits of agreement ranging from -21.181 ml/min to 19.798 ml/min and -17.274 ml/min to 14.141 ml/min for the 160 and 200 mm FOV, respectively ($n = 12$) (Figure A-19 and A-20). This corresponds to percent differences ranging from -3.193% to 2.571% for the 160 mm FOV and -2.248% to 2.287% for the 200 mm FOV. For the intraobserver study ($n = 12$) the bias resulted in -4.621 ml/min with the 95% limits of agreement ranging from -17.249 to 8.008 ml/min for the 160 mm FOV (Figure A-21). For the 200 mm FOV, the bias was calculated to be -0.903 ml/min with the 95% limits of agreement ranging from -14.705 to 12.899 ml/min (Figure A-22).

Low-Resolution Scan Comparison: 160, 200 and 350 mm FOV

In order to demonstrate if an increase in the number of phase encodings makes a significant difference in resulting data, low-resolution scans (96 phase encodings) were also performed during this validation study. This subsection will present the results obtained from the low-resolution scans at the 160, 200, and 350 mm FOV. Because

background correction was shown to have no significant positive effect on the flow data, only the data that has not been background-corrected will be presented for this experiment. Again, the data is obtained from each region of interest defined in the images as described in Chapter IV. The same four scans that provided poor images in the high-resolution data also presented issues with the low-resolution data, indicating that true flow values may have been the cause of error. This subsequently resulted in thirty-two data sets available for statistical analysis ($n = 32$) for each region of interest. A summary of the information extracted using the Bland-Altman method to analyze the low-resolution data is provided in Table 5-3, while corresponding Bland-Altman plots are provided in Appendix A (Figures A-23 through A-31). A graphical comparison of the low-resolution data and high-resolution data for each field of view is provided in Figure 5-16 (ROI 1), 5-17 (ROI 2), and 5-18 (ROI 3). For the magnitude and phase borders, variability in the low-resolution data increased as the field of view increased (Figures 5-16 and 5-17). When using the automatic border, low-resolution data was more comparable to high-resolution data at the 160 and 200 mm FOV, while increased deviation was observed at the 350 mm FOV.

Table 5-3: Various quantitative results extracted from the Bland and Altman plots shown in Figures 5-26 through 5-35 using low-resolution protocol (96 phase encodings). A brief description of each of these statistical parameters is provided with Table 5-2. When comparing the values in this table with those in Table 5-2, it is apparent that high-resolution protocol (192 phase encodings) provides significantly more accurate results, as further shown in the following figures.

	Bias (mL/min)	- 2 SD (mL/min)	+ 2 SD (mL/min)	Lower % Difference	Upper % Difference
160 FOV					
ROI 1	11.804	-83.936	107.543	-9.42	34.73
ROI 2	33.097	-77.364	143.558	-11.02	35.52
ROI 3	-27.310	-113.033	58.413	-20.13	15.21
200 FOV					
ROI 1	32.806	-97.695	163.306	-10.94	47.48
ROI 2	57.307	-131.192	245.267	-9.68	61.43
ROI 3	-39.897	-141.624	61.831	-19.22	26.30
350 FOV					
ROI 1	173.082	-40.846	387.010	7.12	80.23
ROI 2	158.894	-120.122	437.910	-9.89	85.13
ROI 3	4.216	-398.707	407.139	-71.54	73.52

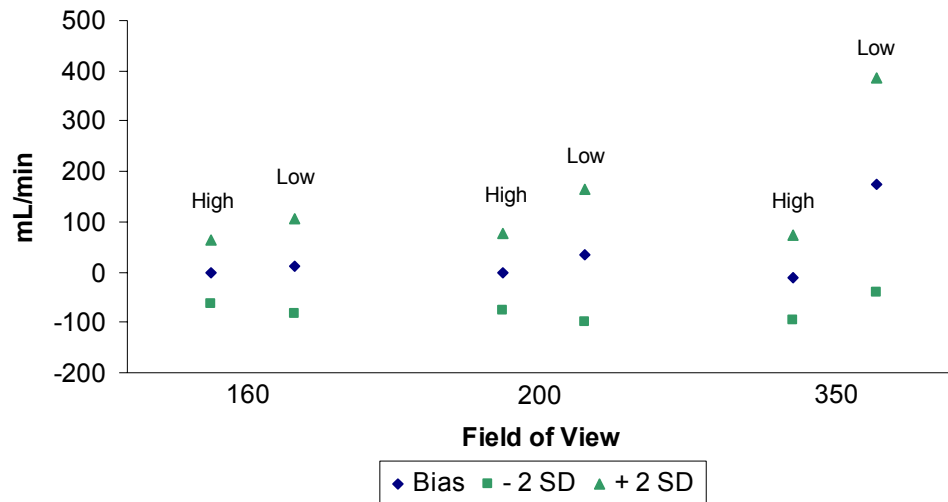


Figure 5-16: Graphical comparison of high-resolution (192 phase encodings) and low-resolution (96 phase encodings) protocol obtained using the Bland-Altman method. The data presented here was acquired using the magnitude border (ROI 1) at the 160, 200, and 350 mm FOV and corresponds to the data presented in Table 5-3. The amount of variability between low- and high-resolution increased with increasing field of view.

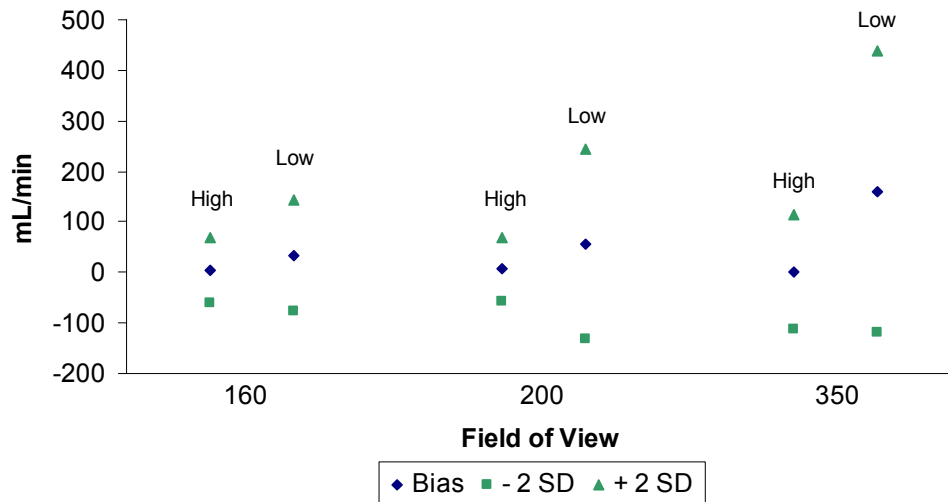


Figure 5-17: Graphical comparison of high-resolution (192 phase encodings) and low-resolution (96 phase encodings) protocol obtained using the Bland-Altman method. The data presented here was acquired using the phase border (ROI 2) at the 160, 200, and 350 mm FOV and corresponds to the data presented in Table 5-3. The amount of variability between low- and high-resolution again increased with increasing field of view.

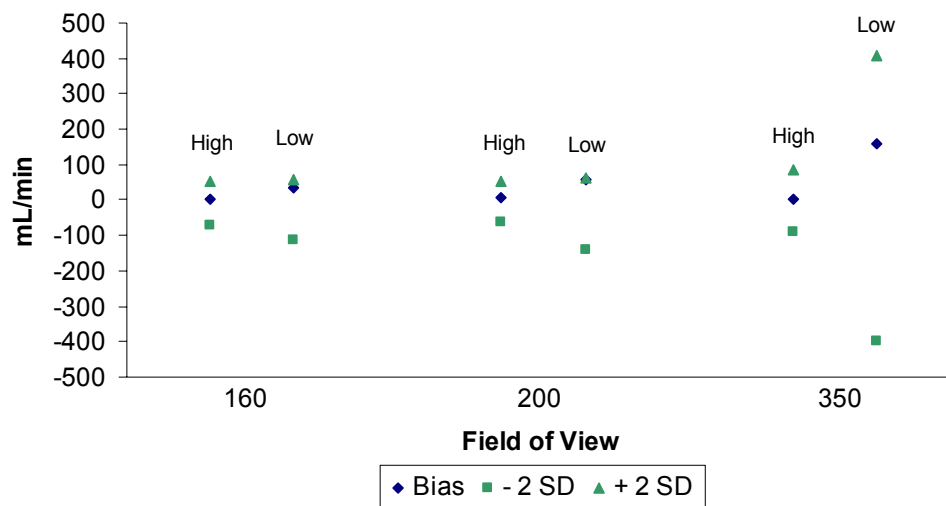


Figure 5-18: Graphical comparison of high-resolution (192 phase encodings) and low-resolution (96 phase encodings) protocol obtained using the Bland-Altman method. The data presented here was acquired using the automatic border (ROI 3) at 160, 200, and 350 mm FOV and corresponds to the data presented in Table 5-3. In this case, the low-resolution data is comparable at 160 and 200 mm FOV, while increased variability is observed at 350 mm FOV.

As shown in Table 5-3 and Figures A-23 through A-31, low-resolution protocol using 96 phase encodings produces data with a considerable amount of bias and variability when compared to true flow values. This data suggests that high-resolution protocol using 192 phase encodings is an improved technique providing more accurate data, shown graphically in Figures 5-16 through 5-18.

Figures 5-19 and 5-20 display the Bland-Altman plots using the percent difference method. These figures more accurately portray the significant differences observed using a lower resolution protocol, and do not show the 95% limits of agreement as the data points are shown as a percent of the corresponding averages. These figures emphasize the differences observed between low-resolution MRI data and true flow based upon each flow rate. This characteristic resulted in some interesting observations. When using 96 phase encodings, velocity-encoded data is consistently less accurate at lower flow rates (< 500 ml/min). This was consistent across all low-resolution data sets.

For the low-resolution data, the absolute bias values were consistently greater than those observed using high-resolution protocol (Figures 5-16 through 5-18). The automatic detection algorithm also underestimated the contour of the simulated vessel throughout these experiments. Overall, MRI data varied significantly more using the parameters set forth in the low-resolution protocol.

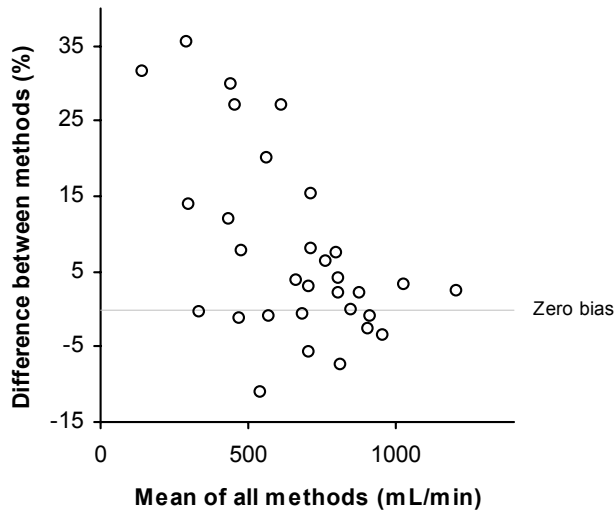


Figure 5-19: Bland and Altman plot displaying the difference between true flow values and MRI data as a percentage using low-resolution protocol (96 phase encodings). This figure specifically shows the extreme deviation from true flow, especially at lower flow rates (< 500 ml/min). Data presented here is from the phase image contour obtained using 160 mm FOV.

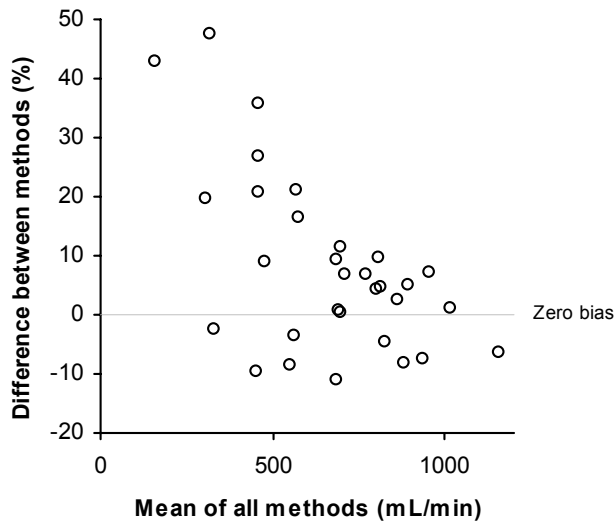


Figure 5-20: Bland and Altman plot displaying the difference between true flow values and MRI data as a percentage using low-resolution protocol (96 phase encodings). This figure also shows the extreme deviation from true flow, specifically at lower flow rates (< 500 ml/min). Data presented here is from the magnitude image contour obtained using 200 mm FOV.

Multiple-Site Study

In order to ensure that the flow characteristics during the validation study were laminar and fully-developed, visually-defined perpendicular planes were imaged at three different points along each vessel for each scan set. The first scan plane is centered along the phantom, and this data has been previously presented as the 200 mm FOV high-resolution data. The second and third scan planes were used to evaluate flow along the length of each simulated vessel at the 200 mm FOV. A schematic of the scan planes and their orientation is provided in Figure 5-21. These scans were performed at the 200 mm FOV using 192 phase encodings (high-resolution). The Bland-Altman test was used to test the statistical accuracy of this method for the magnitude and phase borders by combining the data acquired at sites 2 and 3 and comparing it against data from site 1 ($n = 50$ for each). Agreement was found to be close over the flow range tested for both regions of interest observed, as shown in Figures 5-22 and 5-23. The bias calculated using the data from the magnitude border (ROI 1) was found to equal 4.784 ml/min, while the 95% limits of agreement equaled -27.288 to 36.856 ml/min (Figure 5-22). For the phase border (ROI 2), the bias was equivalent to 0.372 ml/min, while the 95% limits of agreement were found to equal -18.959 to 19.702 ml/min (Figure 5-23). The average COV was also calculated for these observations and was recorded as 1.04% and 1.93% for ROI 1 and ROI 2, respectively. This data also exhibits the overall reproducibility of the method. In addition to the inter- and intraobserver studies, the multiple-site test shows that it is possible to obtain both accurate and reproducible flow data. The biases are both within 5 ml, and the COV values are both within 2%.

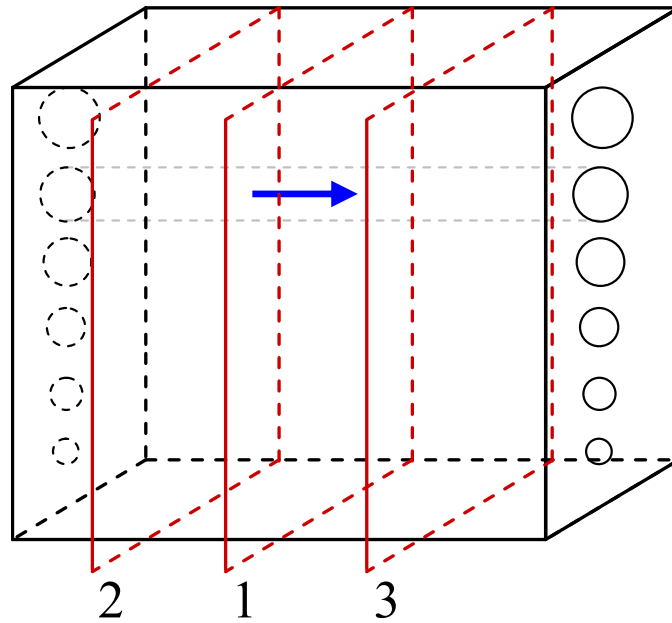


Figure 5-21: Schematic showing visually-defined perpendicular planes used to capture velocity-encoded phase images in this phantom validation study. The first scan plane is centered along the phantom, and this data is presented as the 200 mm FOV high-resolution data. The second and third scan planes were used to evaluate flow along the length of each simulated vessel at the 200 mm FOV.

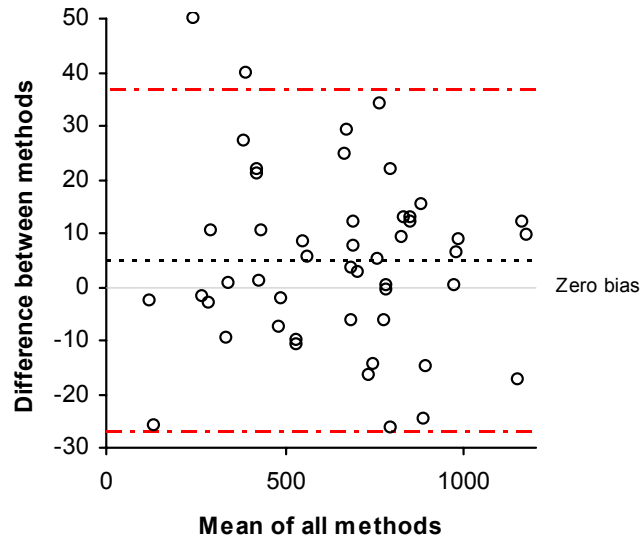


Figure 5-22: Bland and Altman plot displaying the difference between sites 2 and 3 as compared to site 1 (Figure 5-21). This plot corresponds to the manual contour drawn in the magnitude image (ROI 1) at the 200 mm FOV.

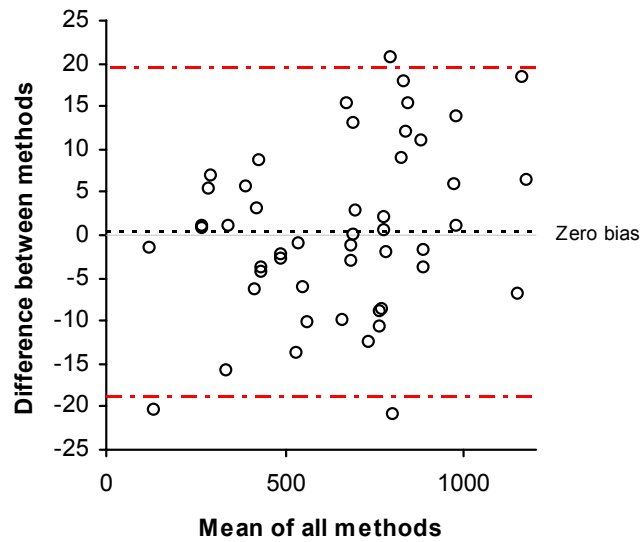


Figure 5-23: Bland and Altman plot displaying the difference between sites 2 and 3 as compared to site 1 (Figure 5-21). This plot corresponds to the manual contour drawn in the phase image (ROI 2) at the 200 mm FOV.

The flow characteristics resulting from this experiment were also analyzed using velocity profiles generated by the FLOW program for each separate scan over the cardiac cycle (16 phases for high-resolution data). Plots were observed as the analysis was completed for each data set to check for irregularity in flow characteristics. Across the cardiac cycle, all flow rates were within 2 ml/s of each other, most having a difference of less than 0.5 ml/s. The data presented in this section suggest that steady, laminar flow was present throughout the experimental study, which further agrees with the Reynolds number calculations performed at each flow rate for each simulated vessel using Equation (4-2). The Reynolds numbers are provided in Table 5-4, with each corresponding flow rate listed directly below the respective Reynolds number.

Although a precise range cannot be quantified for whether flow is classified as laminar or turbulent, it is appropriate for general purposes to describe flow in a pipe, or round tube, as laminar if the Reynolds number is less than 2100 [99]. If the Reynolds number is greater than 4000, turbulent flow exists, with the region in between these two values defined as transitional. In the transitional state, flow may switch between laminar and turbulent flow. However, since the greatest Reynolds number in this validation study is 1460.75, it is shown that only laminar flow was present in these experiments throughout each channel for all flow rates observed.

Table 5-4: Reynolds numbers resulting from experimental flow rates measured using the weight determination method, which are shown in parentheses below each corresponding Reynolds number. The Reynolds numbers listed below were calculated using Equation (4-2) and are all within the laminar range, as defined by Munson et al. [99].

		Channel Diameter (mm)					
		3.18	4.76	6.35	7.94	9.52	11.11
Reynolds Number (Re)		235.55 (123.35)	354.03 (278.09)	321.72 (336.95)	364.52 (477.22)	338.68 (532.07)	378.85 (694.37)
		462.38 (242.13)	524.15 (411.72)	437.24 (457.93)	437.75 (573.09)	449.95 (706.87)	434.65 (796.64)
		721.76 (377.96)	649.32 (510.04)	624.90 (654.48)	528.10 (691.37)	506.61 (795.88)	464.62 (851.56)
(Flow Rate) (mL/min)		759.44 (397.69)	840.55 (660.25)	655.06 (686.06)	601.26 (787.15)	514.46 (808.22)	501.51 (919.18)
		1014.37 (531.19)	982.02 (771.37)	710.26 (743.88)	684.79 (896.5)	613.88 (964.4)	551.30 (1010.44)
		1460.75 (764.94)	1100.22 (864.22)	830.60 (869.91)	747.87 (979.08)	727.02 (1142.15)	648.95 (1189.41)

Velocity Encoding in Three Directions

For this experiment, velocity was encoded in all three orthogonal planes (RL, AP, FH) to detect any deviations in flow and to observe if this technique provided more accurate results. These scans were performed using a field of view of 240 mm x 240 mm (240 mm). Each scan was then reconstructed and individually analyzed using the same method as previously described. A total of twenty-four reconstructed image sequences were readable and subsequently analyzed using this protocol. Table 5-5 provides a summary of these results using the Bland and Altman method.

When comparing these results to those in Table 5-2, specifically at the 200 mm FOV, the amount of bias is comparable; however, the 95% limits of agreement are greater in both directions (± 2 SD) all regions of interest defined. This is shown graphically in Figure 5-24. It is interesting to note that the automatic detection algorithm (ROI 3) provided the best results for this technique, although it was not significantly better than the manually-defined magnitude and phase borders. The bias was only improved by approximately 1 ml/min.

Table 5-5: Quantitative summary resulting from experiment with velocity encoded in three directions. A field of view of 240 mm was used in this protocol. The magnitude (ROI 1), phase (ROI 2), and automatic (ROI 3) borders were analyzed using this technique. The automatic detection algorithm most accurately analyzed the velocity data encoded in the phase-velocity images for this protocol, but not by a significant amount.

	Bias (mL/min)	- 2 SD (mL/min)	+ 2 SD (mL/min)	Lower % Difference	Upper % Difference
240 FOV					
ROI 1	-4.699	-112.602	103.204	-11.65	9.92
ROI 2	4.556	-100.582	109.694	-11.51	18.43
ROI 3	3.577	-82.128	89.282	-9.11	10.42

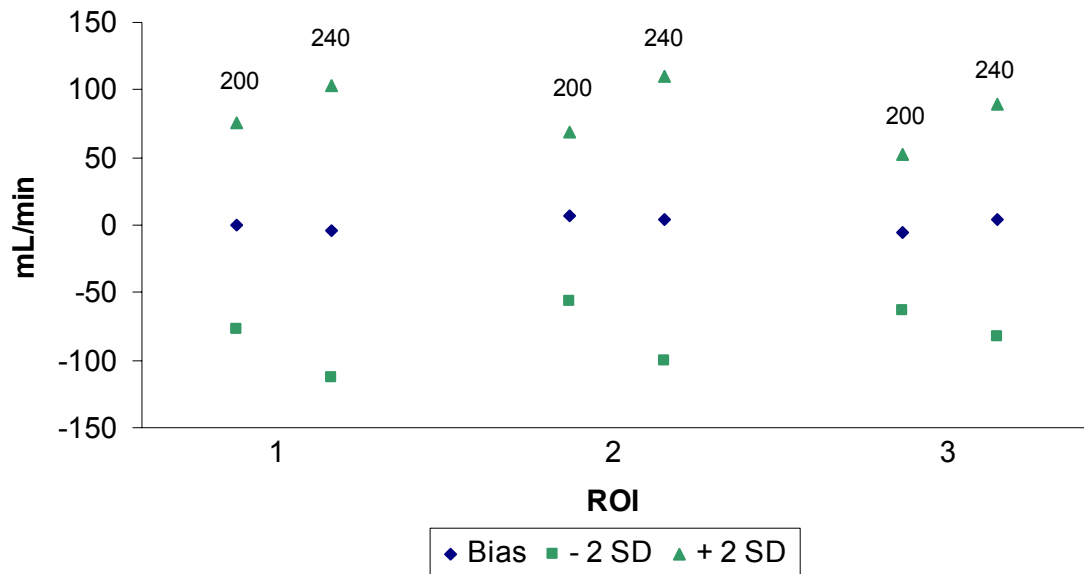


Figure 5-24: Graphical comparison of high-resolution protocol at the 200 mm FOV with protocol velocity-encoded in all three orthogonal planes (240 mm FOV). It is shown that this technique is not useful as compared to high-resolution protocol, as increased variability is observed with all image contours at the 240 mm FOV.

Summary of Findings

Based upon statistical analysis, including the Bland-Altman method and the coefficient of variance (COV), a number of key results have been presented. It has been shown that PVA is a superior phantom material to be used as an MRI quality control phantom. By using a high-resolution gradient-echo technique with 192 phase encodings, experiments at the 160 and 200 mm FOV are shown to be superior to those at the 350 mm FOV. It is also shown that these results are more accurate than low-resolution protocol using 96 phase encodings. Inter- and intraobserver results were excellent, ensuring repeatability of the method, especially at the 200 mm FOV. The multiple-site study, which used images acquired at three locations along the simulated vessel, showed similar results along each channel. This suggested fully-developed and laminar flow, which was also the result of the Reynolds number calculations. The multiple-site study also reinforced the results of the inter- and intraobserver studies, showing that this MRI flow measurement method is both accurate and reproducible. The observation of velocity profiles also illustrated that the flow was steady. Velocity encoding in three directions did not significantly improve data, further suggesting that high-resolution protocol using 192 phase encodings is the most accurate technique for the purposes of the clinical investigation relating to this validation study.

CHAPTER VI

DISCUSSION

In this chapter, the results presented in Chapter V will be discussed and the significance of each finding will be presented. A number of experiments were performed during this study to determine the most accurate protocol to be used in RBF quantification. The tolerance of the MRI flow measurement method under controlled steady-flow conditions, which partially simulated renal arterial blood flow, was also evaluated. This discussion focuses on a variety of MRI parameters and how they have been applied in these experiments to correctly capture flow through a simulated vessel.

Motivation for the Study

The long-term goals of the CRISP study include the capacity to more fully understand how MRI may be used to assess renal circulation. It has been shown that the hemodynamic parameters measured in the renal arteries correlate strongly with the anatomical and functional indicators of ADPKD severity [19]. In the short-term, the outcome of the present validation study may be applied to clinical investigations, resulting in the acquisition of more accurate RBF data. This will further allow clinicians

to understand the processes involved that cause the correlation between RBF and other indicators of ADPKD severity. By having a more complete understanding of these processes, more effective diagnostic and treatment plans may be developed.

Material Evaluation Using PVA, Plastic, and Glass

As stated in Chapter V, the average coefficient of variation (COV) determined using PVA data was consistently less than that of plastic and glass (-9.56% and -3.62% from COV values for plastic and glass, respectively; see Figure 5-2). Serious inconsistencies were observed between the ROI data sets at a single flow rate along the entire range of flow rates observed when using plastic (Figure 5-1) due to various factors. Increased variation between individual measurements performed using each material, as compared to true flow values (Figure 5-1), suggests that there exists more sensitivity to lumen border determination when the surrounding area is air, as the plastic data was acquired in this type of environment. During the PVA and glass experiments, the surrounding environment included PVA and water, respectively. This implies that when the object being imaged is surrounded by air, a low MRI signal intensity results at the lumen boundary, which contributes to velocity estimation errors. PVA and water produce an improved signal, due to the basis of NMR and the inherent magnetic properties that these materials possess as a result of their elemental makeup. PVA is comprised of carbon, hydrogen, and oxygen, which are all NMR active elements, and therefore provide a signal when scanned using MRI. Figure 6-1 displays a comparison of

plastic and PVA data acquired during this study, as compared to *in vivo* tissue found in the renal arteries.

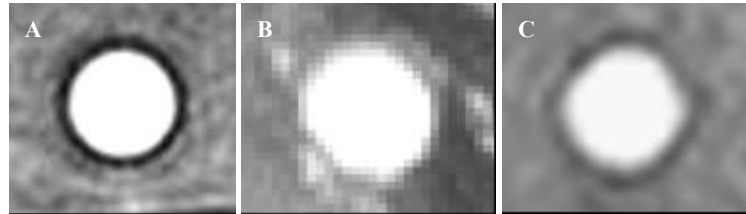


Figure 6-1: *In vitro* and *in vivo* breath-held phase-velocity encoded MRI scans. The plastic material in (A) was found to perform less like the *in vivo* tissue in (B) than the PVA in (C).

As shown by the quantitative data presented in Figures 5-1 and 5-2, as well as the MRI images displayed in Figure 6-1, models using PVA present more realistic vessel lumen than plastic or glass models. A distinct ring is present around the flow region in both plastic (Figure 6-1) and glass models, resulting from the materials' magnetic properties: plastic and glass are incapable of providing a signal comparable to the resultant PVA signal. The PVA model displays a more indefinite wall, as a result of the signal that PVA provides, and is more realistic as compared to vessel lumen observed *in vivo*. It is also important to note that partial volume effects did not seem to be as prevalent when using PVA. The partial volume effect phenomenon occurs because each voxel in the image may represent more than one tissue type, or in this case, type of material. The image value of a particular voxel reflects the average value over the object,

which may be skewed when rapid changes occur across the object. As PVA provides a stronger MRI signal, these changes are not as drastic when this type of model is used, resulting in more correct data less prone to partial volume effects.

PVA is also mechanically comparable to vessel lumen and shares many of the same magnetic properties [25]. These properties are determined by the cross-linking that occurs during the freeze-thaw cycles. During the freezing process, crystal nuclei are formed, which form into larger crystals during the thaw cycle. The crystals act as cross-linking sites for the polymer, which increase in size and number with each cycle, resulting in the rubber-like mold formed in this study.

Chu and Rutt [25] focused on reproducing the elastic modulus of porcine aortas using PVA, in addition to two magnetic properties during their experiment: the T_1 and T_2 relaxation times. Following each pulse, the longitudinal magnetization (M_z) is converted into the transverse magnetization (M_{xy}), which is not oriented along the B_0 field. When the pulse is turned off, the longitudinal magnetization returns to its initial state. The recovery time of the longitudinal magnetization is referred to as the T_1 relaxation time. T_2 relaxation is defined as the decay of transverse magnetization immediately following each pulse when the longitudinal magnetization is completely converted into transverse magnetization (M_{xy}).

Chu and Rutt were able to obtain the range of healthy porcine aortic T_1 and T_2 relaxation times using between two and five freeze-thaw cycles and two to three freeze-thaw cycles, respectively. It is important to note that the PVA cryogel used in the present study was made from a solution containing 30% PVA and 70% water. Lower PVA concentrations (specifically 15% by weight), as discussed by Chu and Rutt, result in

models that exhibit superior imaging properties, but are also more fragile. During initial experimentation in this renal validation study, the cryogel with a concentration of 20% PVA had difficulty withstanding its own weight. However, in smaller vessel model experiments, lower PVA concentrations may be used. By exhibiting some of the same important mechanical and magnetic properties as compared to porcine aortas, PVA is shown to be a superior phantom material as compared to plastic and glass. This statement is further confirmed by the statistical analysis presented in Figures 5-1 and 5-2.

Comparison of High-Resolution Scans: 160, 200, and 350 mm FOV

Field of View

A large portion of the present study focuses on the field of view (FOV) parameter. The FOV is the physical length over which the image extends in both the frequency and phase-encoding directions. In various applications, the image will be square so that a single value for the FOV is specified, which is the case in this study. However, a rectangular FOV may also be used. Data was taken at three different fields of view in these experiments using the high-resolution protocol: the 160 mm, 200 mm, and 350 mm FOV (all square). When observing the data presented in Chapter V (Table 5-2, Figure 5-6 through 5-11), it becomes apparent that minimization of FOV is important in acquiring accurate MRI velocity data to increase data quality and resolution. At the 350 mm FOV, data was more scattered and less accurate as compared to data obtained using the 160 and 200 mm FOV. For example, a comparison of the Bland and

Altman plots using the phase border at the 160 and 350 mm FOV shows an increase in disagreement with the corresponding increase in FOV (Figure 6-2). At the 160 mm FOV, the resultant bias is 4.459 mL/min, while the 95% limits of agreement are -59.845 and 68.763 mL/min. For the 350 mm FOV, the bias is 1.356 mL and the 95% limits of agreement range from -110.958 to 113.669 mL/min for the same region of interest. Although the bias is slightly less, the 95% limits of agreement are significantly greater. This is more accurately portrayed by the lower and upper percent differences, which are equivalent to -15.63 and 23.50 for the 350 mm FOV and -6.28 and 11.88 for the 160 mm FOV. The same pattern was seen throughout these experiments, with the 350 mm FOV data being consistently worse than the results obtained for both the 160 and 200 mm FOV. Similar results were obtained for the 160 and 200 mm FOV; however, this is to be expected, as only a 40 mm difference exists along each length between the two fields of view. The 160 mm FOV did provide slightly better results than the 200 mm FOV, again suggesting that minimization of FOV is important for this study. However, it is important to note that the biases for the 160 and 200 mm FOV were 1.782 and 3.048 mL/min, respectively, with very similar 95% limits of agreement. This difference in the bias of only 1.266 mL/min suggests that using a 200 mm FOV as opposed to a 160 mm FOV should not result in significantly less accurate flow data. As the FOV is decreased, pixel size increases, allowing for more accurate determination of the vessel contour. However, using a 160 mm FOV instead of a 200 mm FOV does not significantly improve the results.

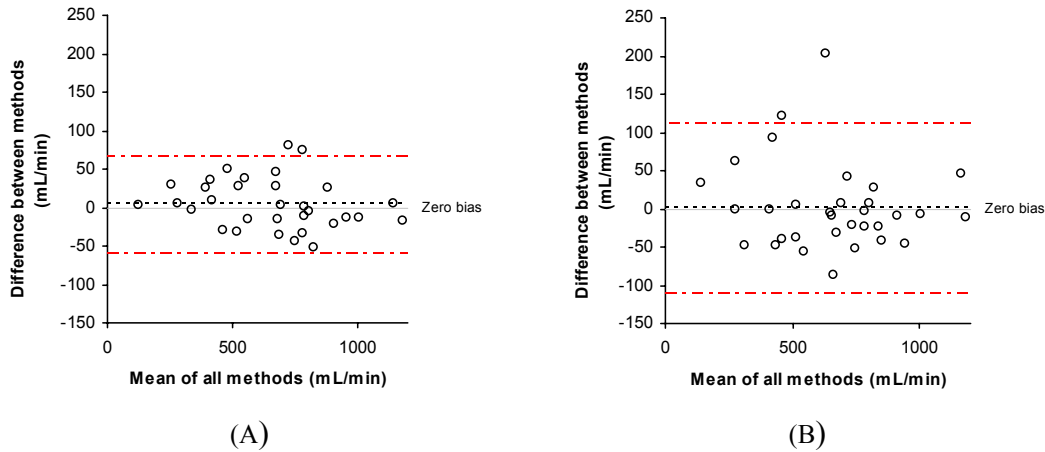


Figure 6-2: Comparison of Bland-Altman plots using the phase border using (A) the 160 mm FOV and (B) the 350 mm FOV. The 95% limits of agreement for the 350 mm FOV data were larger than the 160 mm FOV, indicating that minimization of FOV is important for accurate flow results.

The differences observed in the data are attributed to spatial resolution. As the FOV was increased in the present study, the spatial resolution of the images decreased, which has been attributed to partial volume effects [18]. This change resulted in data with increased deviation from true flow values, as described in previously. By minimizing the field of view, while ensuring that the entire vessel area is captured, more precise flow measurements may be obtained.

Although a larger area of the anatomy is excited when using the 350 mm FOV, the object of study may be too small to accurately determine the lumen border. Throughout the image analysis process, the MRI images taken using the 350 mm FOV had to be magnified in order to determine the lumen border using the “zoom” tool in the FLOW software program. This resulted in a blurred image, causing additional difficulty

in lumen border determination. With improved automatic algorithms, this issue may be resolved. At the 350 mm FOV, the automatic border provided slightly better results as compared to the magnitude and phase borders (Table 5-2), suggesting that with larger fields of view, a precise automatic algorithm may provide superior data as compared to manual determination. Throughout the experiment, the data resulting from the use of the automatic algorithm in the FLOW software program was comparable to both the magnitude and phase borders performed manually, although it did not provide as accurate results using the 160 and 200 mm FOV, or when artifact was present.

Wraparound Artifact

The wraparound phenomenon is also commonly referred to as aliasing. Two types of aliasing may occur during the acquisition of MRI scans: frequency aliasing and phase aliasing. This discussion will focus on phase aliasing, or phase wrap, as this artifact was observed during post-processing.

During MRI acquisition during clinical studies, anatomy outside of the defined FOV can be excited by the RF pulses. Because phase encoding gradients are only scaled for the specific FOV being used, these tissues are not properly phase-encoded relative to their anatomical position. When this occurs, the anatomy outside the FOV “wraps” onto the opposite side of the image, resulting in a MRI scan where anatomy appears to be in the wrong place. During the 3.18 mm diameter experiment in the present study, this phenomenon was observed. Because the “anatomy” surrounding the channel was simply the PVA block, a “black hole” appeared within a number of the phase images; an example of this phenomenon is shown in Figure 6-3. As the flow rate increased, the

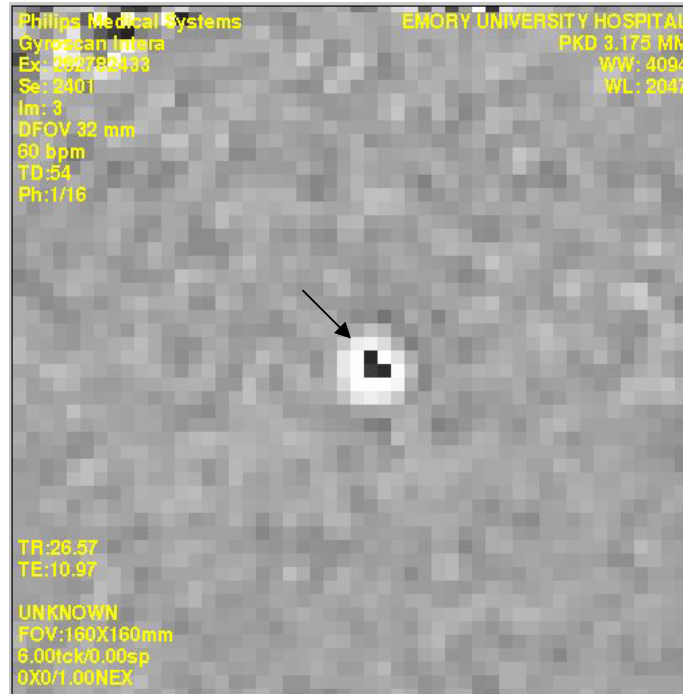


Figure 6-3: Phase image for the 160 mm FOV scan obtained for the 3.18 mm channel experiment. The arrow points to the flow region, which contains the wraparound artifact. This phenomenon is due to the excitation of tissue outside the defined FOV boundary, which causes the anatomy to be displaced from its actual position. This image was corrected by properly encoding the “unwanted” tissue using the phase-unwrap feature in the FLOW software program. These values are presented in Table 6-1.

wraparound artifact became more prominent; however, aliasing was not present in the 350 mm FOV images until the highest flow rate experiment that provided readable images (531.19 mL/min). This observation may be attributed to increased partial volume effects noticed at higher fields of view. In this experiment, the aliasing present in the images is attributed to the values used to define the velocity encoding range. From the resulting data, it appears that the values used were too small to accurately capture velocity images. The velocity encoding values determine the maximum velocity that can be correctly measured without causing aliasing. It is important to note that increasing the velocity encoding range ultimately decreases the velocity-to-noise ratio [100]; however, it has been determined that because the flow velocities, and thereby the flow rates, are integrated over a large number of voxels, increasing the velocity encoding range by a realistic amount (50 to 100 cm/s) does not significantly increase the amount of error [18]. The decrease in velocity resolution may however have an effect on accurately acquiring peak flow velocity measurements [18]. This bears a certain degree of importance in the application of phase-velocity encoded MRI to ADPKD clinical evaluation, as the ability to distinguish between slow-flowing and stagnant blood is diminished with decreased resolution. In hypertensive ADPKD patients, it is important to have the ability to differentiate between these two types of flow patterns.

In order to correct phase wrap, a number of steps may be taken. A larger field of view may be used, presaturation pulses may be applied to the undesired tissue, or the unwanted “tissue” may be correctly velocity-encoded [94]. As shown by the 350 mm FOV experiments, increasing the field of view seems to hide the phase wrap artifact in most cases; however, decreased spatial resolution is again observed and the velocities

may not be correct. For the remaining experiments, the images were correctly phase-encoded during post-processing. This was accomplished using the “phase-unwrap” feature in the FLOW software program, which is based upon Equation (6-1),

$$v_{corr} = v + 2v_{enc} \quad (6-1)$$

where v_{corr} is the corrected velocity and v_{enc} is the velocity-encoding value used (100 cm/s in this study). Table 6-1 shows the values used for each scan used to correct each image, and it is important to note that the velocity range is 200 cm/s, or twice the velocity-encoding value. By correctly encoding the images, accurate flow data was obtained; however, it is important to note that the automatic border detection algorithm built into the software program did not accurately capture the vessel border in these affected images. This is an issue that should be further looked into by software programmers, in order to decrease the amount of time required for data analysis while also providing accurate velocity and flow results. Although the images in the present *in vitro* experiment were correctly velocity encoded during analysis, it is important to note that the ability to recognize aliasing becomes more difficult using images obtained during *in vivo* clinical exams. Care should be taken during clinical exams in order to obtain correct flow measurements while simultaneously avoiding aliasing.

Table 6-1: Parameters used to correct wraparound artifact for 3.175 mm simulated vessel. v_{min} and v_{max} are provided for each scan corrected. It is important to note the direct relationship between FOV and the degree of aliasing: as the FOV increases, the degree of phase wrap increases, as well.

Flow Rate (mL/min)	FOV (mm)	v_{min} (cm/s)	v_{max} (cm/s)
377.96	160	-76	124
377.96	200	-86	114
397.69	160	-70	130
397.69	200	-79	121
531.19	160	-40	160
531.19	200	-51	149
531.19	350	-74	126

Background Subtraction

The results presented in Table 5-2 show that the background-subtraction method does not significantly improve the results, if improvement is observed at all. This is further confirmed in Figures 5-14 and 5-15. A table summarizing the results shown in these figures is provided in Table 6-2. Although all COV values are within 5 percent, in all but one experiment (160 mm FOV, ROI 2), the background subtraction actually increased the COV. Because the PVA mold provides a static signal, it was expected and is shown that the data obtained using the background-subtraction method does not drastically alter these measurements. Similar results have been presented in previous studies where correcting for DC phase errors did not result in more accurate flow measurements [18, 21]. Under *in vitro* conditions, artifactual phase shifts are at a minimum, causing no improvement in results when applying a first-order background phase correction algorithm [18]. However, this background-subtraction method may be

valuable during *in vivo* clinical investigations, where other vessels and anatomical structures have the capability of producing a more dynamic background signal.

The background-subtraction results do show that diffusion through the PVA mold was not present, as there is an absence of background velocity. During certain experiments, specifically at high flow rates, leaks occurred at the entry and exit points where the Teflon tubing was inserted into the phantom casing and PVA mold. Although this issue was immediately addressed and all efforts were made to prevent leaks, the faulty connections between the Teflon tubing and the PVA may be an overall cause of error in this validation study. Flow rates were experimentally measured using the weight determination method before and after each set of scans, but not simultaneously. Efforts were also made to obtain the flow rates using digital flow probes. This method was rejected due to the appearance of artifacts during the scans. Even though a minimum number of connections were used throughout the flow loop to prevent leaks and air saturation of the glycerin and water solution, leaks often persisted at the highest flow rates for each channel diameter, and may contribute to the error observed between the true and experimental MRI flow values.

Table 6-2: Resulting COV values between true flow and flow measured using velocity-encoded MRI (graphically shown in Figures 5-14 and 5-15). Background subtraction actually increased the COV between the true flow MRI flow in all experiments, with the exception of ROI 2 using the 160 mm FOV.

	COV (%)	
	No BG	BG
160 FOV		
ROI 1	2.96	3.33
ROI 2	3.08	3.03
ROI 3	3.11	3.32
200 FOV		
ROI 1	3.61	4.07
ROI 2	2.99	3.17
ROI 3	2.85	3.12

Region of Interest

In the high-resolution scans, ROI 2 (the phase contour) provided the most accurate results in terms of the lower and upper percent differences when comparing the 160 and 200 mm FOV data (Table 5-2). By taking into account the amount of bias present, the corresponding data may be altered accordingly, providing more accurate MRI flow results. When the contour is manually traced in the phase image, velocity components (in cm/s) are used to outline the region of interest. In the magnitude image (ROI 1), the manual tracing is less quantitatively defined, and as hypothesized, it does not provide results with the same amount of accuracy as compared to ROI 2. Although the results obtained with the use of the automatic border detection algorithm are reasonably

comparable to the results from the phase image, it is important to note that this method provides slightly less accurate results.

Throughout this study, it has been discussed how the automatic detection algorithm did not perform as well as expected under certain circumstances, specifically when artifacts are observed in the images. Therefore, it is not recommended that the same automatic program be used for *in vivo* studies. However, other studies have shown that certain “in-house” programs have more accurately captured the lumen boundary, both *in vivo* and *in vitro* [20-21, 54]. Such an algorithm has been applied to flow in the ascending aorta as defined by van der Geest et al. [54], in which manual tracing of the contours required approximately ten minutes, while only six seconds were required with the use of the automated contour detection program. Inter-and intraobserver variabilities were less than two percent for both the manual and the automated methods in this study, suggesting a precise automatic algorithm. The application of a similar automated process would enhance the clinical applicability of MR flow velocity mapping to the renal arteries. The use of an automated algorithm may also reduce interobserver variability of the multiphase studies, although the error observed between subjects in this study was minimal.

It is also interesting to note the correlation between the FOV and the different regions of interest. As the field of view was decreased, the statistical differences observed between ROI 1 (magnitude border) and ROI 2 (phase border) became less (Table 5-2). At the 160 mm FOV, the lower percent difference decreased by only 0.11% while the upper percent difference increased by 0.19% when going from ROI 1 to ROI 2. This result further shows the increased spatial resolution observed with a decrease in

FOV. As ROI 1 is based more upon the evaluator's interpretation of the contour, it is implied that the increased resolution resulting from the decrease in FOV improves the accuracy of the evaluator, as shown by comparing ROI 1 to ROI 2 (Figures 5-6 and 5-7).

Low-Resolution Scan Comparison: 160, 200, and 350 mm FOV

In order to assist in determining the best protocol, low-resolution scans were also performed at the same fields of view as in the high-resolution scans. Changes in protocol resulted in flow rate values being closer to the true flow values for the high-resolution data acquisition using 192 phase encodings as compared to the low-resolution data, which used only 96 phase encodings. Overall, an increase was observed in all quantitative parameters for the low-resolution protocol comprising the Bland and Altman plots, including the bias, 95% limits of agreement, and lower and upper percent differences (Table 5-3, Figures 5-16 through 5-18). This assists in showing that an increase in the number of phase encodings from 96 (low-resolution) to 192 (high-resolution) improves the data. This result was also expected, as less detail exists in the phase-encoding direction with each decrease in the number of phase encodings. However, the increase in the number of phase encodings to 192 increased the image acquisition time from 20 to 30 seconds. This effect was expected as the total imaging time is defined by Equation (6-3),

$$\text{Total imaging time} = 2 \times (\text{TR}) \times (\text{NSA}) \times (\text{Number of phase encodings}) \quad (6-3)$$

where TR is the relaxation time and NSA is the number of signal averages. The total imaging time is multiplied by two (shown in Equation 6-3) because of the velocity encoding. The scan time increase may have a slight impact on patients undergoing clinical investigation. Because these scans are breath-held, certain individuals will experience difficulty having the scans performed. This includes, but is not limited to, individuals who do not have the ability to hold their breath for an extended amount of time due to illnesses affecting their respiratory system, small children, and elderly patients. As MRI technology continues to improve, this problem will be addressed, and scan times will be reduced while the same, or improved, high-resolution protocol is maintained.

Based upon the comparison of the low-resolution and high-resolution results in this *in vitro* study, the number of phase encodings in the CRISP protocol was increased in order to obtain the most accurate patient data possible. Although this increased acquisition time by 10 seconds, it has been shown through the present phantom study that increasing the number of phase encodings results in more precise velocity data.

Multiple-Site Study

In order to assess the flow characteristics present in the phantom model, as well as the overall reproducibility of the MRI flow measurement method, the multiple-site test was performed by scanning the simulated vessels in three sites using three defined planes

perpendicular to the direction of flow. The 200 mm FOV was used for this experiment. It was hypothesized that sites 2 and 3 (Figure 5-21), located between the entry and exit points and the site 1 of the model, would provide equivalent flow data, based upon the entry-length tubing calculations (Equation (4-1)) and the fact that the model did not introduce any directional flow changes. Based upon the results obtained using the Bland-Altman statistical method, it is shown that the flow in this experiment was fully developed.

The Bland and Altman plots shown in Figures 5-22 and 5-23 show that ROI 2 (phase contour) again provides the most accurate results. The bias for ROI 2 was 0.372 mL/min, while the bias for ROI 1 (magnitude contour) equaled 4.784 mL/min. The 95% limits of agreement were also closer for ROI 2 than for ROI 1 (-18.959 to 19.702 and -27.288 to 36.856, respectively). These results may have been slightly more accurate if the 160 mm FOV was used instead of the 200 mm FOV, based upon earlier discussion in this chapter. However, it is hypothesized that such a change would not have resulted in a significant improvement, based upon the results for the 160 and 200 mm FOV high-resolution data. From the statistical analysis pertaining to the multiple-site experiments, it is shown that the flow throughout the model was fully-developed (Figure 5-22 and 5-23). Based upon these same results, the overall reproducibility of the MRI flow measurement method is also confirmed.

Using the FLOW software program, velocity curves were generated as a function of time for each data set. These were observed during post-processing, and as stated previously, flow rate measurements were all within 2 mL/s of one another, with the

majority of points measuring within 0.5 mL/s. These velocity profiles suggest that the flow was also steady throughout the model for the duration of the experiment.

Reynolds numbers were also calculated for each channel diameter at each experimental flow rate. The highest Reynolds number present in the experiment was approximately 1461, showing that turbulent flow should not have been present during any experiment in this study, as the transition into turbulent flow does not begin until a Reynolds number of 2100 for this type of experimental setup. Three-dimensional velocity encoding was used to further investigate this specific flow characteristic. As discussed here, the flow in this experiment may be characterized, as steady, laminar, and fully-developed.

It is important to note that the described flow characteristics in this model are not a truly accurate representation of the flow observed *in vivo*. The purpose of this study was first to determine and suggest protocol that may be used to obtain accurate blood flow measurements during clinical investigation. In order to do so, a steady and laminar flow was used, as the flow rate should be constant throughout the model when observing flow with the described characteristics. Pulsatile flow will be used in later research to more accurately represent *in vivo* flow characteristics.

Velocity Encoding in Three Directions

By experimenting with velocity encoding in all three orthogonal directions, it was further shown through statistical analysis that the flow in the model was laminar and

fully-developed (Table 5-5, Figure 5-24) . Flow was only present in a single direction, and the results were highly comparable to those obtained using the 200 mm FOV, specifically the bias values. The 95% limits of agreement were greater in both the positive and negative directions for the 240 mm FOV three-dimensional scan. This increase may be attributed to the increase in field of view. Although velocity encoding does not improve results in this *in vitro* validation, this technique may be applied to *in vivo* clinical studies, where more complex three-dimensional flow fields may be present.

This discussion has presented the effects of altering a number of MRI parameters as applied to the range of vessel diameters observed in the renal arteries. A number of experiments were performed during this study to determine the most accurate protocol to be used in RBF quantification. Based upon these results and discussion, a specific protocol was formulated to provide the most correct data obtainable using phase-velocity encoded MRI, and is presented in the next chapter.

CHAPTER VII

CONCLUSIONS

In the present study, a number of acquisition parameters were experimentally tested to observe their effects on the accuracy of resulting image data using a phantom with biomechanical and MR signal properties similar to the properties possessed by aortic tissue with a laminar flow profile. The more closely the materials composing the phantom mimic tissue parenchymae with respect to the relevant physical and chemical properties, the more valuable the phantom. As such, various materials were initially tested, with PVA being selected as the material of choice based upon its ability to mimic vessel properties. The importance of surrounding the simulated vessel with a material providing a good MRI signal has been shown, as increased velocity estimation errors were observed when the “vessel” under examination was surrounded by air. This error was attributed to a low MRI signal intensity occurring at the lumen boundary.

It has been shown that certain parameters do not make a significant impact on the preciseness of results, such as three-dimensional velocity encoding. Other parameters, such as field of view, have a certain impact on the correctness of velocity data obtained during image acquisition. As the FOV was increased in this study, the spatial resolution of the images decreased, which has been attributed to partial volume effects [18]. As FOV is increased, pixel size decreases, resulting in less accurate flow data. This change

resulted in data with increased deviation from true flow values, suggesting that minimization of FOV is important in obtaining correct flow measurements. This is statistically depicted through the presentation of the Bland-Altman plots and the average COV calculated for each field of view. Both the 160 and 200 mm FOV presented similar results, while results from the 350 mm FOV were much less accurate. Data obtained using the 160 mm FOV provided slightly better results as compared to the 200 mm FOV, but did not significantly improve the flow data. In this study, manual drawing techniques were also used and proved to be accurate with small inter- and intraobserver differences, specifically in the phase image map (ROI 2). The multiple-site study also confirmed the reproducibility of the flow measurement method. The semiautomated vessel edge detection program built into the FLOW software program did not provide improved results. Previous studies have shown that “in-house” automated methods improve results while also decreasing the time required for image analysis [18, 54, 101]. However, it is important to note that these methods were most likely tailored to the specific images acquired in each of these experiments.

The flow characteristics used in this validation study may be classified as steady, laminar, and fully-developed flow, as shown in the multiple-site study. This was shown by the agreement in the Bland-Altman plots and the corresponding COV values, which were equal to less than 2% for both ROI 1 and ROI 2. Velocity profiles obtained from each scan set showed the flow to be steady, and also reinforced that the flow was indeed laminar. Because velocity data resulted from acquisition in only a single orthogonal plane, instead of all orthogonal planes, it was observed that no turbulent or complex flow patterns were observed throughout the simulated vessels.

In conclusion, the results presented here show that breath-held phase-velocity encoded MRI has the capability of becoming a non-invasive diagnostic tool to clinically investigate the hemodynamic characteristics of flow through the renal arteries. Accurate data was obtained for the entire range of arterial sizes representing a healthy and diseased population of children and adults. Once the spatial resolution is appropriate for a specific vessel size through minimization of field of view, flow data may be obtained with a high degree of confidence. High-resolution scans (192 phase encodings) further improved measurement accuracy as compared to lower-resolution protocol previously used (96 phase encodings). As the number of phase encodings was increased, additional detail was observed in the images, causing this protocol to be more efficient at capturing important flow data near the simulated vessel wall. The increase in number of phase encodings from 96 to 192 suggests that the number of phase encodings should be maximized without making the image acquisition time too long for a breath-held scan. These results show that when using current breath-hold MR flow-imaging technology, it is feasible to capture an accurate assessment of the hemodynamic changes observed with the progression of ADPKD, which may further assist in understanding the pathogenesis of the disease.

Based upon this research, the parameters that were tested and provide the most accurate flow data for the artery sizes present in the renal arteries use a FOV of 160 mm \times 160 mm with 192 phase encodings. The remaining parameters that were used with these experiments, which provide the most correct data are as follows: repetition time (TR) = 24 ms, echo time (TE) = 11 ms, and flip angle = 35°. A multi-shot echoplanar imaging sequence (FE-EPI) was also used during this study.

Although these results indicate that clinical studies performed using the same protocol may result in accurate *in vivo* measurements, and despite efforts to mimic *in vivo* vessel conditions (biomechanical and magnetic properties, vessel size) and similar flow rates, the resulting recommendations should be applied to the clinical arena with caution. The substantial difference in preciseness of measurements observed between the low-resolution (96 phase encodings) and high-resolution (192 phase encodings) prompted CRISP to change its patient protocol, accordingly, by increasing the number of phase encodings to 192. This validation study was the first step in showing that velocity-encoded MRI may be used to accurately obtain flow data in the range of vessel diameters observed in the renal arteries *in vivo*. Further research will be performed using pulsatile flow characteristics in order to further improve data acquisition methods that may be applied to ADPKD clinical studies with a high degree of confidence.

CHAPTER VIII

RECOMMENDATIONS

Although numerous steps were taken in order to mimic *in vivo* conditions in the described experiments, certain improvements may be made in order to obtain more accurate data for the purposes of the CRISP clinical study, as well as other studies focusing on the renal arteries, that the present validation study supports.

Most importantly, for the purposes of applying phase-velocity encoded MRI to the renal arteries, pulsatile flow should be introduced into the experimental setup. *In vivo* blood flow measurement is considerably more complex than the laminar flow model presented in this study. Blood is non-Newtonian, and the flow profile depends on the time in the heart cycle and the particular vessel in question [63]. By using a pulsatile pump with a predetermined waveform, this issue may be addressed. This recommendation is now being investigated in the Frederik Philips Magnetic Resonance Research Center at Emory University in Atlanta, Georgia, where the present study was also performed.

In this study, only a small sample of the effects of altering the plane angle relative to the vessel was observed. Although it has been recently shown that this alteration has no significant effect on the flow data [18], it should be further investigated as applied to the renal arteries.

Although the use of PVA assisted in creating a vessel similar to that found *in vivo*, its use presented certain difficulties, as well. With time, the PVA mold physically shrank, and a new PVA mold was required. Although it is not extremely difficult to rebuild the mold, certain inconsistencies in the properties of the mold may have been present. To date, no other materials exist that possess the same biomechanical and magnetic properties and also have an extended life cycle. Thus, extreme care should be taken in creating identical phantoms for the purpose of long-term MRI validation. During the study, difficulty was also experienced in maintaining the position of the entry- and exit-length tubing inside the PVA. Therefore, improvements should be made to the model to increase the friction between the PVA and the Teflon tubing by changing the profile of the Teflon tubing or using a bonding agent that adheres to both PVA and Teflon.

In these phantom experiments, the simulated vessels were stationary, and no dynamic motion was involved; however, it would be tedious to create a complex phantom comprised of moving arteries with PVA. It is more difficult to obtain accurate data in human subjects, as renal arteries exhibit motion and cross-sectional shape changes throughout the cardiac cycle. Certain programming improvements should be made to improve the accuracy of automatic contour detection algorithms in order to decrease the amount of time required for post-processing, without diminishing the correctness of the velocity data. The automatic detection algorithm used in this validation study was shown to have numerous inaccuracies; it is therefore recommended that this specific program should not be used for clinical purposes. It has been discussed how other studies have obtained improved results using “in-house” automatic algorithms, and thus, the need for

an improved algorithm for renal applications certainly exists and should be applied in clinical investigation. The described automatic program should also have the ability to correctly detect the vessel boundary when artifacts are present. Based upon the discussion of the difficulty in observing certain aliasing effects *in vivo*, an accurate detection algorithm having the ability to correct for these effects would be invaluable.

It is also important to note that *in vivo* studies present additional challenges in image acquisition and analysis. In the renal anatomy, there is a presence of supernumerary arteries. Even with improved techniques, MR sometimes fails to depict accessory arteries, which may be identified by conventional angiography. With improved MRI technology providing increased resolution, it is hypothesized that the need for conventional angiography to be performed in conjunction with MR scans will become less important, as these smaller arteries become more visible. However, in the meantime, conventional angiography should be used to observe these smaller arteries when the need arises.

Although certain improvements must be made to more accurately apply phase-velocity encoded MRI to obtain renal blood flow measurements, the current study provides an excellent basis for the application of phase-velocity encoded MRI to the renal arteries. Further research will continue to make various adjustments to the protocol, improving the data acquired and increasing confidence in using this non-invasive modality.

APPENDIX A

BLAND-ALTMAN PLOTS

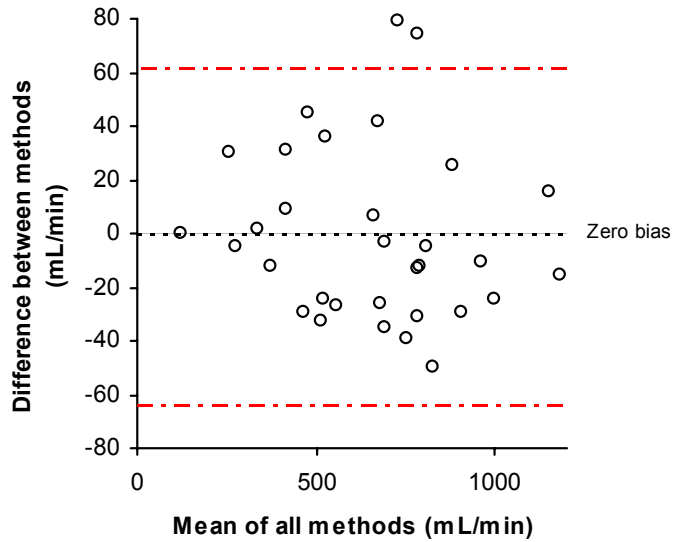


Figure A-1: Bland and Altman plot displaying the difference between the true flow values and the experimental MRI data ($n = 32$). This plot corresponds to the contour drawn in the magnitude image (ROI 1) without background correction at 160 mm FOV.

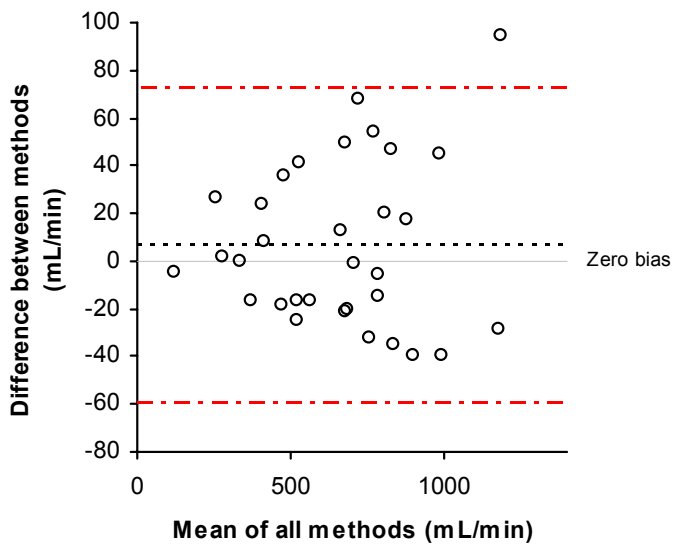


Figure A-2: Bland and Altman plot displaying the difference between the true flow values and the experimental MRI data ($n = 32$). This plot corresponds to the contour drawn in the magnitude image (ROI 1) with background correction at 160 mm FOV.

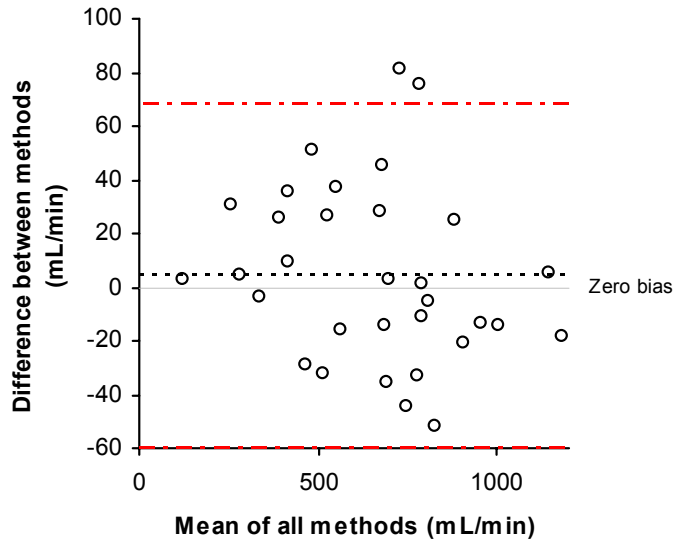


Figure A-3: Bland and Altman plot displaying the difference between the true flow values and the experimental MRI data ($n = 32$). This plot corresponds to the contour drawn in the phase image (ROI 2) without background correction at 160 mm FOV.

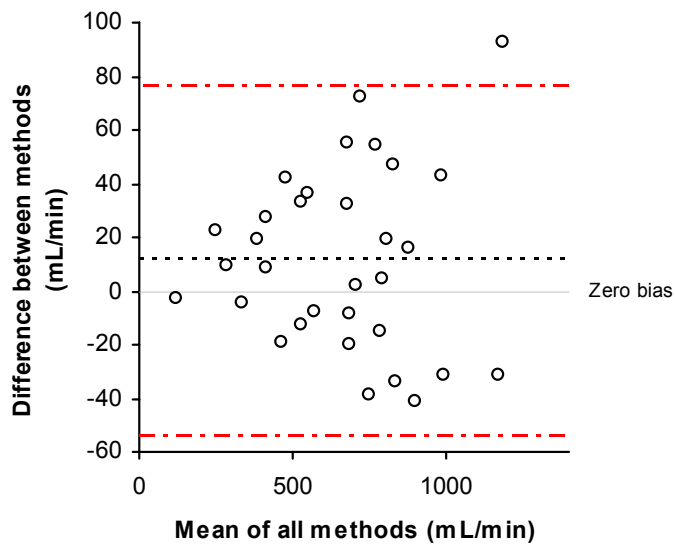


Figure A-4: Bland and Altman plot displaying the difference between the true flow values and the experimental MRI data ($n = 32$). This plot corresponds to the contour drawn in the phase image (ROI 2) with background correction at 160 mm FOV.

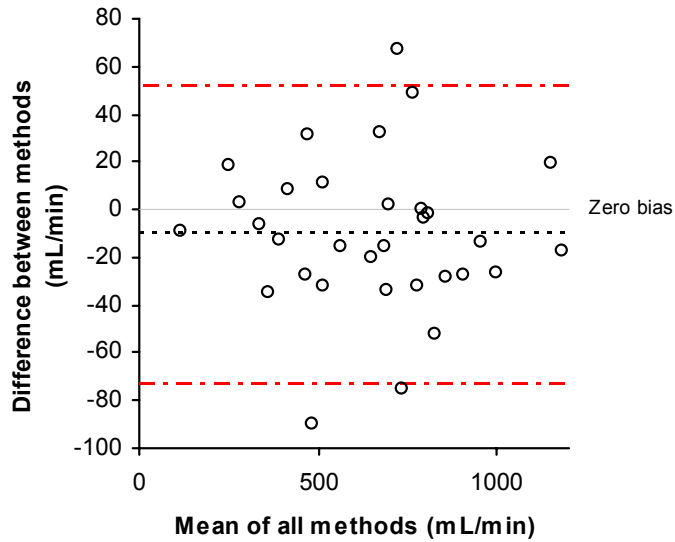


Figure A-5: Bland and Altman plot displaying the difference between the true flow values and the experimental MRI data ($n = 32$). This plot corresponds to the automatic contour drawn in the phase image (ROI 3) using the algorithm in the FLOW software without background correction at 160 mm FOV.

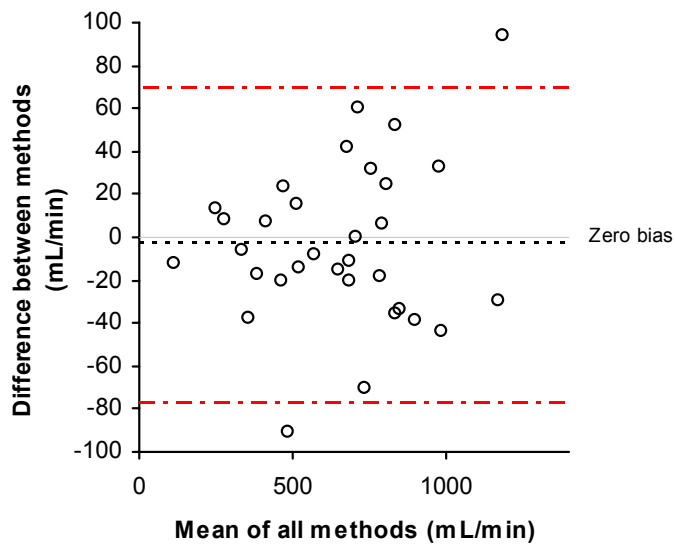


Figure A-6: Bland and Altman plot displaying the difference between the true flow values and the experimental MRI data ($n = 32$). This plot corresponds to the automatic contour drawn in the phase image (ROI 3) using the algorithm in the FLOW software with background correction at 160 mm FOV.

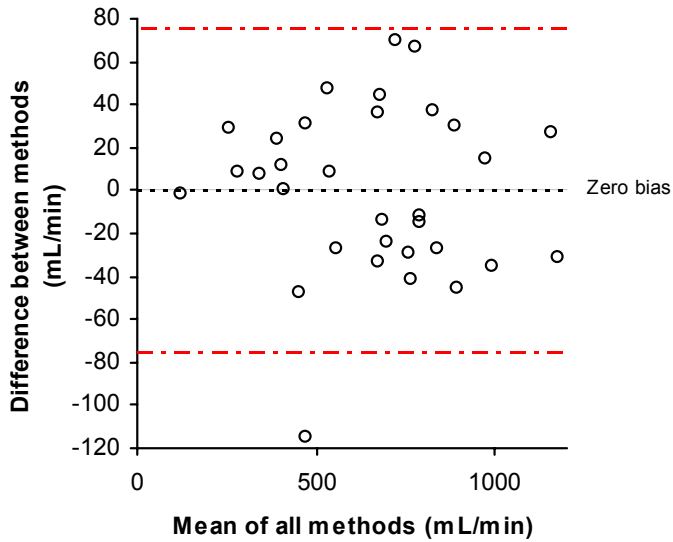


Figure A-7: Bland and Altman plot displaying the difference between the true flow values and the experimental MRI data ($n = 32$). This plot corresponds to the contour drawn in the magnitude image (ROI 1) without background correction at 200 mm FOV.

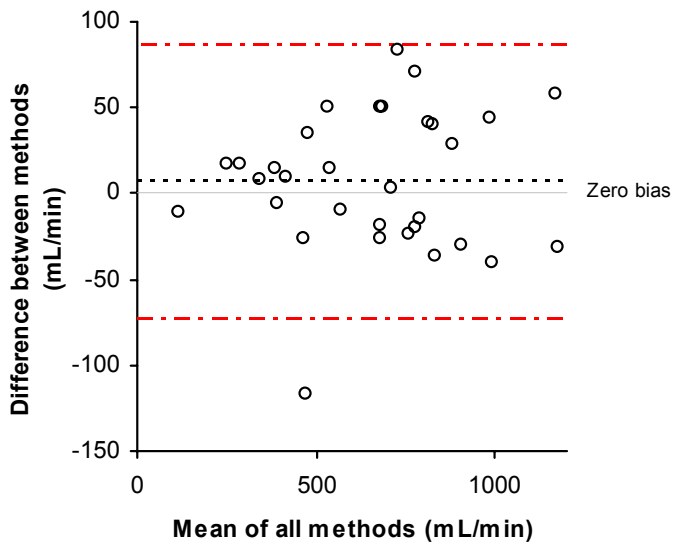


Figure A-8: Bland and Altman plot displaying the difference between the true flow values and the experimental MRI data ($n = 32$). This plot corresponds to the contour drawn in the magnitude image (ROI 1) with background correction at 200 mm FOV.

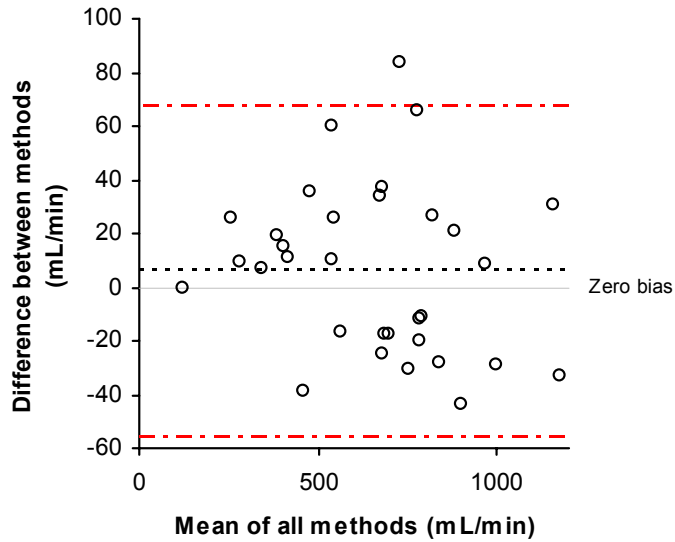


Figure A-9: Bland and Altman plot displaying the difference between the true flow values and the experimental MRI data ($n = 32$). This plot corresponds to the contour drawn in the phase image (ROI 2) without background correction at 200 mm FOV.

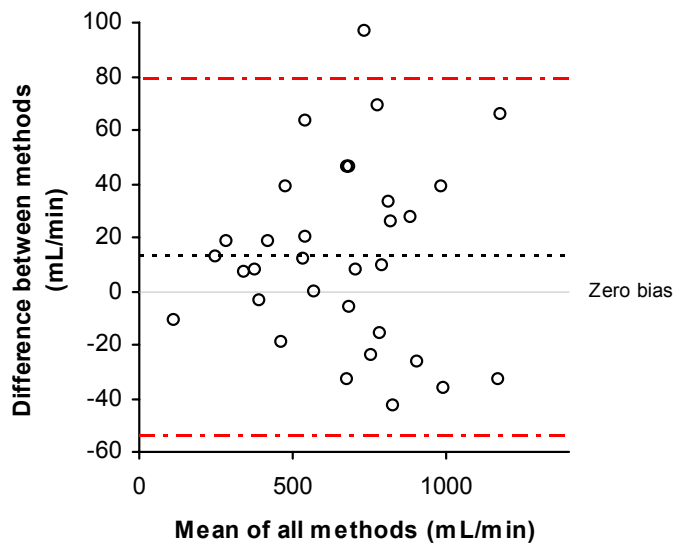


Figure A-10: Bland and Altman plot displaying the difference between the true flow values and the experimental MRI data ($n = 32$). This plot corresponds to the contour drawn in the phase image (ROI 2) with background correction at 200 mm FOV.

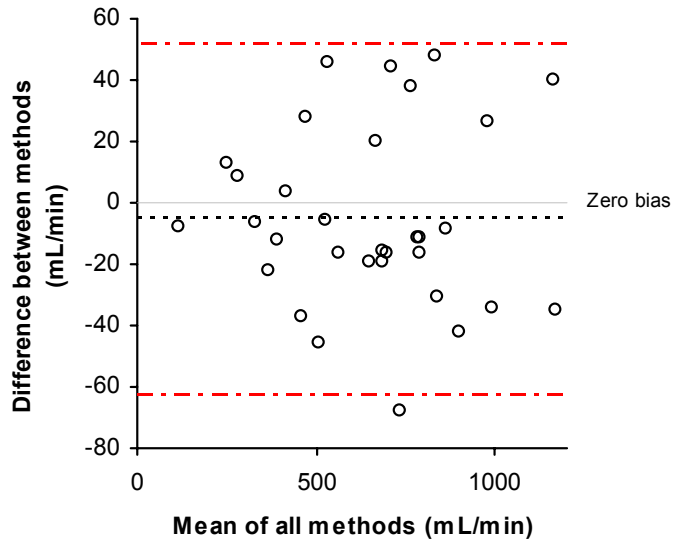


Figure A-11: Bland and Altman plot displaying the difference between the true flow values and the experimental MRI data ($n = 32$). This plot corresponds to the automatic contour drawn in the phase image (ROI 3) using the algorithm in the FLOW software without background correction at 200 mm FOV.

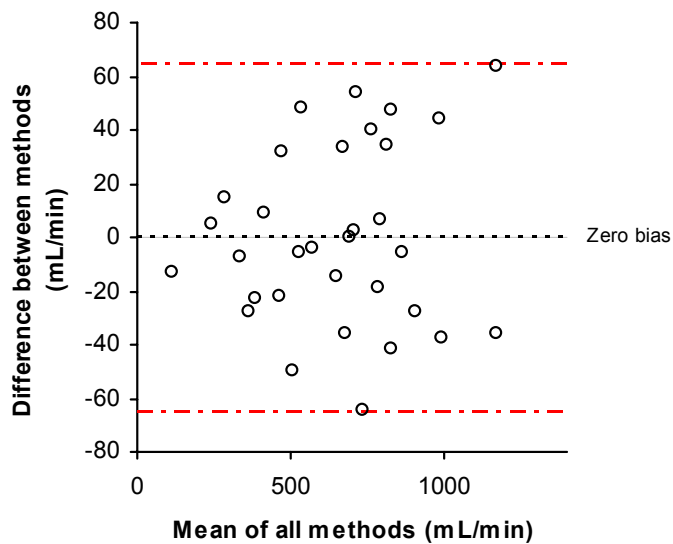


Figure A-12: Bland and Altman plot displaying the difference between the true flow values and the experimental MRI data ($n = 32$). This plot corresponds to the automatic contour drawn in the phase image (ROI 3) using the algorithm in the FLOW software with background correction at 200 mm FOV.

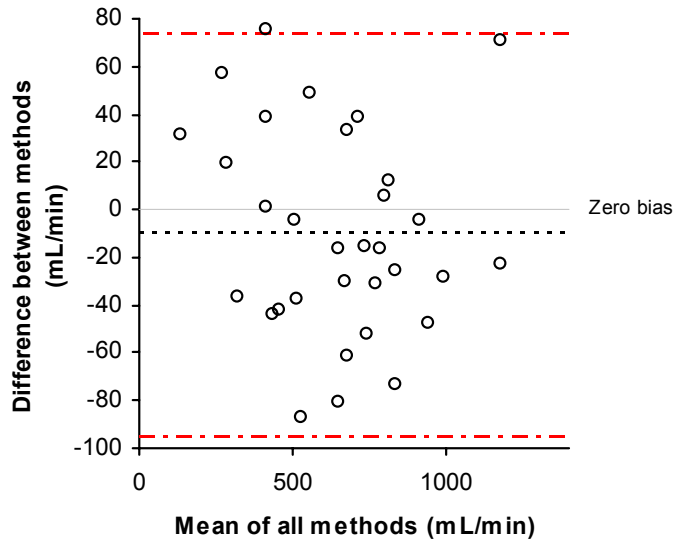


Figure A-13: Bland and Altman plot displaying the difference between the true flow values and the experimental MRI data ($n = 32$). This plot corresponds to the contour drawn in the magnitude image (ROI 1) without background correction at 350 mm FOV.

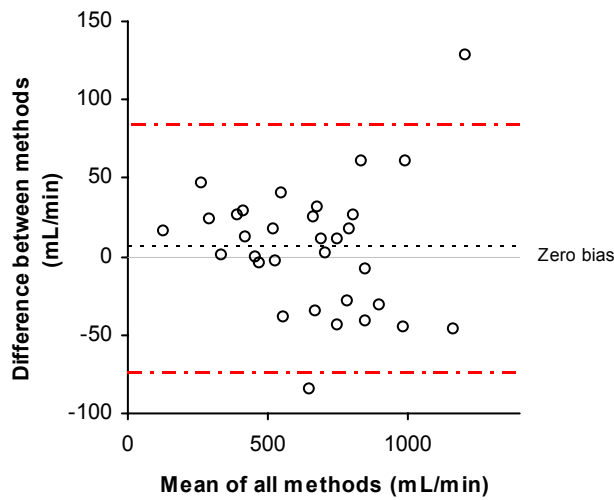


Figure A-14: Bland and Altman plot displaying the difference between the true flow values and the experimental MRI data ($n = 32$). This plot corresponds to the contour drawn in the magnitude image (ROI 1) with background correction at 350 mm FOV.

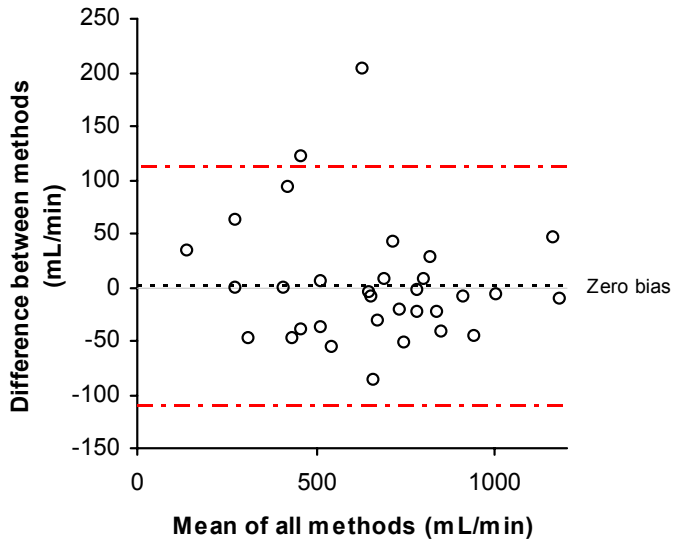


Figure A-15: Bland and Altman plot displaying the difference between the true flow values and the experimental MRI data ($n = 32$). This plot corresponds to the contour drawn in the phase image (ROI 2) without background correction at 350 mm FOV.

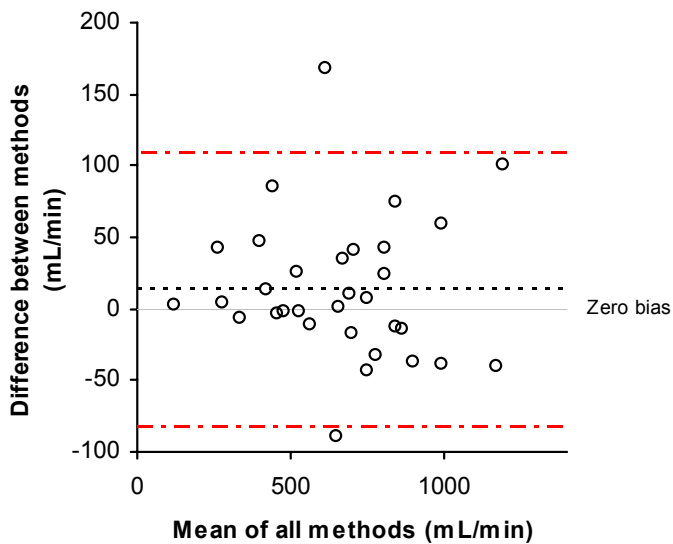


Figure A-16: Bland and Altman plot displaying the difference between the true flow values and the experimental MRI data ($n = 32$). This plot corresponds to the contour drawn in the phase image (ROI 2) with background correction at 350 mm FOV.

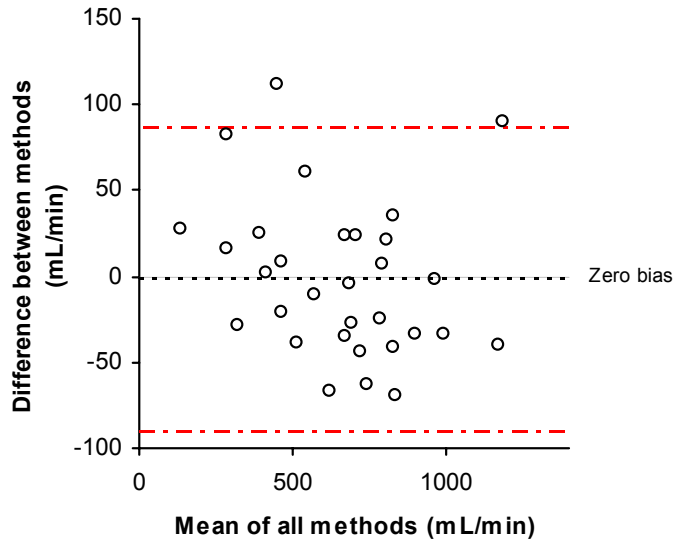


Figure A-17: Bland and Altman plot displaying the difference between the true flow values and the experimental MRI data ($n = 31$). This plot corresponds to the automatic contour drawn in the phase image (ROI 3) using the algorithm in the FLOW software without background correction at 350 mm FOV.

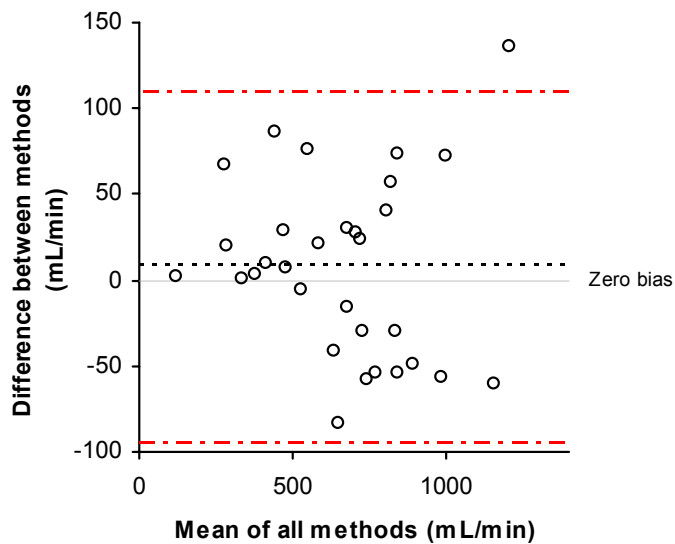


Figure A-18: Bland and Altman plot displaying the difference between the true flow values and the experimental MRI data ($n = 31$). This plot corresponds to the automatic contour drawn in the phase image (ROI 3) using the algorithm in the FLOW software with background correction at 350 mm FOV.

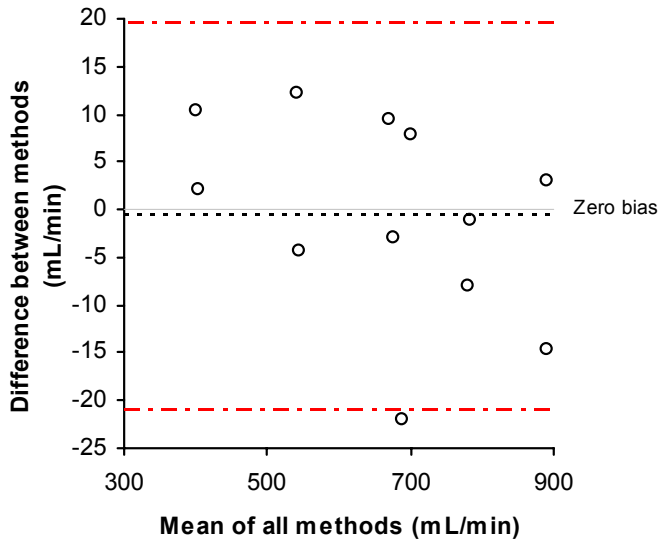


Figure A-19: Bland and Altman plot displaying the difference between methods using two independent and blinded observers at the 160 mm FOV (interobserver study).

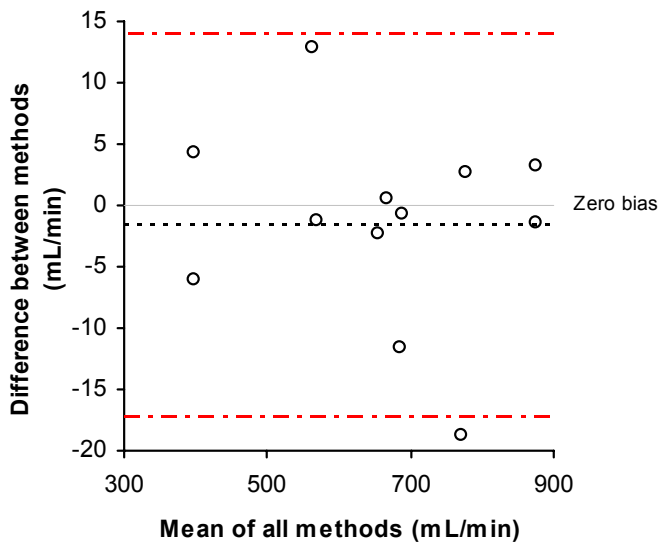


Figure A-20: Bland and Altman plot displaying the difference between methods using two independent and blinded observers at the 200 mm FOV (interobserver study).

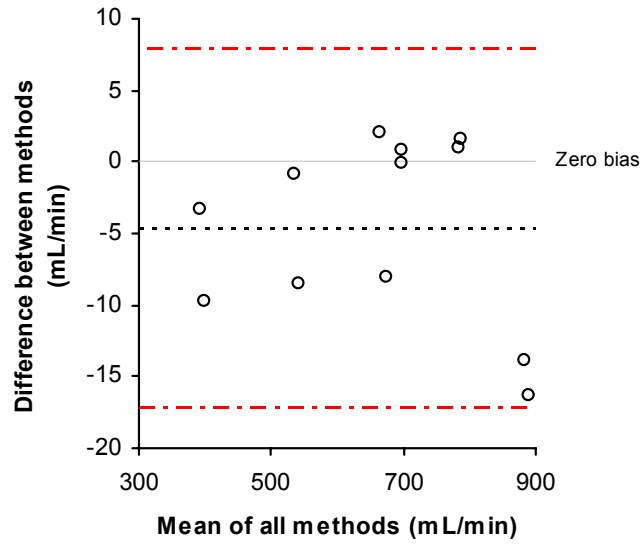


Figure A-21: Bland and Altman plot displaying the difference between methods using a single observer at two different dates at the 160 mm FOV (intraobserver study).

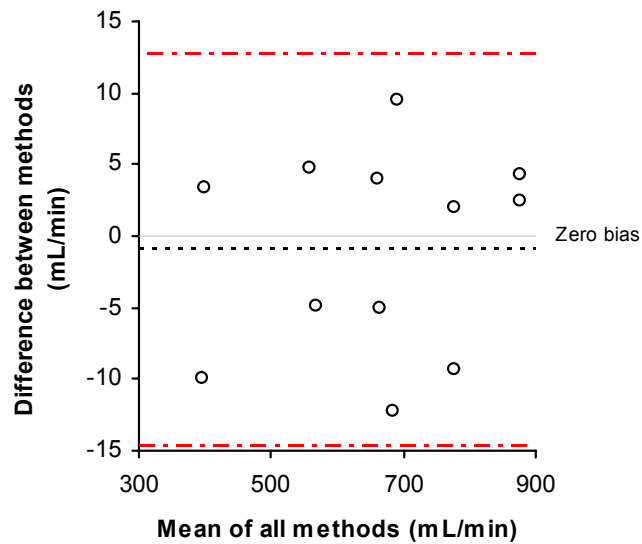


Figure A-22: Bland and Altman plot displaying the difference between methods using a single observer at two different dates at the 200 mm FOV (intraobserver study).

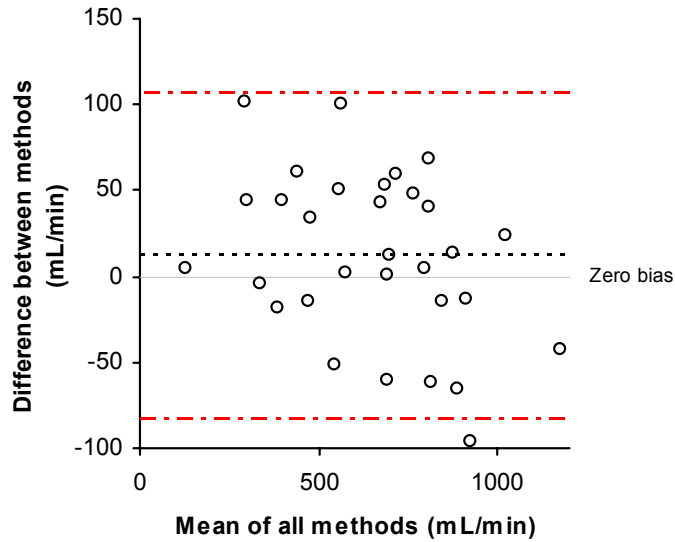


Figure A-23: Bland and Altman plot displaying the difference between the true flow values and the experimental MRI data using a low-resolution protocol ($n = 32$). This plot corresponds to the contour drawn in the magnitude image (ROI 1) at 160 mm FOV.

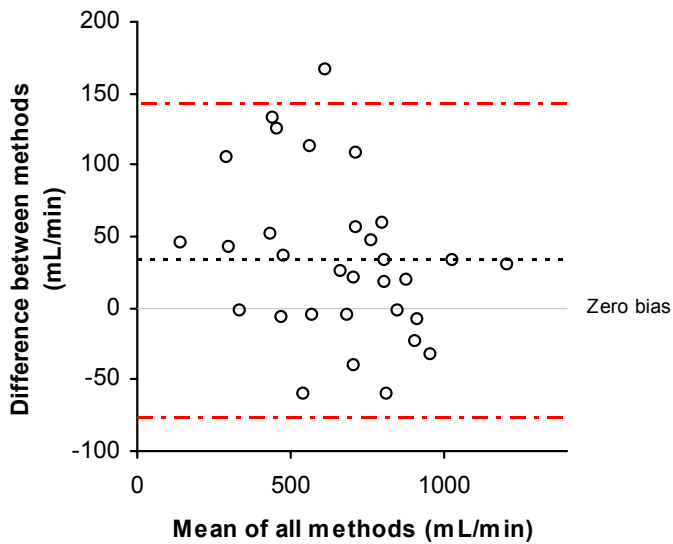


Figure A-24: Bland and Altman plot displaying the difference between the true flow values and the experimental MRI data using a low-resolution protocol ($n = 32$). This plot corresponds to the contour drawn in the phase image (ROI 2) at 160 mm FOV.

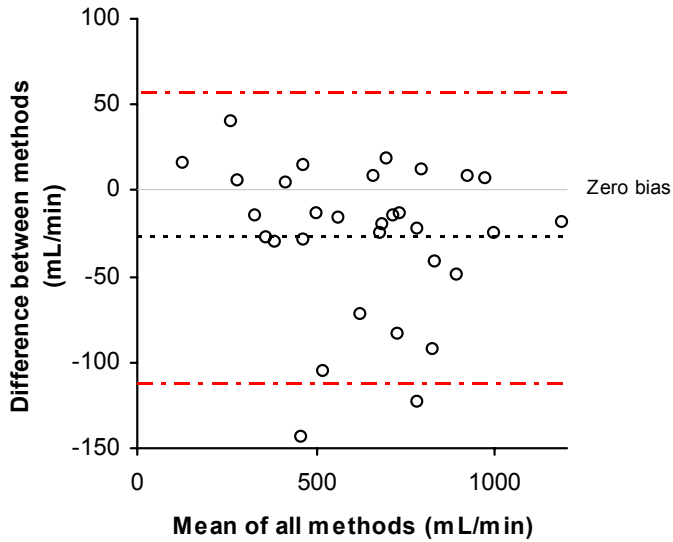


Figure A-25: Bland and Altman plot displaying the difference between the true flow values and the experimental MRI data using a low-resolution protocol ($n = 32$). This plot corresponds to the automatic contour drawn in the phase image (ROI 3) using the algorithm in the FLOW software at 160 mm FOV.

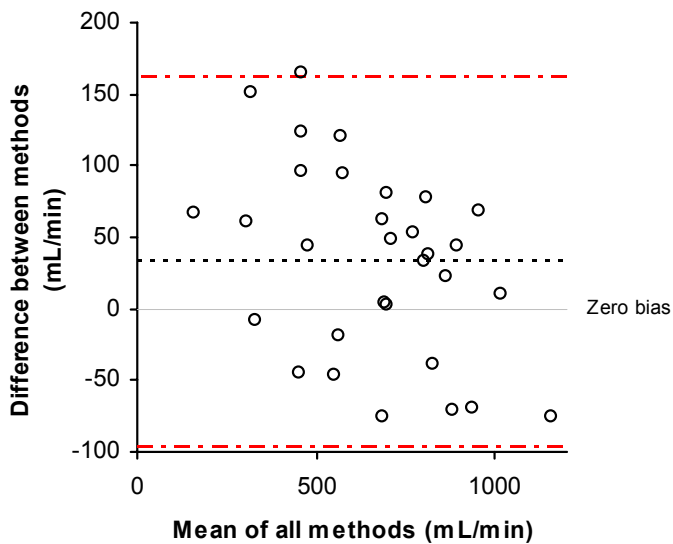


Figure A-26: Bland and Altman plot displaying the difference between the true flow values and the experimental MRI data using a low-resolution protocol ($n = 32$). This plot corresponds to the contour drawn in the magnitude image (ROI 1) at 200 mm FOV.

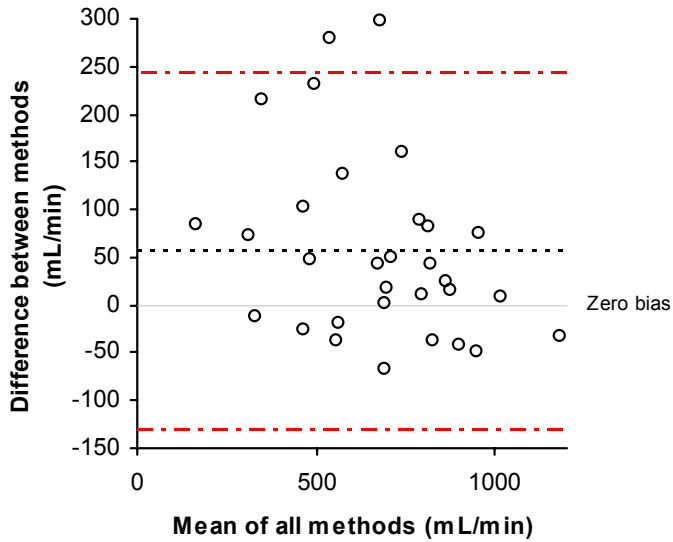


Figure A-27: Bland and Altman plot displaying the difference between the true flow values and the experimental MRI data using a low-resolution protocol ($n = 32$). This plot corresponds to the contour drawn in the phase image (ROI 2) at 200 mm FOV.

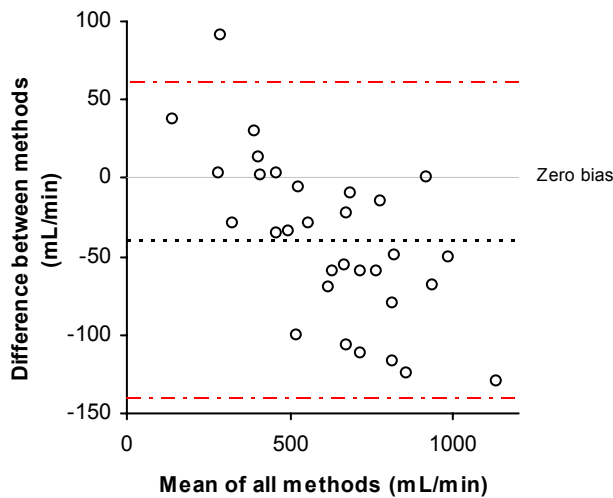


Figure A-28: Bland and Altman plot displaying the difference between the true flow values and the experimental MRI data using a low-resolution protocol ($n = 32$). This plot corresponds to the automatic contour drawn in the phase image (ROI 3) using the algorithm in the FLOW software at 200 mm FOV.

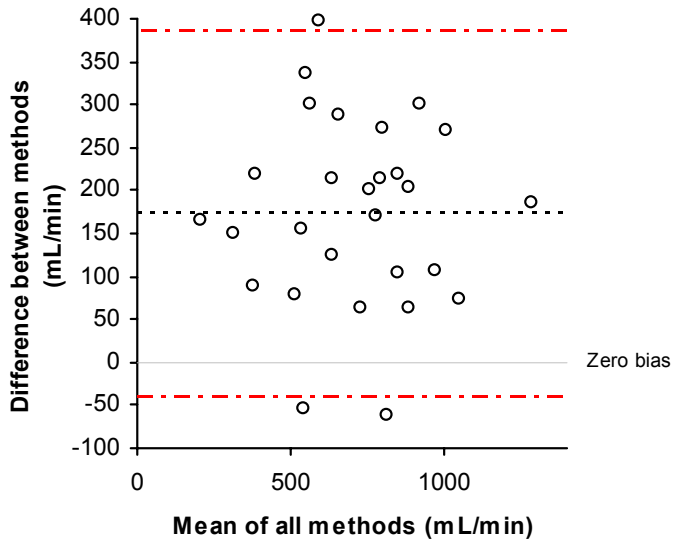


Figure A-29: Bland and Altman plot displaying the difference between the true flow values and the experimental MRI data using a low-resolution protocol ($n = 32$). This plot corresponds to the contour drawn in the magnitude image (ROI 1) at 350 mm FOV.

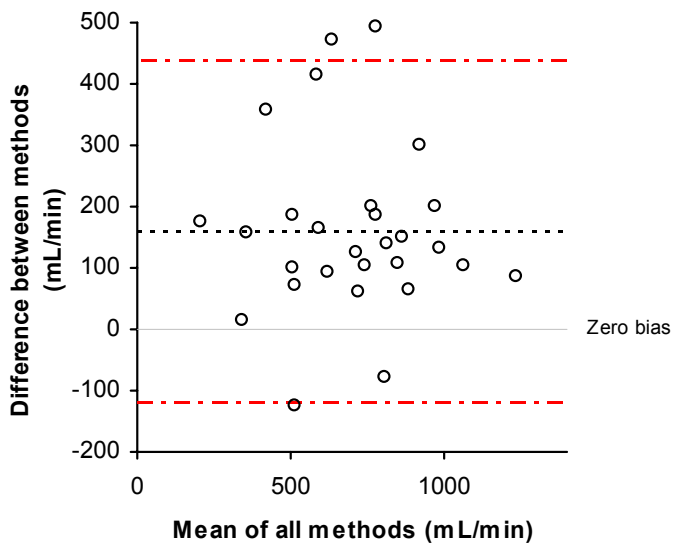


Figure A-30: Bland and Altman plot displaying the difference between the true flow values and the experimental MRI data using a low-resolution protocol ($n = 32$). This plot corresponds to the contour drawn in the phase image (ROI 2) at 350 mm FOV.

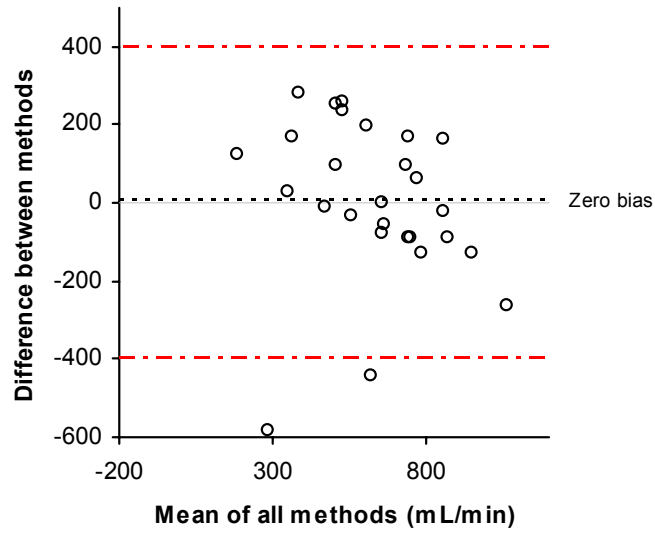


Figure A-31: Bland and Altman plot displaying the difference between the true flow values and the experimental MRI data using a low-resolution protocol ($n = 31$). This plot corresponds to the automatic contour drawn in the phase image (ROI 3) using the algorithm in the FLOW software at 350 mm FOV.

REFERENCES

1. National Institute of Diabetes and Digestive and Kidney (NIDDK) of the National Institutes of Health (NIH). (2003). "Polycystic Kidney Disease." www.niddk.nih.gov/health/kidney/pubs/polycyst/polycyst.htm. July 7, 2003.
2. Torres, V. E. (1998). "New insights into polycystic kidney disease and its treatment." *Curr Opin Nephrol Hypertens*, 7(2): 159-169.
3. US Renal Data System. (2003). *USRDS 2003 Annual Data Report*. Bethesda, MD; National Institutes of Health, National Institute of Diabetes and Digestive and Kidney Diseases: April 2003.
4. Parfrey, P. S., Bear, J. C., Morgan, J., Cramer, B. C., McManamon, P. J., Gault, M. H., Churchill, D. N., Singh, M., Hewitt, R., Somlo, S., Reenders, S. T. (1990). "The diagnosis and prognosis of autosomal dominant polycystic kidney disease." *N Engl J Med*, 323(16): 1085-1090.
5. King, B. F., Reed, J. E., Bergstralh, E. J., Sheedy, P. F. II, Torres, V. E. (2001). "Quantification and longitudinal trends of kidney, renal cyst, and renal parenchyma volumes in autosomal dominant polycystic kidney disease" *J Am Soc Nephrol*, 11(8): 1505-1511.
6. Ritter, S., Baehr, G. (1929). "The arterial supply of the congenital polycystic kidney and its relation to the clinical picture." *J Urol*. 21: 583-592.
7. Schacht, F. (1930). "Hypertension and vascular studies in congenital polycystic kidney," in *Thesis for Master of Science in Urology*. St. Paul, University of Minnesota.
8. Schacht, F. (1931) "Hypertension in cases of congenital polycystic kidney." *Arch Intern Med*. 47: 500-509.
9. Zeier, M., Fehrenbach, P., Geberth, S., Mohring, K., Waldherr, R., Ritz, E. (1992). "Renal histology in polycystic kidney disease with incipient and advanced renal failure." *Kidney Int*, 42(5): 1259-1265.
10. Meier, D., Maier, S., Boesiger, P. (1988). "Quantitative flow measurements on phantoms and on blood vessels with MR." *Magn Reson Med*, 8(1): 25-34.
11. Maier, S. E., Meier, D., Boesiger, P., Moser, U. T., Vieli, A. (1989). "Human abdominal aorta: comparative measurements of blood flow with MR imaging and multigated Doppler US." *Radiology*, 171(2): 487-492.

12. Kondo, C., Caputo, G. R., Semelka, R., Foster, E., Shimakawa, A., Higgins, C. B. (1991). "Right and left ventricular stroke volume measurements with velocity-encoded cine MR imaging: in vitro and in vivo validation." *AJR Am J Roentgenol*, 157(1): 9-16.
13. Sieverding, L., Jung, W. I., Klose, U., Aplitz, J. (1992). "Noninvasive blood flow measurement and quantification of shunt volume by cine magnetic resonance in congenital heart disease. Preliminary results." *Pediatr Radiol*, 22(1): 48-54.
14. Evans, A. J., Iwai, F., Grist, T. A., Sostman, H. D., Hedlund, L. W., Spritzer, C. E., Negro-Vilar, R., Beam, C. A., Pelc, N. J. (1993). "Magnetic resonance imaging of blood flow with a phase subtraction technique. In vitro and in vivo validation." *Invest Radiol*, 28(2): 109-115.
15. Frayne, R., Steinman, D. A., Ethier, C. R., Rutt, B. K. (1995). "Accuracy of MR phase contrast velocity measurements for unsteady flow." *J Magn Reson Imaging*, 5(4): 428-431.
16. Mohiaddin, R. H., Pennell, D. J. (1998). "MR blood flow measurement. Clinical application in the heart and circulation." *Cardiol Clin*, 16(2): 161-187.
17. Powell, A. J., Maier, S. E., Chung, T., Geva, T. (2000). "Phase-velocity cine magnetic resonance imaging measurement of pulsatile blood flow in children and young adults: in vitro and in vivo validation." *Pediatr Cardiol*, 21(2): 104-110.
18. Greil, G., Geva, T., Maier, S. E., Powell, A. J. (2002). "Effect of acquisition parameters on the accuracy of velocity encoded cine magnetic resonance imaging blood flow measurements." *J Magn Reson Imaging*, 15(1): 47-54.
19. King, B.F., Torres, V. E., Brummer, M. E., Chapman, A. B., Bae, K. T., Glockner, J. F., Felmlee, J. P., Grantham, J. J., Guay-Woodford, L. M., Bennett, W. M., Klahr, S., Hirschman, G. H., Kimmel, P. L., Thompson, P. A., Miller, J. P., and the Consortium for Radiologic Imaging Studies of Polycystic Kidney Disease (CRISP). (2003). *Kidney Int*, 64(6): 2214-2221.
20. Ku, D. N., Liepsch, D. (1986). "The effects of non-Newtonian viscoelasticity and wall elasticity on flow at 90° bifurcation." *Biorheology*, 23(4): 359-370.
21. Evans, A. J., Iwai, F., Grist, T. A., Sostman, H. D., L. W., Hedlund, L. W., Spritzer, C. E., Negro-Vilar, R., Beam, C. A., Pelc, N. J. (1993). "Magnetic resonance imaging of blood flow with a phase subtraction technique: in vitro and in vivo validation." *Invest Radiol*, 28(2): 109-115.
22. Frayne, R., Gowman, L. M., Rickey, D. W., Holdsworth, D. W., Picot, P. A., Drangova, M., Chu, K., Caldwell, C. B., Fenster, A., Rutt, B. K. (1993). "A

- geometrically accurate vascular phantom for in-vitro x-ray, ultrasound, and MR flow studies: construction and geometric verification.” *Med Phys*, 20(2 Pt 1): 415-425.
23. Goldstein, D. C., Kundel, H. L., Dube-Witherspoon, M. E., Thibault, L. E., Goldstein, E. J. (1987). “A silicone gel phantom suitable for multi-modality imaging.” *Invest Radiol*, 22(2): 153-157.
 24. Urchuk, S. N., Plewes, D. B. (1995). “A velocity correlation method for measuring vascular compliance using MR imaging.” *J Magn Reson Imaging*, 5(6): 628-634.
 25. Chu, K. C., Rutt, B. K. (1997). “Polyvinyl alcohol cryogel: An ideal phantom material for MR studies of arterial flow and elasticity.” *Magn Reson Med*, 37(2): 314-319.
 26. Mano, I., Goshima, H., Nambu, M., Iio, M. (1986). “New polyvinyl alcohol gel material for MRI phantoms.” *Magn Reson Med*, 3(6): 921-926.
 27. Nambu, M. Goshima, H., Mano, I., (1986). Material for diagnostic NMR imaging (in German), Ger. Offen. DE 3,614,142, 06 November 1986.
 28. Nambu, M., Yamada, N. (1991). Method for determining resolution power or discrimination capacity of an NMR imaging apparatus, U.S. Patent 5,023,185, June 11, 1991.
 29. The PKD Foundation. (2003). “An introduction to the kidneys and PKD.” www.pkdcure.org. July 1, 2003.
 30. Lerman, L.O., Flickinger, A. L., Sheedy, P. F. II, Turner, S. T. (1996). “Reproducibility of human kidney perfusion and volume determinations with electron beam computed tomography.” *Invest Radiol*, 31(4): 204-210.
 31. Moëll, H. (1956). “Size of normal kidneys.” *Acta Radiol*, 46(5):640-645.
 32. Columbia University. (2003). “Kidney disease: Normal kidney function.” *Columbia University Department of Surgery*. www.columbiasuregery.org/programs/tx_renal/dis_function.html.
 33. Novartis. (2003) “Kidneys in situ: Anterior view.” *Columbia University Department of Surgery*. www.columbiasuregery.org/programs/tx_renal/dis_function.html.
 34. Pearson Custom Publishing. (2003). “Human Kidney, Diagram, with Nephron, enlarged.” *Lab Art Library*. 96L.12001. www.labartlibrary.com/symbiosis/96/96L12001.pdf. July 7, 2003.

35. Woo, D. (1995). "Apoptosis and loss of renal tissue in polycystic kidney diseases." *New Eng J Med*, 333(1): 18-25.
36. Dalgaard, O. Z. (1957). "Bilateral polycystic disease of the kidneys: A follow-up of two hundred and eighty-four patients and their families." *Acta Med Scand Suppl*, 158(Suppl 328): 1-255.
37. Iglesias, C. G., Torres, V. E., Offord, K. P., Holley, K. E., Beard, C. M., Kurland, L. T. (1983). "Epidemiology of adult polycystic kidney disease, Olmsted County Minnesota: 1935-1980." *Am J Kidney Dis*, 2(6): 630-639.
38. Delaney, V. B., Adler, S., Bruns, F. J., Licinia, M., Segel, D. P., Fraley, D. S. (1985). "Autosomal dominant polycystic kidney disease: presentation, complications, and prognosis." 5(2): 104-111.
39. Gonzalo, A., Rivera, M., Quereda, C., Ortuño, J. (1990). "Clinical features and prognosis of adult polycystic kidney disease." *Am J Nephrol*, 10(6): 470-474.
40. Churchill, D. N., Bear, J. C., Morgan, J., Payne, R. H., McManamon, P. J., Gault, M. H. (1984). "Prognosis of adult onset polycystic kidney disease re-evaluated." *Kidney Int*, 26(2): 190-193.
41. Milutinovic, J., Fialkow P. J., Agodoa, L. Y., Phillips, L. A., Rudd, T. J., Bryant, J. I. (1984). "Autosomal dominant kidney disease: symptoms and clinical findings." *Q J Med*, 53(212): 511-522.
42. New Horizons Press. (2003). "The Basics of PKD." *Polycystic Kidney Disease Access Center*. www.nhpress.com/pkd/basics.html. July 7, 2003.
43. Rivera, J. F., Martinez-Maldonado, M., Ramirez de Arellano, G. A., et al., (1965). *Bol Assoc Med PR*, 57: 251-262.
44. Newcombe, D. S. (1973). "Gouty arthritis and polycystic kidney disease." *Ann Intern Med*, 79(4): 605.
45. Chapman, J. R., Hilson, A. J. W. (1980). "Polycystic kidneys and abdominal aortic aneurysms." *Lancet*, 1(8169): 646-647.
46. Scheff, R. T., Zuckerman, G., Harter, H., Delmez, J., Koehler, R. (1980). "Diverticular disease in patients with chronic renal failure due to polycystic kidney disease." *Ann Intern Med*, 92(2 pt 1): 202-204.
47. Zeier, M., Geberth, S., Ritz, E., Jaeger, T., Waldherr, R. (1988). "Adult dominant polycystic kidney disease – clinical problems." *Nephron*, 49(3): 177-183.
48. Lejars, F. (1888). "Du fros rein polykystique l'adulte." Paris: *Steinheil*, 1888: 5-55.

49. Bricker, N. S., Patton, J. F. (1957). "Renal function studies in polycystic disease of the kidneys – With observations on the effects of surgical decompression." *N Engl J Med*, 256(5): 212-214.
50. Waters, W. B., Hershman, H., Klein, L. A. (1979). "Management of infected polycystic kidneys." *J Urol*, 122(3): 383-385.
51. Morris, N. (1952). "Pregnancy complicated by congenital polycystic disease of the kidney." *J Obst Gynecol Br Emp*, 59: 822-828.
52. Miller, W. G. (1953). "Pregnancy and polycystic disease of the kidneys." *J Obst Gynecol Br Emp*, 60: 868-871.
53. Sukhatme, V. P. (1997). "Gene therapy for kidney disease." *Adv Nephrol*, 26: 73-80.
54. Van der Geest, R. J., Niezen, R. A., van der Wall, E. E., de Roos, A., Reiber, J. H. (1998). "Automated measurement of volume flow in the ascending aorta using MR velocity maps: evaluation of inter- and intraobserver variability in healthy volunteers." *J Comput Assist Tomogra*, 22(6): 904-911.
55. Powell, A. J., Maier, S. E., Chung, T., Geva, T. (2000). "Phase-velocity cine magnetic resonance imaging measurements of pulsatile blood flow in children and young adults: in vitro and in vivo validation." *Pediatr Cardiol*, 21(2): 104-110.
56. Geva, T., Sahn, D. J., Powell, A. J. (2003). "Magnetic resonance imaging of congenital heart disease in adults." *Prog Pediatr Cardiol*, 17:21-39.
57. Sommer, G., Noorbehesht, B., Pelc, N. (1992). "Normal renal blood flow measurement using phase-contrast cine magnetic resonance imaging." *Invest Radiol*, 27(6): 465-470.
58. Wolf, R. L., King, B. F., Torres, V. E., Wilson, D. M., Ehman, R. L. (1992). "Cine-phase contrast flow volumetry of the renal arteries" (abstr). *Radiology*, 185(P): 163.
59. Lundin, B., Cooper, T. G., Meyer, R. A., Potchen, E. J. (1993). "Measurement of total and unilateral renal blood flow by oblique-angle velocity-encoded 2D-cine magnetic resonance angiography." *Magn Reson Imaging*, 11(1): 51-59.
60. Schoenberg, S.O., Just, A., Bock, M., Knopp, M. V., Persson, P. B., Kirchheim, H. R. (1997). "Noninvasive analysis of renal artery blood flow dynamics with MR cine phase-contrast flow measurements." *Am J Physiol*, (5 Pt 2): H2477-H2484.

61. De Haan, M. W., Kouwenhoven, M., Kessels, A. G., van Engelshoven, J. M. (2000). "Renal artery blood flow: quantification with breath-hold or respiratory triggered phase-contrast MR imaging." *Eur Radiol*, 10(7): 1133-1137.
62. De Haan, M. W., van Engelshoven, J. M. A., Houben, A. J. H. M., Kaandorp, D. W., Kessels, A. G. H., Kroon, A. A., de Leeuw, P. W. (2003). "Phase-contrast magnetic resonance flow quantification in renal arteries." *Hypertension*, 41(1): 114-118.
63. Nayler, G. L., Firmin, D. N., and Longmore, D. B. (1986). "Blood flow imaging by cine magnetic resonance." *J Comput Assist Tomog*, 10(5): 715-722.
64. Firmin, D. N., Nayler, G. L., Klipstein, R. H., Underwood, S. R., Rees, R. S. O., Longmore, D. B. (1987). "In vivo validation of MR velocity imaging." *J Comput Assist Tomogra*, 11(5): 751-756.
65. Mostbeck, G. H., Caputo, G. R., Higgins, C. B. (1992). "MR measurement of blood flow in the cardiovascular system." *AJR*, 159(3): 453-461.
66. Rebergen, S. A., Ottenkamp, J., Doornbos, J., van der Wall, E. E., Chin, J. G., de Roos, A. (1993). "Postoperative pulmonary flow dynamics after Fontan surgery: assessment with nuclear magnetic resonance velocity mapping." *J Am Coll Cardiol*, 21(1): 123-131.
67. Szolar, D. H., Sakuma, H., Higgins, C. B. (1996). "Cardiovascular applications of magnetic resonance flow and velocity measurements." *J Magn Reson Imaging*, 6(1): 78-89.
68. Lee, V. S., Spritzer, C. E., Carroll, B. A., Pool, L. G., Bernstein, M. A., Heinle, S. K., MacFall, J. R. (1997). "Flow quantification using fast cine phase-contrast MR imaging, conventional cine phase-contrast MR imaging, and Doppler sonography: in vitro and in vivo validation." *AJR*, 169(4): 1125-1131.
69. Powell, A.J. and Geva, T. (2000). "Blood flow measurement by magnetic resonance imaging in congenital heart disease." *Pediatr Cardiol*, 21(1): 47-58.
70. Be'eri, E., Maier, S. E., Chung, T., Geva, T. (1998). "In vivo evaluation of Fontan pathway flow dynamics by multidimensional phase-velocity magnetic resonance imaging." *Circulation*, 98(25): 2873-2882.
71. Watanabe, H., Saitoh, M., Igari, D., Tanahashi, Y., Harada, K. (1976). "Non-invasive detection of ultrasonic Doppler signals from renal vessels." *Tohoku J Exp Med*, 118(4): 393-394.
72. Van Herk, G., de Zeeuw, D. (1978). "Unilateral kidney blood flow measurement using the $^{81}\text{Rb}/^{81\text{m}}\text{Kr}$ ratio." *Contrib Nephrol*, 11: 67-72.

73. Debatin, J. F., Ting, R. H., Wegmuller, H., Sommer, F. G., Fredrickson, J. O., Brosnan, T. J., Bowman, B. S., Myers, B. D., Herfkens, R. J., Pelc, N. J. (1994). "Renal artery blood flow: quantitation with phase-contrast MR imaging with and without breath holding." *Radiology*, 190(2): 371-378.
74. Hahn, U., Miller, S., Nägele, T., Schick, F., Erdtmann, B., Duda, S., Claussen, C. D. (1999). "Renal MR angiography at 1.0 T: three-dimensional (3D) phase-contrast techniques versus gadolinium-enhanced 3D fast low-angle shot breath-hold imaging." *AJR*, 172(6): 1501-1508.
75. De Haan, M. W., Kouwenhoven, M., Thelissen, R. P., Koster, D., Kessels, A. G., de Leeuw, P. W., van Engelshoven, J. M. (1996). "Renovascular disease in patients with hypertension: detection with systolic and diastolic gating in three-dimensional phase-contrast MR angiography." *Radiology*, 198(2): 449-456.
76. Nambu, M. (1982). A hydrogel, Japanese Patent Kodai, No. 57/130543.
77. Nambu, M., Makino, N. (1987). Skin markers for NMR and x-ray imaging, European Patent Application EP 228,692, 15 July 1987.
78. Nambu, M., Goshima, H., Mano, I. (1988). Material for diagnosis by nuclear magnetic imaging, U.S. Patent 4,774,957, October 4, 1988.
79. Nambu, M., Makino, N. (1990). Process for making skin marker. U.S. Patent 4,916,170, April 10, 1990.
80. Nambu, M., Watari, T., Sakamoto, T., Akojima, K. (1990). Method for applying electromagnetic wave and ultrasonic wave therapies, U.S. Patent 4,958,626, September 25, 1990.
81. Honda, Y., Naoi, N., Kim, S. Y., Sakaue, E., Nambu, M. (1986). "New disposable ERG electrode made of anomalous polyvinyl alcohol gel." *Doc Ophthalmol*, 63(2):205-207.
82. Nambu, M., Honda, N., Naoi, N., Kim, S. Y., Sakaue, E. (1986). Electrode containing polyvinyl alcohol hydrogel membrane for use in electroretinography, European Patent Application EP 194,598, 17 September 1986.
83. Nambu, M., Honda, Y., Naoi, N., Kim, S. Y., Sakaue, E. (1988). Electrode for use in retinography, U.S. Patent 4,735,207, April 5, 1988.
84. Nambu, M. (1983). Porous hydrogel wound covering, European Patent Application, EP 95,892, 07 December 1983.
85. Wood, L. L., Calton, G. J. (1993). Cryogel bandage containing therapeutic agent, U.S. Patent 5,260,066, November 9, 1993.

86. Nambu, M. (1983). Gel for use as a cooling medium, European Patent Application, EP 70,986, 09 February 1983.
87. Nambu, M. Kinoshita, T., (1984). Hydrogel and its use as a cooling medium, European Patent Application, EP 101,068, 22 February 1984.
88. Tanabe, T. and Nambu, M. (1988). Medical material of polyvinyl alcohol and process of making, U.S. Patent No. 4,734,097, March 29, 1988.
89. Nambu, M., Kuwabara, Y., Okuno, Y., Ohban, T. (1989). Denture Base, U.S. Patent 4,828,493, May 9, 1989.
90. Kraft, K. A., Fatouros, P. P., Clarke, G.D., Kishore, P. R. (1987). "An MRI phantom material for quantitative relaxometry." *Magn Reson Med.* 5(6): 555-562.
91. Blechinger, J. C., Madsen, E. L., Frank, G. R. (1988). "Tissue-mimicking gelatin-agar gels for use in magnetic resonance imaging phantoms." *Med Phys.* 15(4):629-636.
92. Watler, P. K., Cholakis, C. H., Sefton, M.V. (1988). "Water content and compression modulus of some heparin-PVA hydrogels." *Biomaterials*, 9(2): 150-154.
93. Frakes, D. H., Conrad, C. P., Healy, T. M., Monaco, J. W., Fogel, M., Sharma, S., Smith, M. J., Yoganathan, A. P. (2003). "Application of an adaptive control grid interpolation technique to morphological vascular reconstruction." *IEEE Trans Biomed Eng.* 50(2): 197-206.
94. Smith, R. C., Lange, R. C. *Understanding Magnetic Resonance Imaging.* CRC Press, Boca Raton, Florida: 1998.
95. Carr, H. Y., and Purcell, E. M. (1954). "Effects of diffusion on free precession in nuclear magnetic resonance experiments." *Phys Rev*, 94: 630-638.
96. Geva, T., Greil, G. F., Marshall, A. C., Landzberg, M., Powell, A. J. (2002). "Gadolinium-enhanced 3-dimensional magnetic resonance angiography of pulmonary blood supply in patients with complex pulmonary stenosis or arteria: comparison with X-ray angiography." *Circulation*, 106(4): 473-478.
97. Bland, J. M., Altman, D. G. (1986). "Statistical methods for assessing agreement between two methods of clinical measurement." *Lancet.* 1(8476): 307-310.
98. Ward, S. P., Taylor, M. G., Gosling, R. G. (1993). "An alternative approach to the semi-quantitative assessment of the transplanted renal artery velocity sonogram." *BJR*, 66(787): 571-576.

99. Munson, B. R., Young, D. F., Okiishi, T. H. *Fundamentals of Fluid Mechanics*. 4th ed., John Wiley and Sons, Inc., New York: 2002.
100. Pelc, N. J., Herfkens, R. J., Shimakawa, A., Enzmann, D. R. (1991). "Phase contrast cine magnetic resonance imaging." *Magn Reson Q*, 7(4): 229-254.
101. Burkart, D. J., Felmlee, J. P., Johnson, C. D., Wolf, R. L., Weaver, A.L., Ehman, R. L. (1994). "Cine phase-contrast MR flow measurements: improved precision using an automated method of vessel detection." *J Comput Assist Tomogr*, 18(3): 469-475.